2017

Adhesion And Wear Of Nanoscale Polymer Contacts

Yijie Jiang
University of Pennsylvania, toyijie@gmail.com

Adhesion And Wear Of Nanoscale Polymer Contacts

Abstract
Atomic force microscopy (AFM) is a powerful tool for high resolution surface measurements, nanolithography, and tip-based nanomanufacturing. An understanding of the nanoscale tribological behavior of the tip-sample contact, including adhesion and wear, is critical in these applications. In this dissertation, the adhesion and wear of polymethyl methacrylate (PMMA) in contact with an ultrananocrystalline diamond (UNCD) AFM tip is investigated using a combination of AFM-based nanomechanics experiments and finite element analysis (FEA).

A novel AFM-based method, which combines pull-off force measurements and characterization of the 3D geometry of AFM tip, was developed to quantify the properties of the adhesive traction-separation relationship of UNCD-PMMA contacts. Adhesion range and strength, as well as work of adhesion, of the contacts were determined. Characterizing and understanding nanoscale wear of polymers has proven difficult in the past due to experimental complications associated with debris produced in the tests and the failure of traditional empirical wear relations, such as Archard's law. Here, nanoscale AFM-based line and raster wear experiments were performed on patterned PMMA structures, which had gaps that allow debris to be captured. Results from the line wear tests indicate that the relationship between height loss rate and stress is well described by a transition state theory wear model. The wear parameters obtained from line wear tests were applied to predict the volume loss in raster wear tests. Despite the significant differences in the loading and sliding geometry between line and raster wear experiments, the raster wear behavior was accurately predicted from the parameters obtained from line wear tests. In addition, experiments at varying temperatures were performed to study the temperature dependence of polymer wear. The results suggest that transition state theory overestimates the effect of temperature on wear for PMMA. Modified models considering viscoelastic relaxation of PMMA and atom-by-atom attrition were applied to describe the measured wear behavior. Finally, an iterative FEA method was developed for simulations of wear. These simulations were used to examine the evolution of geometry and stress during the wear process as a function of contact conditions, such as friction and surface roughness.

Degree Type
Dissertation

Degree Name
Doctor of Philosophy (PhD)

Graduate Group
Mechanical Engineering & Applied Mechanics

First Advisor
Kevin T. Turner

Keywords
Adhesion measurements, AFM-based nanomechanics, Finite element analysis, Nanoscale wear, Polymer contacts, Transition state theory

ADHESION AND WEAR OF NANOSCALE POLYMER CONTACTS

Yijie Jiang

A DISSERTATION

in

Mechanical Engineering and Applied Mechanics

Presented to the Faculties of the University of Pennsylvania

in

Partial Fulfillment of the Requirements for the

Degree of Doctor of Philosophy

2017

Supervisor of Dissertation

_____

Kevin T. Turner, Professor, Mechanical Engineering and Applied Mechanics

Graduate Group Chairperson

_____

Kevin T. Turner, Professor, Mechanical Engineering and Applied Mechanics

Dissertation Committee

Robert W. Carpick
John Henry Towne Professor, Mechanical Engineering and Applied Mechanics

David J. Srolovitz
Joseph Bordogna Professor, Materials Science and Engineering

ACKNOWLEDGMENTS

I would like to sincerely express my gratitude to my advisor Prof. Kevin Turner for his guidance and support with my research. Prof. Turner is always encouraging, patient and inspiring throughout the progression to complete this work.

I gratefully acknowledge Prof. Robert Carpick and Prof. Judith Harrison for suggestions and support in the nanoscale wear project. I thank Prof. Tevis Jacobs, Prof. David Schall, Dr. Vahid Vahdat, Dr. Rodrigo Bernal and Zachary Milne for collaboration and discussion. I would also like to acknowledge Dr. Matthew Brukman for his training and great assistance in atomic force microscopy.

I enjoy working with Prof. Daeyeon Lee and Jyo Lyn Hor in nanocomposite project, and Prof. John Hart and Dr. Sanha Kim in carbon nanotube project. I am thankful for their advice and collaboration. These experiences have broadened my knowledge and will benefit me in the future.

I wish to thank my friends and colleagues Helen Minsky, Nathan Ip, Dr. Michael Wald, Lisa Mariani, and the other past and present members of the Turner Research Group for their helpful discussions, useful suggestions and friendship over the past five years.

I would like to gratefully thank my family for their support during this endeavor and throughout my life. Xin, my lovely wife, is always a source of encouragement, company and love. My parents, Shidong and Fuqin, receive my deepest gratitude and love for their dedication and education.

ABSTRACT

ADHESION AND WEAR OF NANOSCALE POLYMER CONTACTS

Yijie Jiang

Kevin T. Turner

Atomic force microscopy (AFM) is a powerful tool for high resolution surface measurements, nanolithography, and tip-based nanomanufacturing. An understanding of the nanoscale tribological behavior of the tip-sample contact, including adhesion and wear, is critical in these applications. In this dissertation, the adhesion and wear of polymethyl methacrylate (PMMA) in contact with an ultrananocrystalline diamond (UNCD) AFM tip is investigated using a combination of AFM-based nanomechanics experiments and finite element analysis (FEA).

A novel AFM-based method, which combines pull-off force measurements and characterization of the 3D geometry of AFM tip, was developed to quantify the properties of the adhesive traction-separation relationship of UNCD-PMMA contacts. Adhesion range and strength, as well as work of adhesion, of the contacts were determined. Characterizing and understanding nanoscale wear of polymers has proven difficult in the past due to experimental complications associated with debris produced in the tests and the failure of traditional empirical wear relations, such as Archard's law. Here, nanoscale AFM-based line and raster wear experiments were performed on patterned PMMA structures, which had gaps that allow debris to be captured. Results from the line wear tests

indicate that the relationship between height loss rate and stress is well described by a transition state theory wear model. The wear parameters obtained from line wear tests were applied to predict the volume loss in raster wear tests. Despite the significant differences in the loading and sliding geometry between line and raster wear experiments, the raster wear behavior was accurately predicted from the parameters obtained from line wear tests. In addition, experiments at varying temperatures were performed to study the temperature dependence of polymer wear. The results suggest that transition state theory overestimates the effect of temperature on wear for PMMA. Modified models considering viscoelastic relaxation of PMMA and atom-by-atom attrition were applied to describe the measured wear behavior. Finally, an iterative FEA method was developed for simulations of wear. These simulations were used to examine the evolution of geometry and stress during the wear process as a function of contact conditions, such as friction and surface roughness.

TABLE OF CONTENTS

LIST OF TABLES

LIST OF ILLUSTRATIONS

CHAPTER 1: Introduction

1.1 Introduction and motivation

Tip-based nanomanufacturing (TBN) uses atomic force microscopy (AFM) probes for the direct production of nanostructures, for nanolithography to create masks on surfaces, and for patterning samples for specific applications. There are a wide range of TBN methods, such as thermal [1]–[3], electrical [4], [5], mechanical [6], [7], dip-pen nanolithography [8], [9] and nanomanipulation [10], [11].

Thermal nanolithography, perhaps one of the most promising TBN methods, uses an AFM cantilever with an integrated resistive heater near the tip. To pattern a pixel, a short voltage pulse produces a current that heats the tip. The heat evaporates a small volume of material from the contacting surface. By controlling the voltage and time, 3D features have been patterned in polymer [1] and molecular glass surfaces [2] (Figure 1-1a-b). Wang *et al.* [12] introduced an AFM tip hammering nanolithography method and used it to emboss and imprint patterns (~20 nm line width and several nm in height) in polystyrene-block-poly(ethylene/butylenes)-block-polystyrene (SEBS) copolymer thin films (Figure 1-1c). The surface was comprised of well-ordered hexagonal PS spheres after being annealed in cyclohexane vapor for ~48h. The structures could be erased by annealing at 70 ^{o}C for 5 min. Martín *et al.* [4] described a technique for producing nanoscale patterns on a thin PMMA layer on a Si wafer. The patterns were made by electrostatic modification

of PMMA and local oxidation of silicon. The lines obtained in a 25 nm thick PMMA layer at speed of 0.5 μm/s and a voltage of 30V (tip positive) were drawn by a doped Si AFM tip.

Compared to above methods, mechanical lithography, in which material is removed through pure mechanical means, has advantages, including the simplicity of the preparation of sample, and no special requirements for AFM tip and setup. Dynamic plowing [6], [13] or static patterning can be achieved by using tapping or contact mode AFM with programmed tip movements. Figure 1-1d shows an example of the University of Pennsylvania logo patterned in a PMMA thin film through mechanical removal of material by a Si AFM tip (radius ~10 nm). A vector image of the pattern was first prepared and then converted via Nanoman function on a Bruker Icon® AFM. The Si tip was slid along the programmed paths (smallest path separation is ~40 nm) under a contact load of 2.5 μN.

Polymers are widely used in microelectromechanical systems (MEMS), nanoelectromechanical systems (NEMS), and TBN applications [1], [2], [4], [12], [14], [15]. Polymers are used in TBN processes as a mask layer for lithography to generate holes, nanogrooves or patterns [4], [14], [16], as a sacrificial layer for lift-off to obtain nanoparticles or nanowires [15], [17], [18] or as a top layer for patterning and modification to form nanostructures [1], [12], [13], [19]–[22].

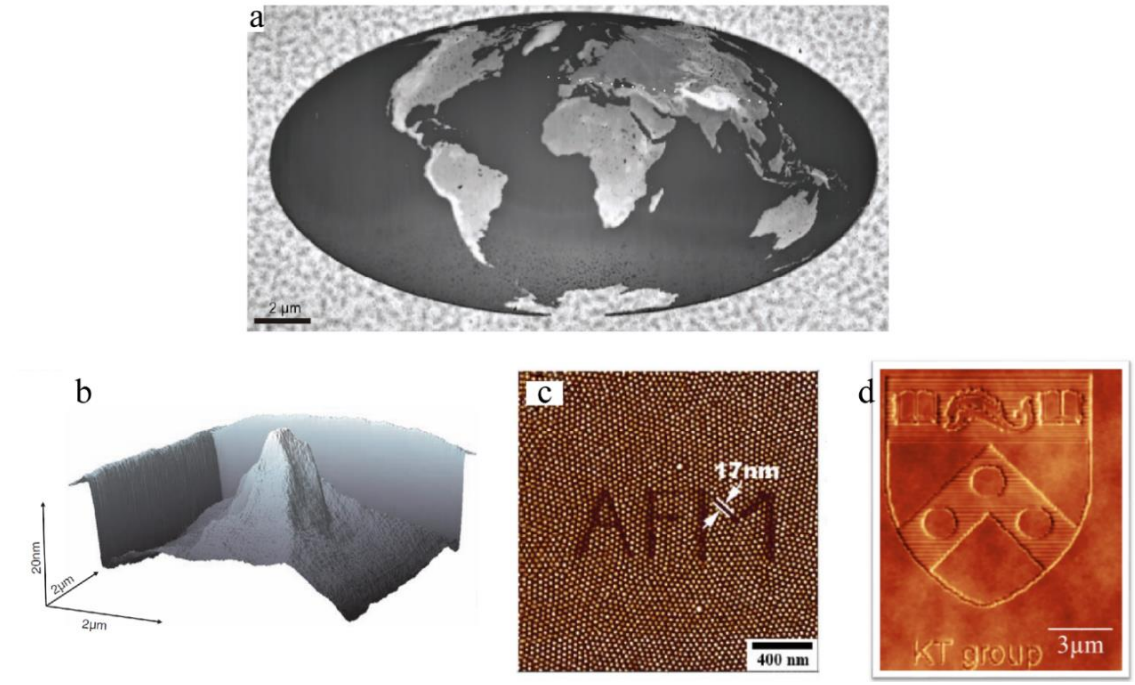

Figure 1-1. Thermal nanolithography results of (a) a 3D topographic map patterned into a polymer [1] and (b) a replica of the Matterhorn patterned in molecular glass sample [2], (c) pattern in a SEBS thin film made by AFM tip hammering nanolithography [12], and (d) a Penn logo in a PMMA thin film made by nanomechanical lithography.

Polymethyl methacrylate (PMMA) is an amorphous thermoplastic with a number of desirable properties, including transparency, chemical resistance, moldability, low ultraviolet radiation sensitivity, high strength, and dimensional stability [23], [24]. PMMA has versatile applications, including nanocomposites [23], [25], medical applications, such as bone cement [26], [27], MEMS and NEMS structures [14] and as a resist in high resolution e-beam lithography [18], [20]. A variety of patterns have been made in PMMA using TBN techniques [4], [13], [17], [18], [20], as listed in Table 1-1. The tribological properties of PMMA, including the adhesion and wear, not only influence the optimization

of the selection of TBN parameters, but also strongly influence the quality of the generated nanostructures and can affect the resolution of the process [6], [14], [22], [28]–[30].

Table 1-1. Summary of TBN techniques applied to PMMA.

Ref.	Method	Patterns
Martín et al. [4]	Electrostatic modification	Long lines of several hundred nm in width in 25 nm thick film; Holes with varying size at varying voltages
Cappella and Sturm [13]	Mechanical lithography (dynamic plowing and nanoindentation)	Dots with varying size and depth (10-100 nm) under varying loads in nanoindentation; 7×7 μm^2 squares with depth of 20 nm using dynamic plowing
Chen, Hsu and Lin [17]	Mechanical lithography (contact mode)	50-70 nm wide lines in 50 nm thick film; Cutting of nanowires with ~40 nm gaps
Sohn and Willett [18]	Mechanical lithography (contact mode)	15 μm long and ~40 nm wide lines in 24 nm thick film
Heyde et al. [20]	Mechanical lithography (dynamic plowing)	~40 nm wide lines of 2-6 nm depth depending on tapping amplitude setpoint

While the nanoscale tribological properties are critical in TBN, there is a poor understanding of adhesion and wear of PMMA at the nanoscale. The adhesion between PMMA and common AFM tip materials, such as Si, Si_3N_4, ultrananocrystalline diamond (UNCD) and metal coated, has not been reported yet. More importantly, a method for characterization of strength and range of adhesion has not been developed when considering the 3D geometry details of the contact pair. In reality, the contact area between an AFM tip and sample are usually non-symmetric and rough [31]–[33]. The nanoscale

roughness has strong influence on the adhesion [32], [34]–[36]. Therefore, such characterization method is required for better understanding the adhesion during TBN processes.

Studies on the wear of PMMA have been done of various scales from millimeter down to micro/nano scale, including the pin-on-disk methods [23], [25], nanoindentation and nanoscratch tests [26], [30], AFM-assisted tests [13], [14], [37] and many other experiments [27], [38], [39]. However, there are two key problems remains to be solved:

a) In all previous studies, Archard's wear law, which assumes wear volume is proportional to the normal external load and the sliding distance, is applied while the reported wear rates of PMMA vary in a wide range (~1×10^{-9} to 1×10^{-4} $mm^3/N\cdot mm$) due to the different polymer structures and experimental conditions, such as loading and sliding speed [14], [23], [25]. Recent nanoscale studies suggest an alternate wear model – transition state theory [28], [40]–[44]. The application of transition state theory to polymer nanoscale wear has not been investigated.

b) The debris and material pile-up is produced by the contact and movement of AFM tip on the polymer surface. This contamination on the surface make it difficult to fabricate desired nanostructures, like grooves with high height-to-width aspect ratios [18], and also cause difficulties in calculating the contact stress and measuring volume or height variation accurately [12]–[14], [45].

1.2 Objectives

The overall objective of this dissertation is to characterize the adhesion and wear properties of PMMA surfaces at the nanoscale via AFM-based experiments. Finite element analysis is applied to validate the methods and analyze the stress and adhesion behavior. This work includes the following sub-objectives:

a) Develop a novel approach for measuring the properties of the adhesion traction separation relationship of nanoscale contacts with AFM.

b) Investigate the nanoscale wear behavior of PMMA by line and raster AFM scanning tests under controlled environment.

c) Investigate the effect of temperature on wear mechanism through temperature controlled AFM experiments.

d) Use the experimentally measured wear behavior in FEA-based wear simulations.

1.3 Scope

Understanding nanoscale adhesion and wear between an AFM tip and a polymer surface is crucial for advancing nanofabrication and nanolithography processes. Traditional adhesion and wear experiments are not suitable for measuring the behavior at nanoscale, for example, the difficulties in measuring the strength and range of adhesion

between the nanoscale interface, and the wide range of wear coefficients of PMMA obtained when using Archard's law. In this work, I present a) a novel method for measuring the traction-separation relationship between an AFM tip and contacting surface, b) systematically controlled PMMA wear experiments and description of the data via modified transition state wear models, and c) development and application of numerical wear simulations. The scope of this dissertation is described below.

First, a review of relevant literature on adhesion and wear mechanisms is presented in Chapter 2. Next, Chapter 3 presents a novel approach for measuring the traction-separation adhesion relationships of nanoscale contacts at the UNCD-PMMA interface. The experimental methods, including the measurements of 3D tip geometry and AFM pull-off force, are introduced first. Combining pull-off force measurements with high resolution 3D geometry measurements of the AFM tips, we extracted the properties of the traction-separation relationship, namely the work of adhesion, adhesive stress and adhesion range. Following the analyses, FEA is used to validate assumptions in the analysis.

Chapter 4 investigates the wear behavior of PMMA at nanoscale at room temperature. Two types of nanoscale wear tests using AFM, line and raster scanning, are presented in this Chapter. Contact stresses are calculated by FEA by importing measured 3D tip geometries into the models. In AFM line wear tests, the wear behavior is well described by a recently proposed wear mechanism, i.e. transition state theory. By using the parameters determined from line wear tests, the volume loss in raster wear tests can be accurately predicted.

The investigation of the temperature dependence of nanoscale polymer wear is described in Chapter 5. AFM-based raster wear tests are performed at varying temperatures. The experimental data indicates an increasing wear volume loss rate with increasing temperature. However, the transition state theory significantly overestimates the volume loss rate at elevated temperatures. Modified wear models, which include the effect of viscoelastic relaxation of PMMA, are developed based on a time-temperature superposition approach. The proposed models reasonably describe the wear behavior over the temperature range examined in the tests.

Chapter 6 presents microscale wear tests done on a commercial nanoindenter. Repeated line wear tests were perform at a scale where load and contact area are two to three orders of magnitude higher than those in nanoscale tests. The wear tracks are characterized by AFM imaging and indicate that the transition state theory is applicable, even at a significantly larger scale compared with previous nanoscale tests, to quantify the wear volume loss.

Finite element wear simulations are summarized in Chapter 7. An iterative algorithm is developed and applied in 2D and 3D wear simulations between a paraboloidal tip and samples, which is similar to the AFM tip-sample interaction. Details of the geometry change and evolution of stress distribution during the wear process, which are extremely difficult to be monitored during experiments, are obtained in the simulations. Wear simulations under systematically controlled contact conditions, such as friction and

interfacial roughness, are performed. The dependence of wear on contact stiffness and roughness are observed from numerical simulations.

CHAPTER 2: Literature review

2.1 Adhesion mechanics

2.1.1 Adhesion models without roughness

Prior to reviewing the theories of adhesive contact, Hertzian contact theory [46] is introduced. Hertz was the first to analyze the deformation of two elastic paraboloids in frictionless, non-adhesive contact as they were pressed against each other (Figure 2-1).

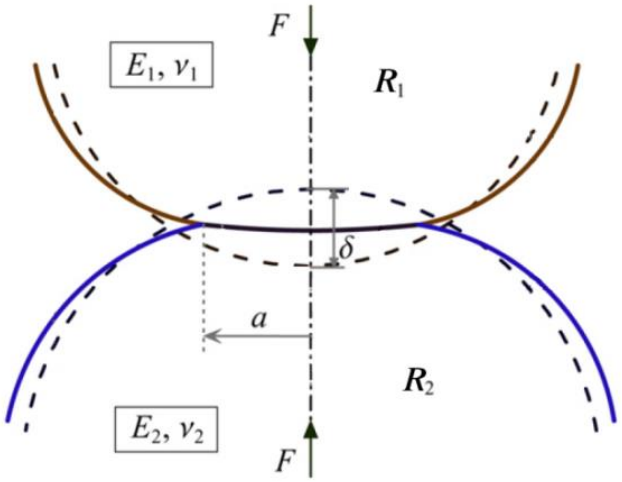

Figure 2-1. Schematic of contact between two paraboloids (image taken from [47]).

The Hertz expressions for contact radius, a, and indentation depth, δ, as a function of applied load, F, geometry and material properties are:

$$a = \left(\frac{3FR}{4E^*}\right)^{1/3} \text{ and } \delta = \left(\frac{9F^2}{16RE^{*2}}\right)^{1/3} \tag{2.1}$$

where E^* is the reduced elastic modulus,

$$E^* = \left(\frac{1-\nu_1^2}{E_1} + \frac{1-\nu_2^2}{E_2} \right)^{-1} \tag{2.2}$$

and R is the effective radius,

$$R = \left(\frac{1}{R_1} + \frac{1}{R_2} \right)^{-1} \tag{2.3}$$

where E_1, E_2, ν_1, ν_2, R_1, and R_2 are elastic moduli, Poisson's ratios and radii of curvature of two paraboloids.

Johnson, Kendall and Roberts [48] established an approach for modeling adhesive contact by minimization of the total energy as a function of the contact radius. This approach is now referred to as the JKR theory. The equilibrium condition is expressed as:

$$\frac{dU_T}{da} = 0 \tag{2.4}$$

where U_T is the total energy and consists of the elastic strain energy, U_E, mechanical energy done by external load, U_M, and surface energy, U_S, i.e. $U_T = U_E + U_M + U_S$. The surface energy term is given as

$$U_s = \pi a^2 W_a \tag{2.5}$$

where W_a is the work of adhesion, which represents the energy per unit area to separate two perfectly flat surfaces from equilibrium contact to infinite separation. The work of adhesion is an important property of an interface that determines adhesion force and

influencing the contact stresses. From JKR theory, the adhesion force, aka "pull-off force", can be derived as

$$F_{adh} = \frac{3}{2}\pi W_a R . \tag{2.6}$$

Derjaguin, Muller and Toporov [49] proposed a different approach for modeling the adhesion of spheres in contact. Specifically, they suggested that the adhesive force acts only outside of the contact area. This approach is referred as the DMT theory and leads to an adhesion force of

$$F_{adh} = 2\pi W_a R . \tag{2.7}$$

In DMT theory, the adhesion force contributes to the total normal force on the contact. The stress distribution within the contact area is described by Hertzian contact theory. Both JKR and DMT models show that the adhesion force depends on work of adhesion, but is independent of strength or range of adhesion in the ideal geometry, i.e. smooth sphere or paraboloid.

While the JKR and DMT theories seemingly conflict with each other by giving different expressions for the adhesion force between two paraboloids, Tabor [50] and Maugis [51] showed that the DMT and JKR theories are compatible and apply in different regimes. Non-dimensional parameters, now known as the Tabor and Maugis parameters, can be used to describe the transition between the JKR and DMT regimes. In Maugis' approach, a Dugdale traction-separation law [51], [52] is used to describe the adhesion.

The DMT-JKR transition is shown in Figure 2-2 by using Maugis-Dugdale theory. The Maugis parameter is defined as:

$$\lambda_{Maugis} = \sigma_D \left(\frac{9R}{2\pi W_a E^{*2}} \right)^{1/3} \tag{2.8}$$

where σ_D is the strength of adhesion. As the Maugis parameter, λ_{Maugis}, increases, the appropriate model for describing the contact transitions from DMT theory to JKR theory.

All of the adhesive contact theories introduced above focus on the contact between paraboloids. An extended Maugis-Dugdale theory is proposed by Zheng and Yu [47] for the frictionless adhesive contact of arbitrary axisymmetric elastic objects. The analysis for adhesive contact between an n^{th} order power-law shaped tip and a flat surface from [47] has been recently applied to AFM experimental data analysis recently [31]. Referred to as the M-D-n model, it can describe the transition between JKR-type and DMT-type behavior for power-law shaped contacts [47].

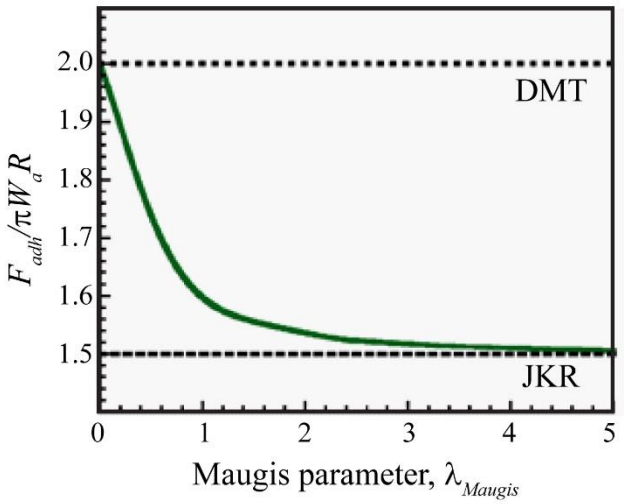

Figure 2-2. Dimensionless pull-off force as a function of Maugis parameter.

2.1.2 Effect of roughness on adhesion

Fuller and Tabor conducted adhesion force measurements between rubber spheres with radii from 7.3 to 53 mm in contact with rough stiff Perspex surfaces [53]. The center line average roughness of the surface in the experiments varied from 0.12 to 1.4 μm, and resulted in a 90% change in the adhesion force. They presented a theoretical analysis to describe their experimental observations. In their analysis, they examined the case of a smooth flat in contact with a (nominally flat) roughened surface based on the following assumptions: (a) surface roughness is made up of a series of asperities with a Gaussian height distribution, (b) the asperities can be described as spherical caps of the same radius and (c) JKR theory can be used to describe the adhesion of individual asperities. An adhesion parameter to describe the effect of roughness was obtained:

$$\theta = \frac{E^*}{W_A}\sqrt{\frac{\sigma^3}{\beta}} \tag{2.9}$$

where β is the radius of the asperities and σ is the standard deviation of the Gaussian distribution of asperity heights.

As shown in Figure 2-3, the experimental results (shown as rectangles) and the theory (shown as curves) indicate that the adhesion monotonically reduces with increasing roughness. The relative pull-off force is the ratio of the pull-off force between rubber and rough surface to that between same rubber and smooth surface.

The dimensionless parameter proposed by Fuller and Tabor has also been applied in a study of the effect of roughness on direct wafer bonding of silicon wafers with high modulus [54]. The study presents five direct bonding experiments on silicon wafers with different roughness with θ varying from 0.1 to 16.8. The theoretical analyses have reasonable agreement with the experimental data and indicate a transition from bonding regime ($\theta < 1$) to non-bonding regime ($\theta > 12$).

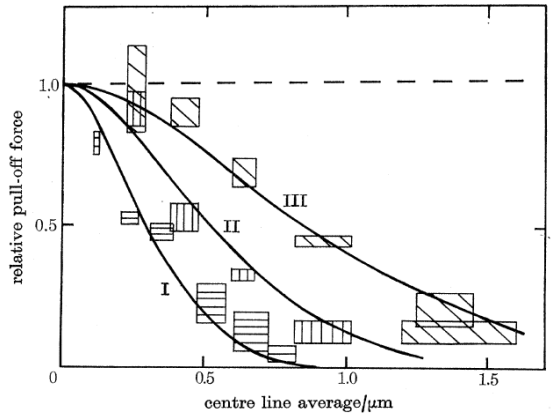

Figure 2-3. Experimental results and theoretical curves of relative pull-off force between smooth rubber spheres and rough Perspex surfaces [53].

In another work examining roughness [34], the interaction between a large blunt smooth particle and hemispherical asperities on a surface is studied. The large radius of the blunt particle makes these results applicable to flat-on-flat contacts. The Katainen model [34] assumes multiple contacts with asperities of same radius underneath a large smooth surface to obtain the adhesion force as

$$F_{adh} = \frac{A_H A}{6z_0^2}\left[\rho r + \frac{1}{\pi z_0 (1 + y_{max}/z_0)^3}\right] \tag{2.10}$$

where A is the nominal contact area, y_{max} is the maximum height of asperities, ρ is the density of the asperities (i.e., number of asperities per area), r is the radius of asperities, A_H is the Hamaker constant and z_0 is the distance of closest approach between surfaces. The first term represents the van der Waals interaction of Lennard-Jones potential between the blunt particle with the asperities and the second with the flat substrate.

Pull-off force measurements between blunt silica AFM tips (varying size up to 5×10^4 nm^2) and ALD coated TiO_2 thin films were performed [34] and compared to this model. The radius of curvature of asperities on the TiO_2 films varied from ~10 to ~30 nm, the maximum height y_{max} from ~1.5 to ~26 nm and the density from 120 to 880 μm^{-2}. The Katainen model provided relatively good agreement with the experimental data when multiple contacts happened between the blunt tips and asperities. Ramakrishna *et al.* [55] subsequently adopted the Katainen model in analyzing data from contact experiments between polyethylene microspheres (diameter between 18 to 20 μm) and silica nanoparticle roughened surfaces. The silica nanoparticles had a diameter ~12 nm and were distributed across the surface with various densities. The contact was treated as a flat on flat contact due to the large size of microsphere. Particle densities varied from 0 to 416 μm^{-2} and the experimental results fit the Katainen model well.

Miki and Spearing [35] argued that the standard deviation or the root mean square (rms) roughness did not provide sufficient information about the surface morphology when considering the adhesion of stiff semiconductor wafers. Bearing ratio, which describes the

area of surface lying above a given depth, was proposed as an alternate metric to describe the role of roughness on the effective bonding energy as well as adhesion force. In their study, silicon surfaces were roughened by using a buffered oxide etch solution (BOE) and/or a potassium hydroxide solution (KOH). The roughened wafers were direct bonded to a second silicon wafers and the resulting bonding energy was measured by using a displacement-loaded double cantilever beam geometry. A linear relationship between the normalized bonding energy and the bearing ratio of the surfaces measured by AFM, as depicted in Figure 2-4, indicates that the bearing ratio can be a good metric to describe the effect of roughness on adhesion.

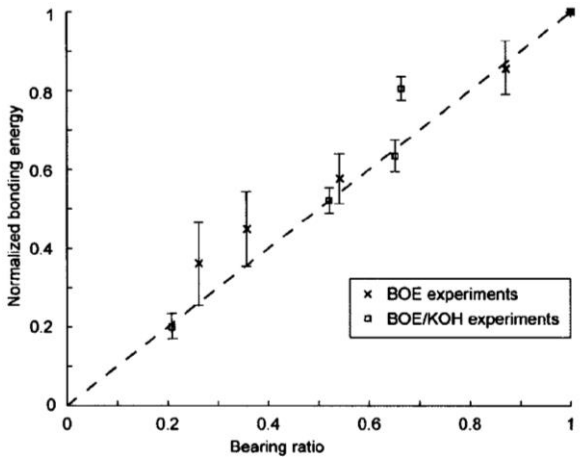

Figure 2-4. Normalized bonding energy as a function of bearing ratio for direct bonded silicon wafers [35].

Peressadko *et al.* [36] conducted pull-off force measurements between rubber and aluminum surfaces. Seven different surfaces with rms roughnesses from ~30 to ~ 200 nm were tested. No direct relation between the strength of the adhesion and the rms roughness was found. Alternatively, they used a model in which the surface roughness is described as

a self-affine fractal [56] to consider the roughness. Specifically, the surface roughness power spectra as shown in eq. (2.11) is used to describe the surface roughness,

$$C(q) = \frac{1}{(2\pi)^2} \int \langle h(x), h(0) \rangle e^{iq \cdot x} d^2 x \tag{2.11}$$

where *C(q)* is the surface roughness power spectra, *h(x)* is the height profile, and *q* is the magnitude of wave vector. $\langle \cdots \rangle$ indicates the ensemble average.

The approximated effective surface energy, which is directly related to adhesion force in a DMT or JKR contact, as:

$$\gamma_{eff} = \frac{A}{A_0} \Delta\gamma - \frac{\pi E}{2(1-\nu^2)} \int_{q_0}^{q_1} q^2 C(q) dq \tag{2.12}$$

where $\Delta\gamma$ is the surface energy obtained from the surface with lowest roughness, A/A_0 is the increase of the surface area due to roughness, *E* and *v* are elastic modulus and Poisson's ratio for the rubber. This equation is referred to as Persson's model.

It is important to note that in Persson's model complete contact between two bodies is assumed [56]. This is applicable if at least one of the bodies is a soft material since elastic deformation can be large enough to fill the gaps between two roughened surfaces. In stiff material cases, e.g. the wafer bonding case of Miki and Spearing [35] discussed earlier, this power spectra model may not be valid.

Rumpf [57] developed one of the most commonly used models of adhesion force in the nanoscale roughness regime. The Rumpf model is based on contact of a single

hemispherical asperity with a much larger spherical particle. The asperity is centered at the surface and interacts with the spherical particle along a line normal to the surface connecting their centers. The adhesion force is given by eq. (2.13).

$$F_{adh} = \frac{A_H}{6z_0^2}\left[\frac{rR}{r+R} + \frac{R}{(1+r/z_0)^2}\right] \tag{2.13}$$

where *r* and *R* are the radii of the asperity and particle. The two parts of eq. (2.13) are Van der Waals forces representing that the particle interacts with the asperity and with the flat substrate, respectively. A primary limitation of this model is the strict requirement of the location of asperity. Several extensions of the Rumpf's model have been developed, such as Katainen model [34], the modified Rumpf model, and Rabinovich's model [58].

A root mean square (rms) value was introduced to describe the roughness of flat surfaces in the modified Rumpf model [58]. The rms roughness is more easily measured than the radius of the asperity. The relation between rms roughness and the asperity radius is developed based on the assumption of a hemispherical shaped asperity. The modified Rumpf model is [58]:

$$F_{adh} = \frac{A_H R}{6z_0^2}\left[\frac{1}{1+R/(1.48rms)} + \frac{1}{(1+1.48rms/z_0)^2}\right] \tag{2.14}$$

where rms is the root mean square value of roughness on the flat surface. The factor 1.48 is valid as long as it is assumed that the surface contains an equal number of asperities and pits [58].

A more realistic model was proposed (referred to as Rabinovich's model) in the same study [58]. A schematic illustration of the model geometry is shown in Figure 2-5.

The asperity is still modeled as a sphere, but the center of the asperity is not required to be positioned at the surface. Furthermore, not only is the height of the asperity used, but its breadth is also considered.

$$F_{adh} = \frac{A_H R}{6z_0^2}\left[\frac{1}{1+(32Rk_1 rms/\lambda^2)} + \frac{1}{(1+k_1 rms/z_0)^2}\right] \tag{2.15}$$

where k_1 is a coefficient linking maximum height of the asperity and the rms roughness, and λ is peak-to-peak distance. The value k_1=1.817 is determined under the assumption that the asperity and pit have the same geometry and equal number.

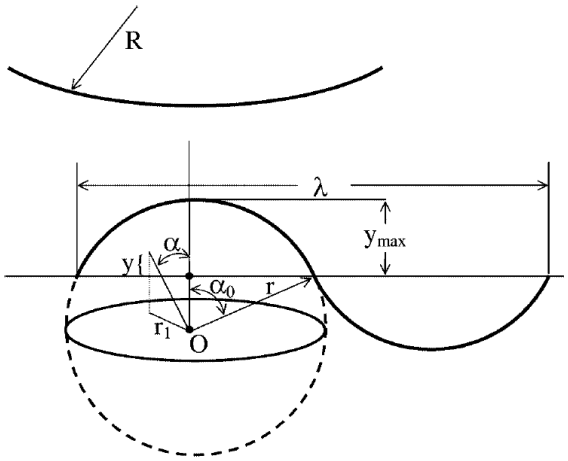

Figure 2-5. Schematic illustration of the geometric model in Rabinovich's model [58].

In all the models above, the sphere is assumed to be smooth and the roughness is only measured and included on the nominal flat surface. Recently, however, the effect of roughness on paraboloidal shaped AFM tips has been considered [32]. Jacobs *et al.* [32] combined both molecular dynamics (MD) simulations and *in-situ* TEM-based nanoindentation experiments to study the effect of roughness of AFM tips. Adhesion of diamond-like carbon (DLC) and ultrananocrystalline diamond (UNCD) AFM tips in

contact with diamond surfaces were examined. The profiles of AFM tips were fit by paraboloids with radii varying from 22 to 116 nm and rms roughness values from 0.18 to 1.58 nm were measured via TEM. Models with 2.3 to 2.7 nm radius and rms roughness 0.03 to 0.12 nm were established in MD simulations. The adhesion force was measured in both numerical simulations and experiments. The relation between adhesion force and work of adhesion was established by DMT theory. Based on the modified Rumpf's model [58], the effective work of adhesion was found to be $W_{a,eff}$:

$$W_{a,eff} = \frac{A_H}{12\pi z_0^2}\left[\frac{1}{1 + R_{tip}/(1.48rms)} + \frac{1}{(1 + 1.48rms/z_0)^2}\right] \qquad (2.16)$$

where A_H is the Hamaker constant. The fitted results A_H=27×10^{-20} J and A_H=55×10^{-20} J, for DLC on diamond and UNCD on diamond, respectively. These values compare favorably with the reported reference value for diamond surfaces in a vacuum. The normalized effective work of adhesion shows a significant drop with increasing rms roughness of tips (Figure 2-6).

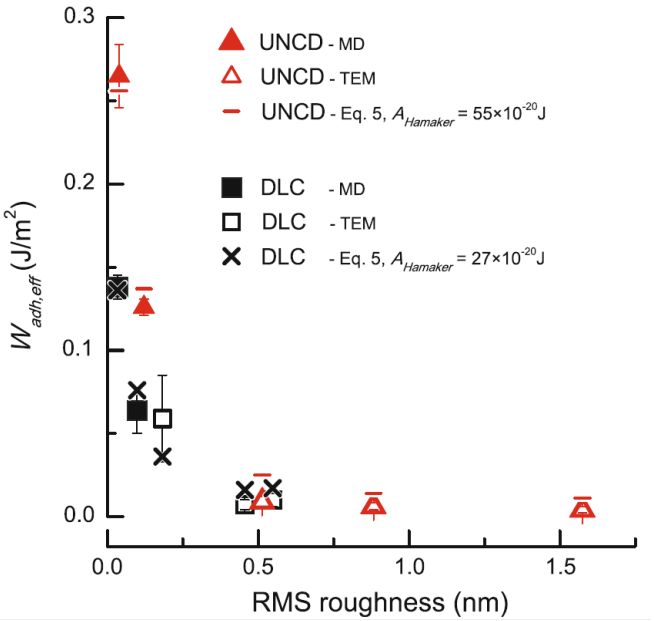

Figure 2-6. The normalized work of adhesion decreases as rms roughness increases from the atomic corrugation to the nanometer scale [32].

2.2 Nanoscale wear

Wear is a phenomenon of progressive loss of material due to relative motion between two contacting bodies. Wear is typically described empirically since the physical and chemical interactions at the interfaces are not fully understood at any scale [44]. In macroscale, the most broadly applicable wear model is Archard's wear law [59], which is expressed as

$$\Delta V = k_A F d \tag{2.17}$$

where ΔV is the wear volume, k_A is the Archard's wear rate, F is the applied normal load and d is the total sliding distance. The wear rate is usually obtained through experimental

measurements and is affected by numerous sliding conditions, such as temperature, sliding speed, surface topography and lubricant conditions [60], [61].

At the nanoscale, molecular dynamics [62] simulations of spherical DLC tips sliding against a DLC surface under loads of 4-102 nN showed a linear relationship between volume loss, and normal load and sliding distance, which is consistent with Archard's law. Several experimental investigations, however, suggest that Archard's law fails at the nanoscale [14], [42], [44], [63], [64]. The results show that the amount of wear volume is not proportional to the applied load, or the wear rate does not remain constant over sliding distance under constant load.

Yan et al. [14] carried out AFM wear tests on a PMMA surface with a Si tip. The sliding speed and the applied load were fixed at 80 μm/s and 70 μN. The Archard's wear rate varied dramatically from 0.01×10^{-6} to 7.8×10^{-6} mm^3/N mm, as shown in Figure 2-7. The wide range of wear rate measured under a constant load suggests that Archard's law is not particularly useful at the nanoscale.

Wear by an atom-by-atom attrition process has been demonstrated and a transition state theory has been proposed to model the nanoscale wear as a thermally activated bond formation and breaking process [40]. The rate of atom loss $\Gamma_{atom\text{-}loss}$ (unit s^{-1}) due to wear is expressed in an Arrhenius type equation:

$$\Gamma_{atom-loss} = f_0 exp\left(\frac{-E_a + V_a\sigma}{k_B T}\right) \tag{2.18}$$

where f_0 is the attempt frequency of the atom, k_B is Boltzmann's constant and T is the absolute temperature. The activation energy E_a is the stress-free activation barrier, σ is the stress component that lowers the activation barrier and V_a is termed as activation volume. Usually, V_a is used when shear stress is applied in the model [65]. If the normal contact stress is used in eq. (2.18), the effective activation volume V_{eff}, rather than V_a, is used [42], [43]. Similar to eq. (2.18), the experimental measured quantities, such as height loss rate, tip radius variation or volume loss rate, can be expressed as a function of stress using Arrhenius type equation.

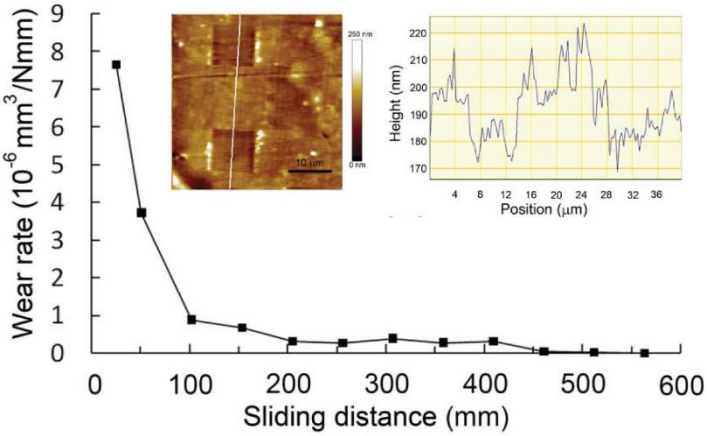

Figure 2-7. Archard's wear rate of PMMA as a function of sliding distance under a constant 70 μN load. The inset is the PMMA topography and profile along a line after 450 mm sliding [14].

To validate this mechanism, nanoscale wear experiments are required. AFM has been commonly used as a sophisticated apparatus for investigating the tribological behaviors at the nanoscale. Sheehan [66] studied the wear of single crystal NaCl by line wear tests using a Si_3N_4 AFM probe under different relative humidity and temperatures.

The line wear tests were carried out by sliding the AFM tip repeatedly along a 300 nm path over two NaCl steps. The distance between the steps, i.e. the recession of steps due to wear, was measured at the same time (Figure 2-8(a)). The AFM tip end was assumed to be spherical and the average shear stress was estimated from a contact mechanical model. The exponential relationship between the wear rate and the shear stress was observed under different relative humidity and two different temperatures (Figure 2-8(b)). Both humidity and temperature had a significant influence on the measured wear rate. By applying transition state theory, E_a=0.34±0.17 eV and V_a=86±6 $Å^3$ was obtained for NaCl. However, the dependence of wear rate on temperature in transition state theory is not yet determined, because: (a) there were only two temperatures used and large uncertainty in fitted activation energy, and (b) relative humidity, which also influenced the NaCl wear strongly, changed at elevated temperatures but couldn't be measured or controlled due to the configuration of the AFM used in this study.

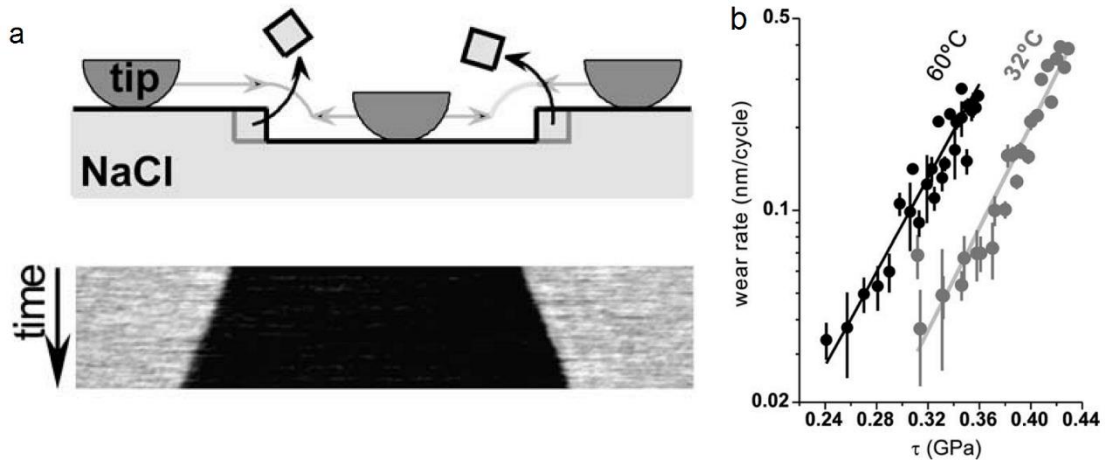

Figure 2-8. (a) A schematic of AFM tip sliding back and forth along a 300 nm line over two NaCl steps and the experimental results of the recession of two steps as they are worn by the tip, and (b) the wear rate versus shear stress at two temperatures [66].

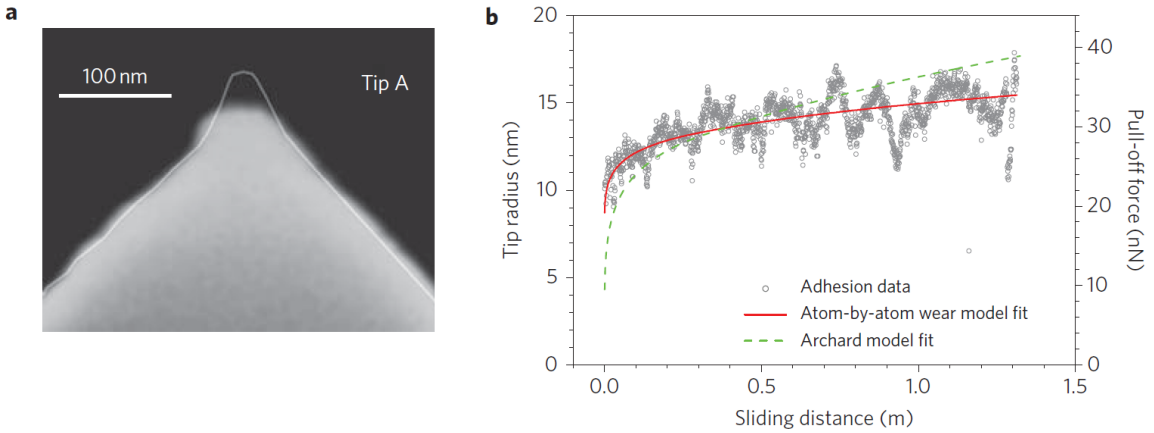

Figure 2-9. (a) SEM image of a DLC coated Si AFM tip after wear test and (b) the tip radius and pull-off force as a function of sliding distance during the wear test [42].

Bhaskaran et al. [42] applied transition state theory in an investigation of the wear of DLC coated Si AFM tip wear. In their experiments, the tips were slid against a SiO_2 surface under different loads (1.15-17.5 nN) for a total sliding distance up to 1 to 2 meters. SEM images of the tips were collected before and after the tests (Figure 2-9(a)). During

the wear tests, the pull-off forces were measured frequently through the experiments. The tip profile was assumed to be a truncated cone and the radius of the end was proportional to the pull-off force. In Figure 2-9(b), the experimental results and the fittings by Archard's law and transition state theory (atom-by-atom wear model) are presented. Consistent with eq. (2.18), the tip radius variation is expressed as:

$$\frac{\partial R}{\partial d} = \frac{\partial R}{\partial h}\frac{f_0 b}{\upsilon} exp\left(\frac{-E_a + V_a \tau}{k_B T}\right) \tag{2.19}$$

where d is the sliding distance and h is the truncated height of the cone, v is the sliding speed and b is a characterized length, typically the length of Burgers vector 2.5-6 Å [40]. The fitting results indicate that the measured data are better described by transition state theory.

In order to measure the tip profile during experiments more precisely, TEM has been used for high resolution tip profile measurements in *ex-situ* [28], [67] and *in-situ* experiments [44]. Jacobs and Carpick [44] carried out *in-situ* wear tests, where the Si AFM tips were brought into contact and slid against a diamond flat surface inside a TEM. High resolution TEM images of the tips were taken periodically during the experiments. The profile of the tips were traced and demonstrated a gradual tip profile evolution as shown in Figure 2-10(a). This *in-situ* method provided accurate and direct tip profile measurements. To quantify the volume removed, these 2D profiles were integrated to give 3D shapes by assuming axisymmetry of each differential slice. The contact radius was estimated by DMT contact mechanics model and thus the average contact stress was calculated. Figure 2-10(b)

indicates the reaction rate (i.e. atom loss rate) is fit well by an exponential relationship (eq. (2.18)) for all data collected from AFM tips with different profiles. The activation energy and volume were fitted as 0.91±0.06 eV and 6.7±0.3 Å^3, respectively.

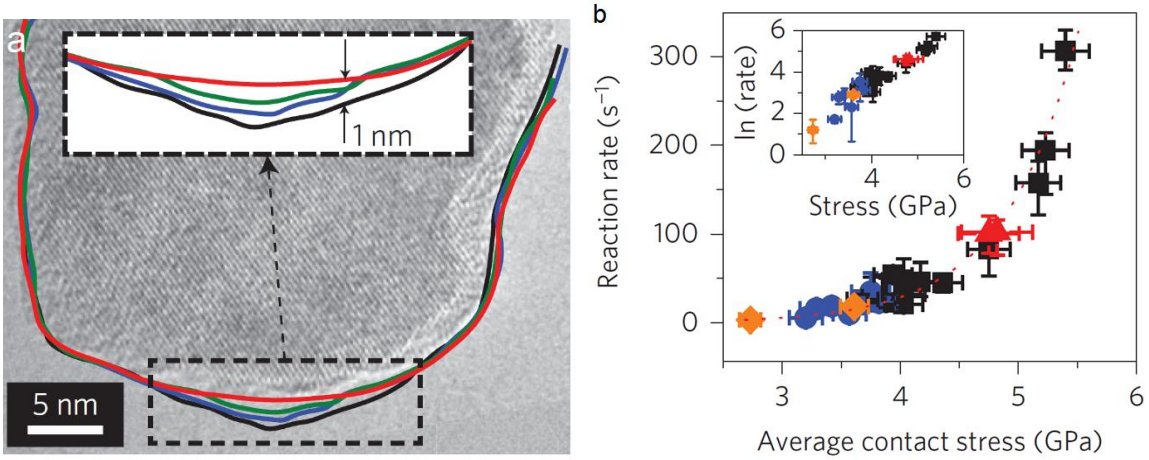

Figure 2-10. (a) TEM image of Si AFM tip with four traces of tip profiles at 200 nm intervals of sliding distance, and (b) the reaction rate (atom loss rate) as a function of average contact normal stress [44].

As expected from transition state theory, the nanoscale wear experiments indicate an exponential relationship between wear quantities (such as volume loss, height loss or atom loss rate) and stress. One thing to be noted is that the average stress is used to describe the stress in eq. (2.18). However, eq. (2.18) is the atom loss rate within a unit of area in contact. The experimentally measured atom loss rate is fit to:

$$\overline{\Gamma_{atom-loss}} = \frac{1}{N}\sum_{i=1}^{N}\Gamma_{atom-loss-i} = \frac{1}{N}\sum_{i=1}^{N} f_0 exp\left(\frac{-E_a + V_a\sigma_i}{k_B T}\right) \qquad (2.20)$$

where N is the total number of area units in contact, the subscript i indicates different unit of contact area. When the stress at the interface is not uniform, eq. (2.20) does not

necessarily equal $f_0 exp\left(\frac{-E_a+V_a\sigma}{k_B T}\right)$. To estimate the atom loss rate, the stress distribution rather than an averaged value may be more appropriate. The discussion on stress distribution and average stress will be detailed in Chapter 4. Moreover, the dependence of wear behavior on many experimental conditions, like temperature, relative humidity and sliding distance needs further investigation.

CHAPTER 3: Characterization of nanoscale adhesion

3.1 Introduction

Adhesion in nanoscale contacts is a ubiquitous and well-known phenomenon that is important in many applications, including microelectromechanical systems (MEMS), fibrillar adhesives, and AFM-based metrology and manufacturing processes. Adhesion at the nanoscale is often characterized through simple AFM-based pull-off force measurements in which an AFM tip (radius of 5 to 100 nm) is contacted to a surface and then subsequently retracted. The force is measured via the deflection of the compliant AFM cantilever and the pull-off force is defined as the peak attractive force during retraction of the tip from the surface. If the AFM tip is paraboloidal in shape, the work of adhesion is proportional to the pull-off force divided by the tip radius and can be calculated using one of the adhesion mechanics models, such as JKR [48], DMT [49], or Maugis-Dugdale [51], discussed in Chapter 2. The tip size as well as the elastic and adhesion properties of the contact determine which adhesion model is appropriate [68].

AFM pull-off force measurements are commonly used to characterize adhesion at the nanoscale because of their simplicity and the widespread availability of AFMs. However, the single value of work of adhesion that is obtained from pull-off measurements does not completely define the adhesion between two surfaces. Adhesion is more fully described by a traction-separation relation [33], [51], [52], [69], [70], such as a Lenard-Jones potential [71], that defines the adhesive stress as function of separation distance

between the surfaces. While the work of adhesion is the integral of the traction-separation relation, the work of adhesion does not provide direct information on magnitude of adhesive stresses or the adhesion range, which are critical in the design and engineering of nanoscale contacts. For example, the adhesion range relative to the surface roughness magnitude is critical in determining whether or not two surfaces will adhere when brought into contact under light loads (e.g., the bonding of semiconductor wafers [72]). Surface force-mediated adhesion typically has a range on the order of nanometers and the adhesive stresses increase sharply over short distances near the surface, thus measurement of the traction-separation relationship is challenging. Traditional AFM-based pull off force measurements cannot be used to obtain information on the adhesion range as the compliant AFM cantilever snaps in and out of contact during approach and separation [73]. Specialized measurement systems, such as the interfacial force microscope [74], [75], have been developed to avoid the snap-in/out phenomena and measure the traction-separation relation, however, these systems are difficult to use and not widely available.

While an AFM tip is often idealized as a smooth paraboloidal asperity, real AFM tips often have nanoscale roughness and complex 3D shapes due to manufacturing variations and changes in geometry that occur during fabrication [67]. Nanoscale surface roughness, can have a profound influence on adhesion [35], [55], [56], [58]. Jacobs *et al.* [32] combined molecular dynamics simulations and *in-situ* TEM adhesion experiments to investigate the effect of tip roughness on the adhesion of UNCD and DLC AFM tips to a diamond surface. Tip roughness, which was measured in 2D through high resolution TEM

imaging, was shown to have a significant impact on the work of adhesion determined from the pull-off force - the measured work of adhesion decreased by more than an order of magnitude as tip roughness increased from 0.03 nm to 0.5 nm. On a larger scale, Grierson *et al.* [31] investigated the effect of the overall geometry of AFM tip on adhesion and demonstrated that the tip evolves from a paraboloidal shape to a power law geometry with repeated sliding. The change in geometry, which was measured via TEM imaging, was exploited to extract information about the adhesion range of the AFM tip-sample contact [31]. A key limitation in both of these previous studies has been that the geometry of the tip was only characterized in 2D via TEM imaging. The lack of 3D geometry information limits the analysis that can be done to account for the effect of tip geometry when applying mechanics models to extract information about the adhesion of the contact.

In this Chapter, I present a novel approach for measuring the properties of the traction-separation relationship of nanoscale contacts with AFM by combining pull-off force measurements with high-resolution measurements of the 3D geometry of the tip. Specifically, we show that the properties of the traction separation relationship, namely the work of adhesion, adhesion range, and peak adhesive stress, can be extracted from pull-off force measurements of multiple tips with known (i.e., measured) complex geometries. These measurements are accomplished in the presence of snap-in/out by exploiting the sensitivity of the pull-off force to the nanoscale geometry of the tip.

The technique is demonstrated through adhesion measurements of UNCD tips in contact with PMMA surfaces. The UNCD-PMMA interface is technologically relevant as

UNCD AFM probes are used in tip-based nanometrology and nanomanufacturing processes and PMMA is a common polymer used in nanofabrication. UNCD is a polycrystalline diamond material made by chemical vapor deposition that has high hardness and wear resistance [28], [76]–[78]. Thin films of PMMA are used as resists in e-beam lithography [18], [20] and tip-based nanolithography [1], [4], [12], [14], [15]. More generally, PMMA is an amorphous thermoplastic with good transparency, chemical resistance, and high dimensional stability [23], [24]. As such, PMMA has a range of applications outside of nanofabrication, including as a component in nanocomposites [23], [25], bone cements [26], [27], and MEMS and NEMS [13], [14], [17], [21].

3.2 Experimental methods

The 3D geometry of each AFM tip used was measured via inverse imaging. The inverse images were collected by scanning the AFM tips over a structured silicon sample containing multiple high-aspect ratio spikes (TGT-01 from NT-MDT®). The scans were done under contact mode with a low load (~3-5 nN) and the image size varied from 100x100 nm^2 to 1x1 μm^2 in order to obtain the detailed features near the apex or the overall tip geometries. For each of the AFM tip used in this thesis, several images have been taken before and after the experiments over different spikes. The spikes are spaced ~2.2 μm apart and have a sharp radius (<10 nm) at the end. If the radius of spike is much smaller than the radius of the AFM tip, scanning over a single spike results in an image of the 3D geometry

of the AFM tip [79]. The finite radius of the spikes prevents the inverse images from measuring atomic scale roughness, however many detailed short wavelengths features are obtained. Importantly, compared to scanning electron microscopy (SEM) or TEM which have been used in previous studies [31], [32], [77] for tip characterization, inverse imaging provides a measurement of the 3D geometry of the tip rather than a 2D profile view. Furthermore, this inverse imaging method is simpler and more convenient than TEM or SEM imaging.

Pull-off forces between three different UNCD AFM tips (cantilever type: CTCT2, CTCT1 and SSCRL from Advanced Diamond Technologies Inc.) and a PMMA surface were obtained using a standard AFM (Bruker Dimension Icon®). The PMMA surface was fabricated by spin coating PMMA photoresist (PMMA-A4-495 from MicroChem®) at 5000 rpm for 50 s on top of a silicon wafer and then was heated on a hotplate at 180 ^{o}C for 10 min. The spring constants of the AFM cantilevers were determined via the thermal tune method [80]. Pull-off force measurements were performed by displacing the tip into contact with a PMMA sample until a specified maximum normal load was reached and then retracting the cantilever from the surface. The pull-off forces were recorded as the maximum adhesive force observed in the force-displacement curves during retraction. The approach and retraction speeds were fixed at 500 nm/s in all tests. The maximum applied loads were varied from ~3.5 nN to 100 nN for each tip. The tests at different loads were performed in an arbitrary order. A minimum of 20 measurements were taken at each load for each tip. Each measurement was done at a new location on the PMMA sample.

3.3 Experimental results

3.3.1 Measurements of AFM tip 3D geometries

An example 3D tip geometry measurement obtained using inverse imaging is shown in Figure 3-1a. By varying the scan size (lateral dimensions of the AFM image) and spatial resolution, the overall geometry of the tip (Figure 3-1(a)) as well as the features at the apex of the tip (Figure 3-1(b)) were obtained. High resolution TEM images of the end of this same tip were taken and the edge was traced, as shown in Figure 3-1(c), to extract the profile of the tip. In Figure 3-1(b) and (c), the same features at the apex of the tip are observed in both the TEM and the inverse AFM image, validating the inverse imaging approach. A projection of the inverse AFM image along the horizontal (fast scanning) direction is compared with the TEM profile in Figure 3-1(d). Considering the possibility of a slight difference in the observation angle in TEM and that the inverse image was projected to a specific plane, the profile data from both methods agree quite well with one another.

Three UNCD tips with significantly different geometries at the tip apex were used in this study. The inverse images of each tip over a ~40x40 nm^2 area are shown in Figure 3-2 and show that the geometries at the apexes of these three tips are significantly different from one another. The non-axisymmetric geometries of the tips, notably, Figure 3-2(b),

illustrate the importance of using the 3D geometries in the analysis of pull-off forces rather than a simpler 2D profile.

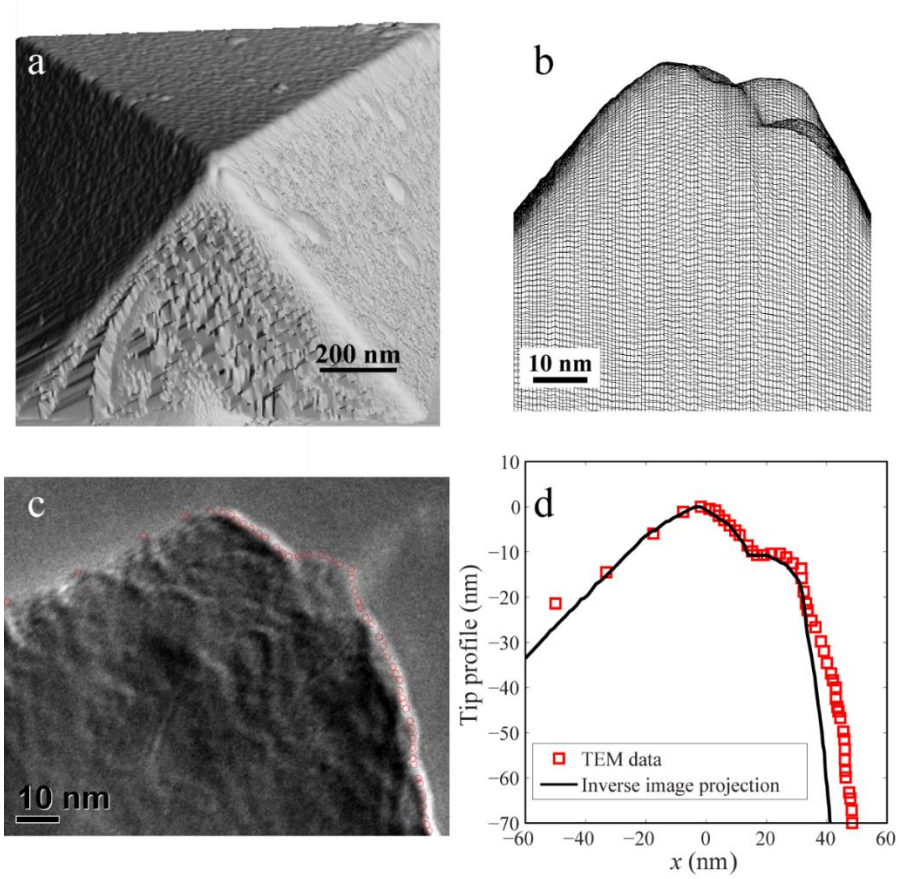

Figure 3-1. Characterization of geometry of AFM tip 2 showing (a) 3D view of inverse AFM image of tip, (b) 2D view of inverse image of tip, (c) TEM image of tip, and (d) the quantitative comparison of the tip profiles measured with TEM and AFM-based inverse imaging.

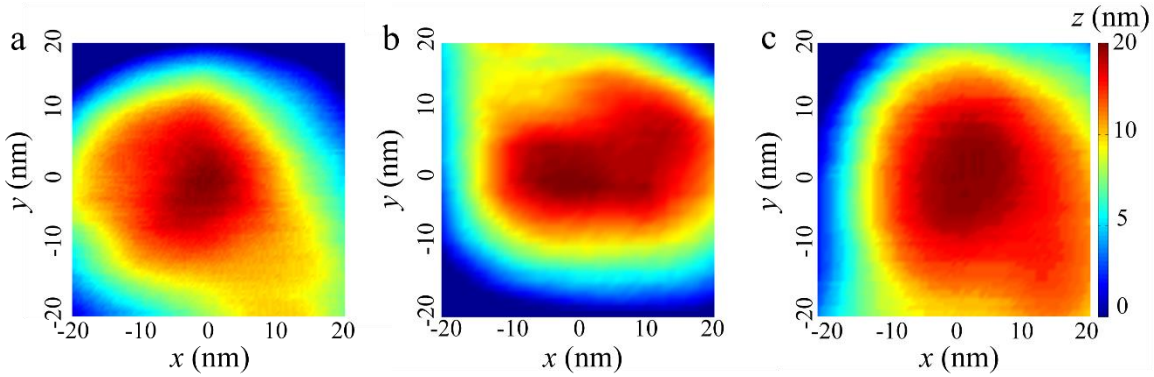

Figure 3-2. Height maps showing the 3D geometry of the apexes of the three UNCD AFM tips used in the current study: (a) tip A1, (b) tip A2 and (c) tip A3.

3.3.2 Pull-off force measurements

The measured pull-off forces for the three UNCD AFM tips are summarized in Figure 3-3. The maximum applied normal load, L, during contact was varied from ~3.5 nN to ~100 nN (compressive) for each of the tips. A sublinear trend of increasing pull-off force with increasing normal load was observed for each tip. The pull-off force data, F_p, data was fit using to an equation of the form: $F_p(L)=F_0+\alpha L^{1/3}$, as shown in Figure 3-3. The index of 1/3 was chosen as it resulted in robust fits over all of the data, however a dependence on the applied load to the 1/3 power was previously reported by Restagno *et al*. [81] for Pyrex to Pyrex adhesion measurements. The increase in pull-off force with normal load is likely due to plastic deformation that occurs during in the contact during the test [81]. The parameters F_0 and α were determined for each tip from the fits shown in Figure 3-3. The pull-off force in the absence of plastic deformation is taken as F_0, which is the pull-off force corresponding to L=0. Plastic deformation would complicate the subsequent adhesion analysis, thus F_0 is used as the pull-off force in all adhesion calculations. The parameter α,

with units of $nN^{2/3}$, is related to the geometry and elastic properties of the contacting bodies [81], thus this quantity is expected to vary for the three different tips used here. For the three tips, the fitting parameters are F_{01}=5.09 nN, F_{02}=7.46 nN and F_{03}=8.32 nN, and α_1=0.3 $nN^{2/3}$, α_2=0.27 $nN^{2/3}$ and α_3=2.71 $nN^{2/3}$, where the subscripts denote the tip number.

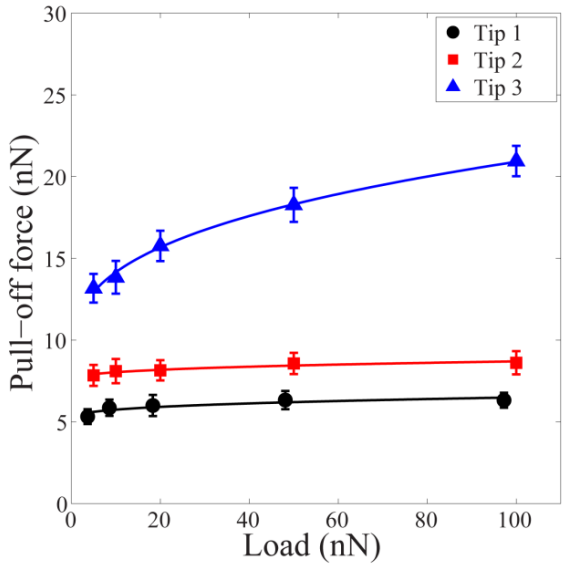

Figure 3-3. Measured pull-off force from a PMMA surface as a function of applied normal load for the three AFM tips. Each point represents the average of 20-25 measurements and the error bars represent the standard deviation. The solid lines are fits to the data; the form of the fit is $F_p=F_0+\alpha L^{1/3}$.

3.4 Analysis and discussion

3.4.1 Characterization of traction-separation laws

In order to analyze the measurements, two commonly used traction-separation relations are considered. The Dugdale traction-separation law [51] assumes the adhesive

stress, σ_D, acting on the surfaces is constant over a fixed separation range, h_{ad}, and then abruptly drops to zero (Figure 3-4). The adhesive stress is related to the adhesion range by the work of adhesion, W_a, as

$$\sigma_D = \frac{W_a}{h_{ad}} \tag{3.1}$$

This simple tractions separation relation has been widely applied in adhesion and fracture mechanics models.

A second common traction-separation relation often used to describe surface-force mediated adhesion is the 3-9 Lennard-Jones traction-separation law (Figure 3-4). This traction-separation relation describes the adhesion as:

$$\sigma_{LJ}(s) = \frac{8W_a}{3z_0}\left[\left(\frac{z_0}{s+z_0}\right)^3 - \left(\frac{z_0}{s+z_0}\right)^9\right] \tag{3.2}$$

where $\sigma_{LJ}(s)$ is the stress as a function of separation, s, and z_0 is the equilibrium separation. This traction-separation law has also been frequently used in analysis of adhered contacts [69], [70]. The 3-9 Lennard-Jones relation is more realistic than Dugdale relation, since it is determined by integrating the common 6-12 particle-particle potential over two half spaces [82] and captures the features of finite repulsive compliance at small separation and continuously decreasing attraction for larger separation [83]. In this study, the zero separation (s=0) is set to satisfy equilibrium, i.e. $\sigma_{LJ}(0)=0$. The stress is adhesive for $0<s<\infty$.

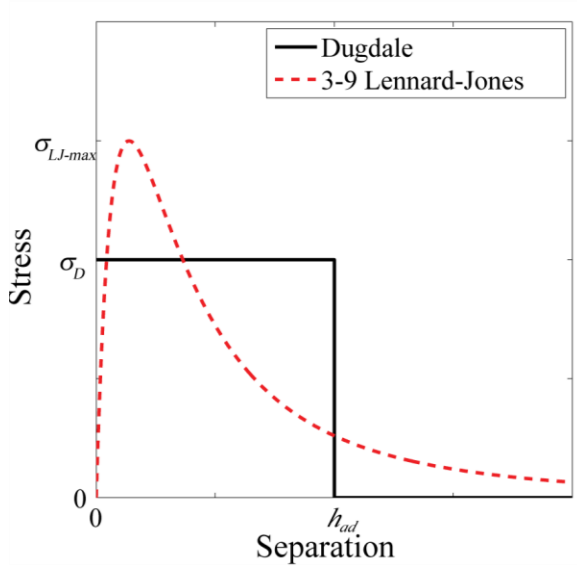

Figure 3-4. A schematic of Dugdale and 3-9 Lennard-Jones traction-separation laws. Both have the same work of adhesion.

The measured pull-off forces are analyzed by considering the traction-separation law at the interface and the geometry of the tip. If the adhesive stress is small enough, the elastic deformation in the contact will be negligible and the tip and sample can be treated as rigid bodies. We treat the bodies as rigid in the analysis below and then validate this assumption via finite element (FE) analysis later in the paper. For a rigid tip and Dugdale traction-separation law, F_0, the force at separation is calculated as:

$$F_0 = \int_{dA} \sigma_D dA_p = \sigma_D A_p(h_{ad}) \tag{3.3}$$

where A_p=$A_p(h)$ is the bearing area of the tip at a height h. h is measured from the apex of the tip. For all three UNCD tips, an identical value of σ_D is expected. Thus, the $F_0/A_p(h_{ad})$ should be constant across all three tips.

To analyze the data from the three tips, the adhesion range h_{ad} was varied from 0.1 nm to 4 nm with an increment of ~0.02 nm. The bearing area $A_{pi}(h_{ad})$ was calculated based on the 3D AFM tip geometries for all three tips, with the subscript i=1, 2 or 3 denoting the tip number. Finally, for the convenience of comparing the tips, the values of $F_{0i}/A_{pi}(h_{ad})$ are normalized by $F_{01}/A_{p1}(h_{ad})$ and plotted as a function of adhesion range. The three curves intersect at two values of h_{ad} as seen in Figure 3-5. However, the steepness of the curves at short ranges reduces our confidence in the intersection point around h_{ad}=0.5 nm. The second intersection point suggests that the adhesion range is between 2.46 and 2.49 nm. The work of adhesion and adhesive stress corresponding to the second intersection is W_a=49.6±0.8 mJ/m^2 and σ_D=20.1±0.4 MPa.

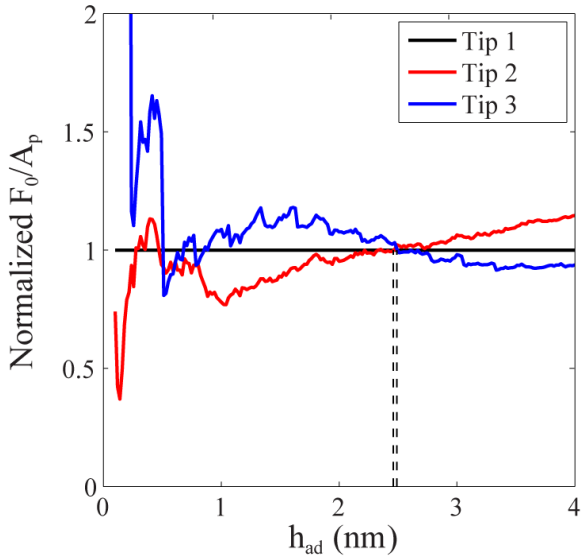

Figure 3-5. Normalized values of $F_0/A_p(h)$ as a function of adhesion range for all three tips. The dashed lines indicate the region over which the curves intersect: 2.46≤ h_{ad} ≤ 2.49 nm.

Similarly, under the assumptions of negligible elastic deformation, F_0 assuming a 3-9 Lennard-Jones traction-separation relation is

$$F_0 = \int_{dA} \sigma_{LJ} dA_p = \frac{8W_a}{3z_0} \int_{dA} \left[\left(\frac{z_0}{h+z_0} \right)^3 - \left(\frac{z_0}{h+z_0} \right)^9 \right] dA_p = \frac{8W_a}{3z_0} A_I \tag{3.4}$$

where the integral $A_I = \int_{dA} \left[\left(\frac{z_0}{h+z_0} \right)^3 - \left(\frac{z_0}{h+z_0} \right)^9 \right] dA_p$, is obtained by integrating from h=0 to a cut-off separation of h=5z_0. The values of W_a and z_0 should be identical for all three tips in this study. Thus, F_0/A_I is expected to be constant. Since the integral A_I is a function of z_0, F_0/A_I varies at different z_0 values. In Figure 3-6, the F_{0i}/A_{Ii} values, normalized by F_{01}/A_{I1}, as a function of z_0 are shown. A z_0 between 1.53 and 2.02 nm is suggested from the curves in Figure 3-6. The work of adhesion and maximum adhesive stress were solved using these z_0 values and eq. (2) and (4): W_a=51.4±2.4 mJ/m^2 and $\sigma_{LJ\text{-}max}$ =30.4±5.3 MPa.

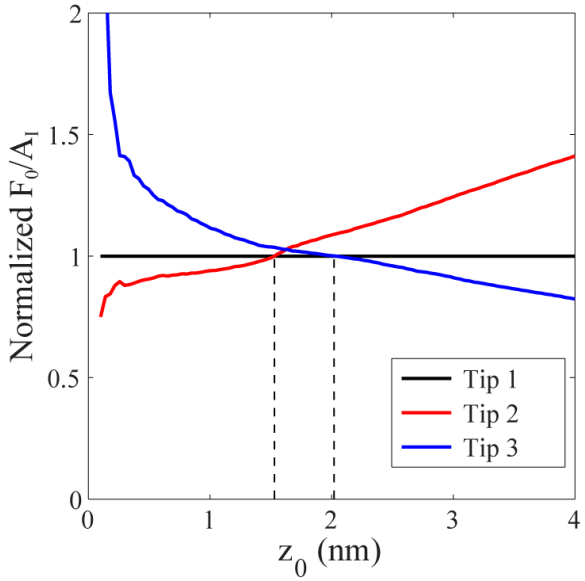

Figure 3-6. Normalized values of F_0/A_I as a function of z_0. The dashed lines indicate the region over which the curves intersect: 1.53≤ z_0 ≤ 2.02 nm.

Table 3-1. The measured adhesion properties between UNCD AFM tips and a PMMA surface extracted assuming two different traction-separation relations.

Traction-separation law	h_{ad} , z_0 **(nm)**	W_a **(mJ/m^2)**	σ_D , $\sigma_{LJ\text{-}max}$ **(MPa)**
Dugdale	2.46 - 2.49	49.6 ± 0.8	20.1 ± 0.4
3-9 Lennard-Jones	1.53 - 2.02	51.4 ± 2.4	30.4 ± 5.3

As summarized in Table 3-1, the analyses from both the Dugdale and 3-9 Lennard-Jones traction-separation laws yield similar values of work of adhesion for the UNCD-PMMA interface. The maximum adhesive stress in the 3-9 Lennard-Jones traction-separation law is about 1.5 times larger than the uniform stress in Dugdale interaction. Grierson *et al*. [31] discussed the effect of the form of the interaction on adhesion. The Dugdale and 3-9 Lennard-Jones traction-separation laws were considered as equivalent to each other when both had the same work of adhesion and the stress $\sigma_{LJ-\max} = \sigma_D$. However, this study suggests that $\sigma_{LJ-\max} \approx 1.5\sigma_D$ for equivalent Dugdale and 3-9 Lennard-Jones traction-separation relations. Using eq. (2), the equilibrium separation of 3-9 Lennard-Jones traction-separation law relates with the adhesion range of Dugdale traction-separation law as

$$z_0 = \frac{16}{9\sqrt{3}}\frac{W_a}{\sigma_{LJ-max}} \approx \frac{16}{9\sqrt{3}}\frac{W_a}{1.5\sigma_D} = 0.684h_{ad} \qquad (3.5)$$

The range of adhesion for the UNCD-PMMA system has not been reported previously. In other systems, interfacial force microscopy measurements indicate a range of adhesion 1.5-4.5 nm for (3-aminopropyl)triethoxysilane (γ-APS) on silicon [74]. In

silicon-diamond adhesion, the *in-situ* TEM experiments and analyses [33] resulted in adhesion range around 0.25 nm. In silicon-DLC and DLC-DLC, adhesion range of 4-5 nm was reported [31]. Regarding the differences in material and methods, we consider the extracted adhesion range (Table 3-1) in this work to be reasonable.

3.4.2 Finite element validation

The above analysis assumes that the elastic deformation in the tip and substrate at pull-off is small. In order to verify the validity of this assumption, finite element (FE) simulations, including the elasticity for both tip and sample, were performed. The geometries in the FE models were constructed from the inverse AFM images of the tips (Figure 3-1) by using a self-coded Matlab® script that generated an input file for Abaqus® with nodal positions defined from the inverse images. The elastic properties for UNCD are E_{UNCD}=790 GPa, $\nu_{UNCD} = 0.06$ [77] and for PMMA are E_{PMMA}=3.3 GPa , $\nu_{PMMA} = 0.4$ [84]. The adhesive stresses were applied as surface tractions in the FE models by a user-defined subroutine (Utracload). The magnitude of the stress was defined via a 3-9 Lennard-Jones traction-separation law (eq. (3.2)) with the parameters in Table 3-1. The surface tractions were applied when the separation between a node on the tip and its counterpart on the other surface was within the cut-off separation h=5z_0. The tip was displaced within a small range (-0.2 to 0.3 nm) vertically on top of the PMMA sample, from an initial

position in which the tip and sample were in contact at one point, and force on the tip was calculated.

The force-displacement curves calculated using the FE model are shown in Figure 3-7. The zero separation indicates the initial tip position in FE model. Positive displacement means that the tip is being pulled away from the surface. The pull-off forces are the peak values of three curves respectively. Elastic deformations occur in both tip and sample and thus result in a small displacement when reaching pull-off forces. The pull-off forces from experimental data are indicated by markers in Figure 3-7(a) for comparison. Although the FE predictions include elastic deformation, the experimentally measured pull-off forces are close to the FE predictions, indicating that the assumption of negligible elastic deformation in the adhesion analysis is reasonable.

The FE-predicted distribution of normal stress on the PMMA surface at pull-off for the three tips is shown in Figure 3-7(b-d), respectively. Positive values are tensile stress resulting from adhesion. The stress distribution has strong correlation with the 3D tip geometries as shown in Figure 3-2. Although there is compressive stress observed near the tip apex, the compressive stress only acts on small area and results in very little influence on the pull-off force as discussed above.

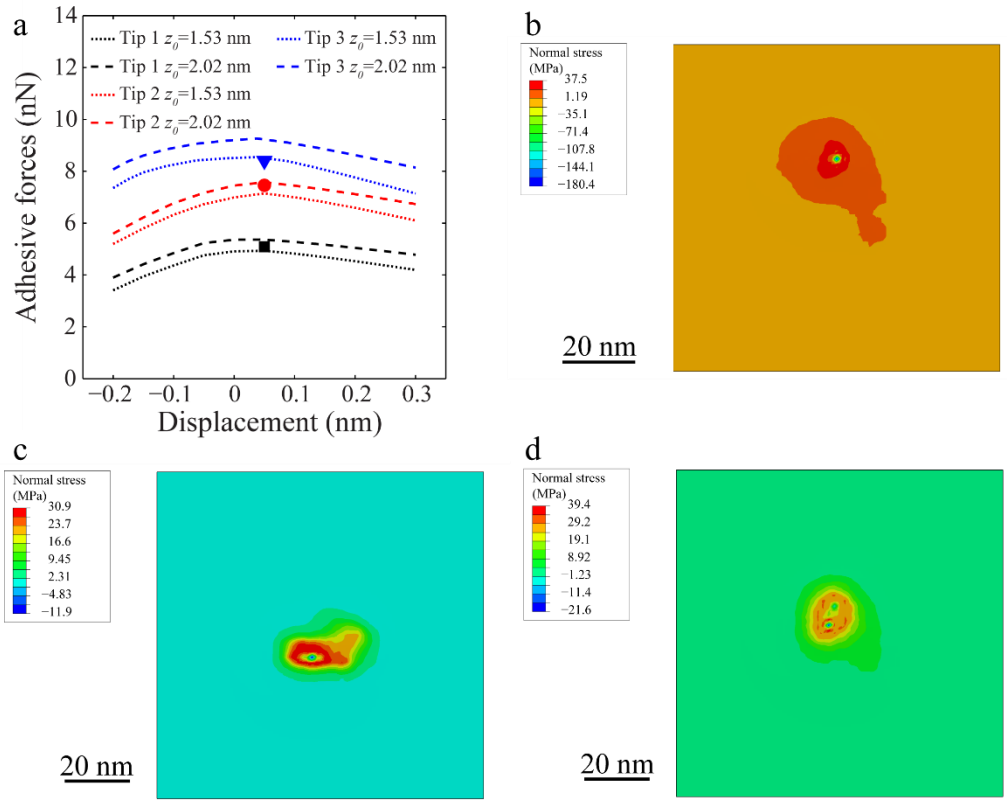

Figure 3-7. (a) FE-predicted adhesive forces (lines) between UNCD tips and PMMA as a function of displacement compared to pull-off forces from experiment (markers). And FE predictions of the distribution of normal stress on the PMMA surface at pull-off of (b) tip A1, (c) tip A2 and (d) tip A3.

3.5 Summary

We have quantified the properties of the adhesive traction separation relation of nanoscale UNCD-PMMA contacts using a new method that combines AFM pull-off measurements and detailed characterization of the 3D geometry of the AFM tip. The measurements were performed using three AFM tips with different geometries and the measurements from all three tips were combined in the analysis to obtain the properties of

the traction-separation relationship. The method requires measurements from a minimum of two tips with different geometries; three tips were used here to illustrate the overall robustness of the technique.

The measurement data was analyzed using two common traction-separation laws: the Dugdale relation and 3-9 Lennard-Jones relation. The Dugdale analysis resulted in h_{ad}=2.46-2.49 nm and W_a=49.6±0.8 mJ/m^2, while the 3-9 Lennard-Jones traction-separation law resulted in z_0=1.53-2.02 nm and W_a=51.4±2.4 mJ/m^2. Nearly the same work of adhesion is obtained regardless of whether the Dugdale or 3-9 Lennard-Jones traction-separation law is assumed. The peak stresses in the traction separation law differ by about 50%, suggesting that it may be more appropriate to set $\sigma_{LJ-\max} \approx 1.5\sigma_D$ instead of $\sigma_{LJ-max} \approx \sigma_D$ as is commonly done in analyses [31], [83] that define equivalent Dugdale and Lennard Jones potentials.

CHAPTER 4: Wear of PMMA at nanoscale at room temperature

4.1 Introduction

The tribological properties of PMMA are important in the selection of TBN parameters as well as the tribological performance of the AFM tips, which will influence the quality of the patterned nanostructures [14], [16], [28], [30]. Studies on the tribology of PMMA have been done at varying scales from millimeter down to micro/nano scale, including pin-on-disk tests [23], [25], nanoindentation and nanoscratch tests [30], AFM-based tests [13], [14], [37] and many other experiments [27]. The reported wear rates of PMMA vary over a wide range (~10^{-9} mm^3/N-mm to 10^{-4} mm^3/N-mm) due to the different compositions of the polymer and experimental conditions [14], [23], [25]. Archards' wear law, which suggests wear volume is linearly proportional to load, is often used in these studies. However, as discussed in Chapter 2, many of the experimental nanoscale wear studies showed disagreement with Archards' law [42], [43], [64].

Another important issue in nanoscale wear experiments on polymers is the debris and material pile-up produced by the contact and movement of AFM tip on the polymer surface [12]–[14]. Yan *et al.* [14] studied the influence of debris distribution on the static plowing performance. The debris, together with the wear of tip, changed the contact stress between ~12 GPa to ~4 GPa in a line scratch test. In Cappella and Sturm's study of dynamic plowing on PMMA [13], the debris produced by dynamic plowing had even larger volume than that of the patterned features. The fast oscillating tip broke the polymer chains during

dynamic plowing and resulted in the creation of the large undesirable border walls around the structures. An experiment design for reducing the influence of debris is necessary to fully understand nanoscale wear.

In this Chapter, wear experiments were carried out on PMMA thin films that were patterned by e-beam lithography. Gaps were formed between long rectangular structures for debris storage and tip cleaning. Load-controlled AFM wear tests were done by six ultrananocrystalline diamond (UNCD) AFM probes in order to reduce the effect of tip wear. The height loss rate of PMMA patterns were measured in line wear experiments, and volume loss rate in raster wear experiments. The 3D geometries of the ends of AFM tips were imaged by scanning over a "spiky" reference structure. Stress distributions on PMMA surface were calculated by finite element analysis (FEA) using the measured 3D geometries of the tips. In line wear tests, transition state theory was applied to describe the relationship of height variations and contact stress. The activation energy and effective activation volume were obtained from line wear data. These wear parameters were then used in a model to successfully estimate the volume loss rate in the raster wear tests.

4.2 Experimental Methods

Samples were prepared as follows. The PMMA (495PMMA A4 resist from MicroChem©) was first spin coated at a speed of 5000 rpm for 50 seconds to form a thin film (~100 nm) on top of a silicon wafer. The sample was prebaked at 180 ^{o}C for 10 minute

before patterning with e-beam lithography. In the e-beam lithography process, the patterns were written with a 150×150 μm^2 field with 20000×20000 dots in total. The exposure dose was set to ~500 $\mu C/cm^2$. Several fields were exposed at different locations using the identical e-beam parameters. Then the sample was developed in solution of 1:3 methyl isobutyl ketone (MIBK): isopropyl alchohol (IPA) for 1 minute.

The PMMA structures were characterized by AFM and SEM. The AFM images (Figure 4-1(a) and (b)) show long rectangular PMMA structures with width of ~200 nm. The gaps of uniform width of ~400 nm are formed between these structures. The silicon surfaces exposed in these gaps are flat and clean. The gaps allow debris to be captured during the wear tests and the exposed silicon surfaces can provide a reliable reference for accurate height measurements. In Figure 4-1(c), the SEM image shows repeated rectangular structures with uniform width. Therefore, we are able to carry out wear tests over the same structures at many different locations. Other patterns of ~500 nm wide long rectangles and 500×500 nm^2 squares (Figure 4-1(d)) were also made. The ~200 nm rectangular ones are used for line wear tests and the other patterns are used in raster wear experiments.

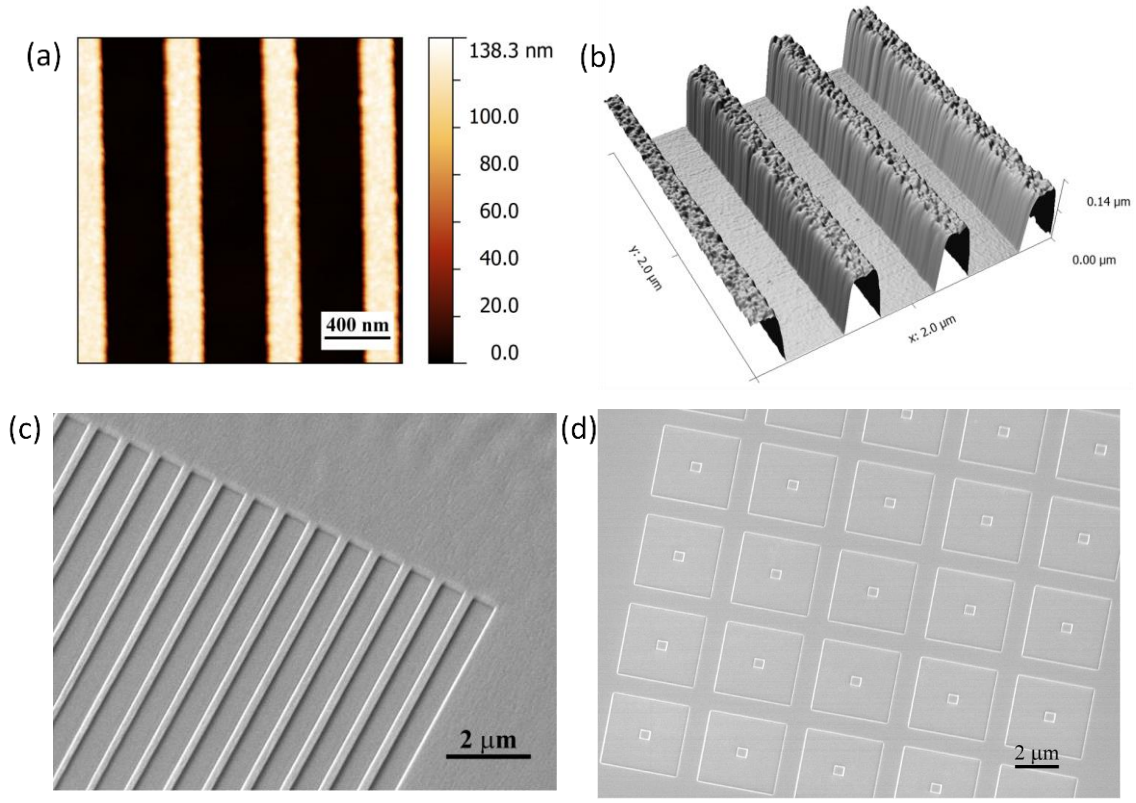

Figure 4-1. E-beam patterned PMMA structure characterized by (a) AFM image and (b) its 3D view, and SEM images of (c) rectangular patterns and (d) square patterns.

Six UNCD AFM tips from Advanced Diamond Technologies© were used in the wear experiments. In order to calculate the stress distribution at the tip-sample contact in the experiments, the tip geometry must be known. The 3D tip geometries were measured by using the inverse imaging of the AFM tips, which has been described in a previous chapter (Section 3.3.1). All 6 AFM tips in this study were imaged and found to have different 3D geometries, as shown in Figure 4-2. The AFM tips are denoted as L1, L2 and L3 for those used in line wear, and R1, R2 and R3 for raster wear experiments.

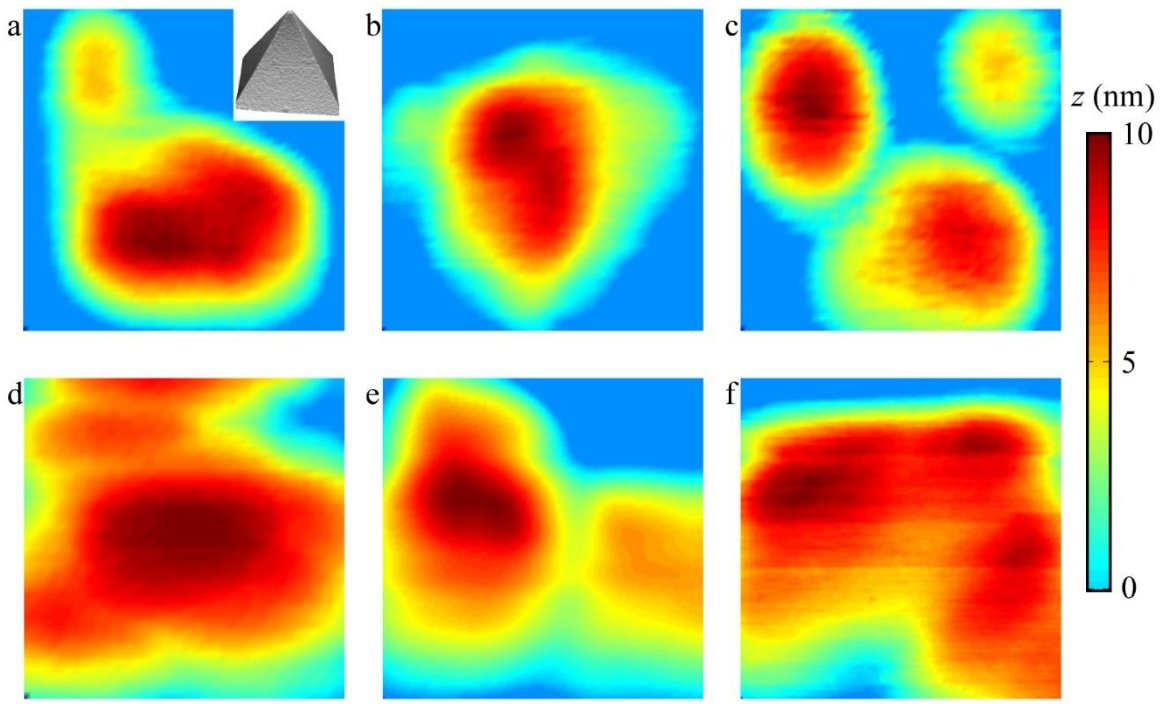

Figure 4-2. Height maps of 3D geometries of the apexes of UNCD AFM tips (a-c) L1-L3 and (d-f) R1-R3. Inset in (a) is a 3D view of the 4-sided pyramidal geometry of the tip measured at a scanning size of 1×1 μm^2. The 3D geometries are obtained by inverse AFM imaging technique. The size of each color map is 50×50 nm^2 and the height range is 10 nm.

Line wear experiments were performed using a Bruker Icon® AFM in ambient environment (temperature ~25 ^oC and relative humidity RH ~30%). The sample with ~200 nm wide rectangles was mounted such that the long rectangular structures were parallel to the long axis of the AFM cantilever. The AFM tip was then slid along a 1.5 μm path under load control for 128 passes. Each pass included one trace and one retrace. The sliding direction was along the fast scanning direction, i.e. the direction perpendicular to its cantilever. The 1.5 μm path was long enough to go over two PMMA lines as well as

some of the silicon reference plane. Three different normal loads were applied for three tips respectively.

Raster wear experiments were done using an NT-MDT® AFM and under dry nitrogen environment (<4% RH) and temperature control (27 ^{o}C). Ten scans of 1.5×1.5 μm^2 over ~500 nm wide rectangles or 1×1 μm^2 over 500×500 nm^2 square patterns were done using different tips at one location. The pattern's volume was measured from AFM images after height calibration based on the exposed Si wafer. Volume loss was then calculated by the difference of volume in a certain AFM image to that of the first scan image.

Both line and raster wear tests were performed under load control and repeated at several different locations. The sliding speed was kept as a constant of 3 μm/s for all experiments.

4.3 Experimental results

In line wear tests, an AFM tip was repeatedly scanned over the same path in the fast scanning direction in each wear test. Thus, the AFM image recorded the patterns' height as a function of time (which is proportional to scan distance). *In-situ* observations of the change in the geometry of PMMA structures as a function of time under different loads are shown in Figure 4-3(a-c). The reference silicon plane allows the raw data to be

processed by leveling the reference plane and thus the measurements on such AFM images are easier and more accurate compared to imaging a recess in a surface. In Figure 4-3(a-c), we observe the structure becoming thinner and shorter with increasing scanning for all three loads using tip 1. The results of higher load, such as 200 nN in Figure 4-3(c), show that the structures were worn faster at higher loads compared to lower loads.

Wear depths are measured from the change in height of the center of each PMMA pattern. In Figure 4-3(d), the wear depths for different normal loads are plotted as a function of scan loops. In each loop, the PMMA patterns experiences a sliding distance that is the width of the contact area, which will be determined from FE calculation in the following section. The solid lines are the wear depths averaged over 8-12 measurements at different locations and the dashed lines are standard deviations from averaged values for each loads respectively. Given the complicated contact conditions present during the wear tests, the data is quite stable and repeatable. There is a sub-linear dependence of wear depth on sliding distance in all three loads and the higher loads result in faster wear of the patterns. To understand this sub-linear behavior, consider the geometry of the contacting bodies. At the beginning of wear, the contact only happens at the end of tip and a plane PMMA surface. This asperity contact results in high contact stress. When the tip wears into the pattern, the contact area increases because of the 4-sided pyramidal geometry of the tip. Thus, the contact stress reduces, and leads to slower wear. Figure 4-4 shows a $2\times2\ \mu m^2$ AFM image taken after three wear tests. The three wear tracks are different due to different

loads, but all remain clean. The e-beam patterned gaps show their utility as debris distributes within the gaps.

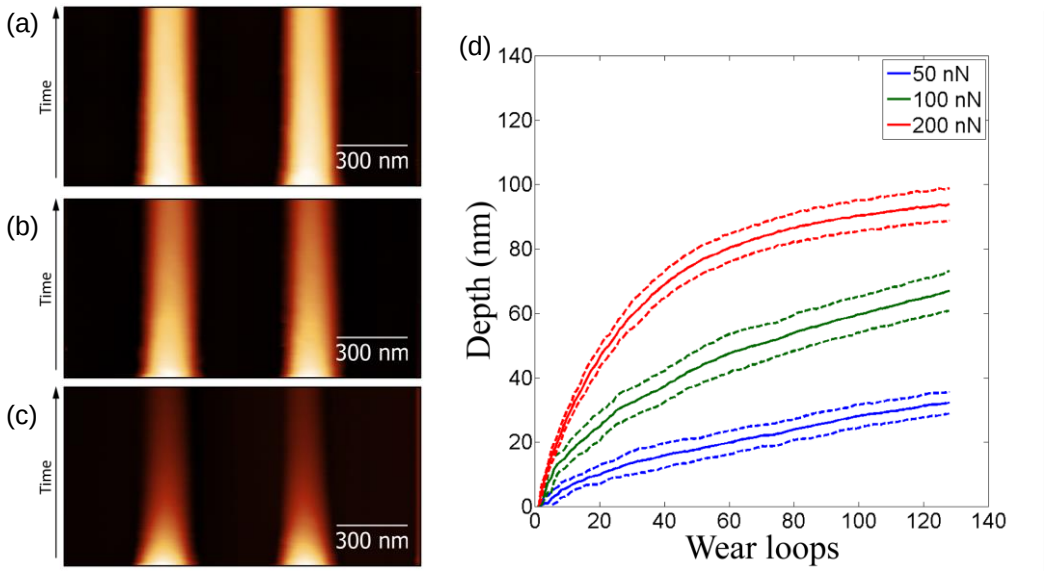

Figure 4-3. *In-situ* observations of geometry variations of PMMA structures as a function of time under load of (a) 50 nN, (b) 100 nN and (c) 200 nN, and (d) wear depth variations under different loads using UNCD tip L1.

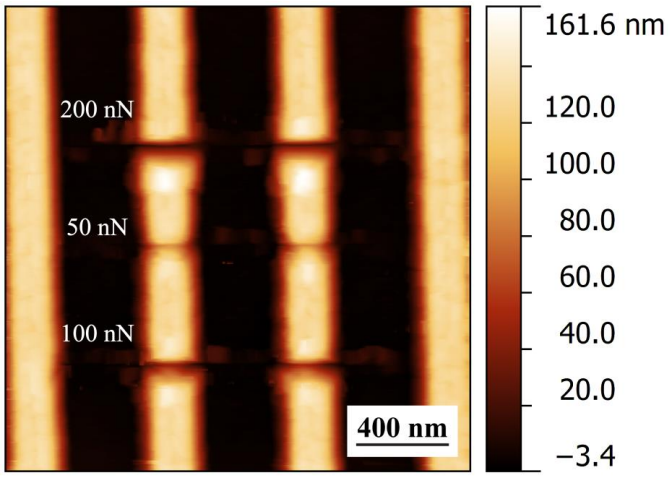

Figure 4-4. An AFM image after three line wear tests on PMMA sample. Debris are deposited on the silicon in the gaps.

In raster wear tests, tip R1-R3 were used. As shown in Table 4-1, the adhesion forces were measured and the applied loads were controlled during each experiment. Two different patterns were scanned. The AFM images were processed as described above so that the volume could be calculated based on the reference silicon plane. Volume loss rate is defined as volume loss per unit sliding distance on PMMA pattern. The volume losses as a function of sliding distance are shown in Figure 4-5.

Table 4-1. Summary of raster wear tests. All raster wear were done in a dry nitrogen environment.

Tip #	**Applied load (nN)**	**Adhesion force (nN)**	**Scanning pattern**	**Volume loss rate (nm^3/nm)**
R1	57.5 ± 5.7	27.9 ± 3.9	1.5×1.5 μm^2 over 500 nm wide rectangular patterns	7.7 ± 0.8
R2	14.9 ± 1.6	8.6 ± 1.0	1×1 μm^2 over 500×500 nm^2 square patterns	2.1 ± 0.3
R3	56.9 ± 8.3	25.0 ± 4.8		6.5 ± 0.4

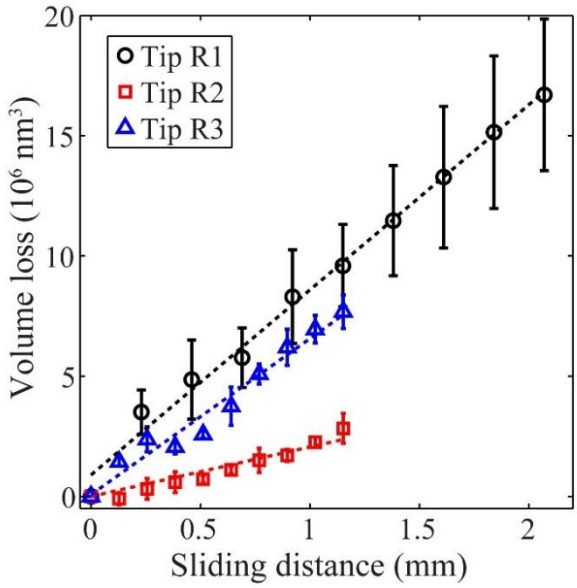

Figure 4-5. Volume loss as a function of sliding distance in raster wear tests.

4.4 Analysis and discussion

4.4.1 Stress analysis by finite element method

To understand the relationship between wear behavior and contact stress, FEA was used to calculate the stresses in the UNCD-PMMA contact. As mentioned in the previous chapter, we measured the 3D geometries of the UNCD tips using inverse AFM imaging. The 3D data was used to build the FE models of tips. The tips were ~100×100 nm^2 and had a cutoff height of ~30 nm. Considering the size of contact areas, the models were large enough to eliminate the boundary effects. The PMMA was modeled as a volume of size ~100×100×30 nm^3. Adhesion between UNCD and PMMA was applied as a surface traction [85] which followed a 3-9 Lennard-Jones traction-separation law. The bottom boundary of PMMA was fixed and the tips were displaced from the top down into contact with PMMA until the total loads reached the same values used in experiments. The constitutive behavior of the polymer is complex and not fully known, thus we considered two cases of constitutive behavior: a) pure elastic case, which would result in an upper bound prediction of contact stress, and b) ideal elastic-perfectly plastic case, which would result in a lower bound prediction of contact stress. The elastic properties were set at E_{UNCD}=790 GPa, ν_{UNCD}=0.06 and E_{PMMA}=3.3 GPa, ν_{PMMA}=0.4 based on reported values [77], [84], [86]. To determine the yield stress, AFM indentation tests, where a high load (300 nN) was applied on AFM tip and the area of permanent indent after tip withdrew, were performed. The yield stress was then estimated as 1/3 of the ratio of load to indented area.

FEA prediction of normal contact stress at the contact of UNCD tip L1 on a pure elastic PMMA under 200 nN load is shown in Figure 4-6. Both side view and top view are shown in 50% transparency. As indicated in Figure 4-6(a), the PMMA deforms and the contact stress is localized at the end of the tip. Due to the asymmetric geometry and the roughness on tip surface, an asymmetric distribution of contact stress is shown clearly in Figure 4-6(b). In fact, by only knowing the 2D profile of a tip, one usually assumes an axisymmetric geometry (or sometimes even ignore the roughness) and results in quite different stress distribution than that using the real 3D geometry.

We have also performed FEA for the case of ideal elastic-perfectly plastic PMMA. The results indicate larger contact areas and a more uniform stress distribution due to the plastic behavior. The distributions of normal stress and the contact areas for all 6 tips and different loadings are obtained from FEA.

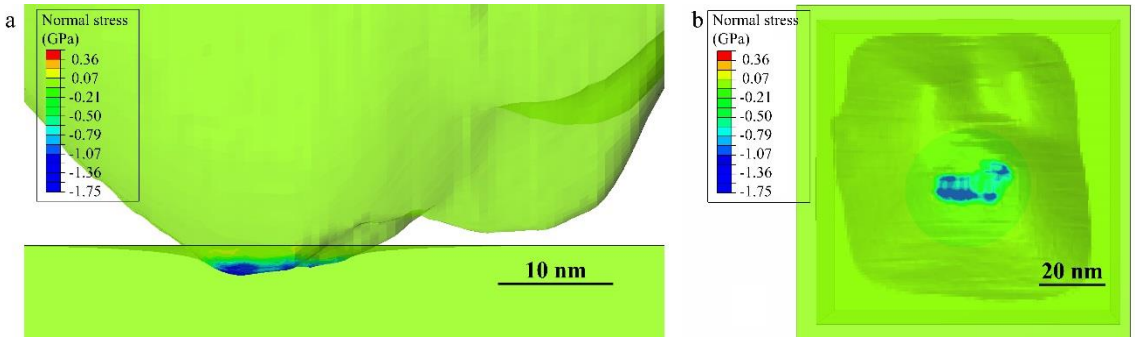

Figure 4-6. (a) Side view and (b) top view of FEA results of contact normal stress between UNCD tip L1 and PMMA under 200 nN load (shown in 50% transparency).

4.4.2 Application of transition state theory to line wear test data

Transition state theory has been applied to nanoscale wear analyses in previous studies of several different systems [40], [43], [44], [66]. In this theory, the removal of material is viewed as the system moving from a local potential energy minimum to another by overcoming an activation energy barrier. To describe this mechanism, an Arrhenius type function can be derived from [43], [44]:

$$\frac{\partial h}{\partial s} = \frac{b f_0}{v} exp\left(\frac{-E_a + V_{eff}\bar{\sigma}}{k_B T}\right) \tag{4.1}$$

where $\partial h/\partial s$ is the height loss, which is defined as height loss per unit sliding distance in this paper. The height loss rate is calculated as the initial slope of the curves in Figure 4-3(d) divided by width of the contact area from FE. v is the constant sliding velocity, b the magnitude of Burgers vector, and f_0 the attempt frequency. E_a is the activation energy barrier, V_{eff} the effective activation volume, k_B Boltzmann's constant, and T the absolute temperature.

The stress acting on the system reduces the activation energy barrier and thus facilitates the wear of material. Average normal stress $\bar{\sigma}$ is used in eq. (4.1) in one analysis in this study, as has been done in previous studies [42]–[44], [77]. However, I also investigate a transition state theory model that uses stress distribution to describe this atom-by-atom removal process.

From FEA, the normal contact stress at each point on a PMMA surface can be calculated. Thus, rather than taking a single averaged stress value, the normal stress

distribution is applied into the Arrhenius type function and then averaged to get height loss rate. A stress distribution model is proposed here:

$$\frac{\partial h}{\partial s} = \frac{bf_0}{v} exp\left(\frac{-E_a}{k_B T}\right) \frac{\sum_{i=1}^{N} exp\left(\frac{V_{eff}\sigma_i}{k_B T}\right)}{N} \tag{4.2}$$

where N is the total number of nodes in contact on PMMA surface. We define a function $g(V_{eff}, \sigma)$ to simplify eq. (4.2):

$$g(V_{eff}, \sigma) = \frac{\sum_{i=1}^{N} exp\left(\frac{V_{eff}\sigma_i}{k_B T}\right)}{N} \tag{4.3}$$

For raster wear, the relationship between volume loss rate and normal stress can be expressed as a function of the average stress in:

$$\frac{\partial V}{\partial s} = \frac{A_c bf_0}{v} exp\left(\frac{-E_a + V_{eff}\bar{\sigma}}{k_B T}\right) \tag{4.4}$$

and in terms of the stress distribution as:

$$\frac{\partial V}{\partial s} = \frac{A_c bf_0}{v} exp\left(\frac{-E_a}{k_B T}\right) g(V_{eff}, \sigma) \tag{4.5}$$

where A_c is the contact area. Both the average stress model and stress distribution model are used in the following analysis.

As mentioned in the previous section, two different constitutive behaviors of PMMA are considered in FEA. The stresses calculated from pure elastic assumption are analyzed by transition state theory for line wear experimental data first. The fitting results of transition state theory of model using average stress and stress distribution are shown in Figure 4-7(a) and (b), respectively. The solid green lines are the best fit curves with parameter b=4×10^{-10} m, f_0=10^{13} Hz and T=300 K. The activation energy E_a=0.67 eV and

effective activation volume V_{eff} =16 Å^3 are obtained from the average stress model, and E_a=0.67 eV and V_{eff} =11.3 Å^3 for the stress distribution model. In both cases, the transition state theory describes the wear behavior well. All data from three different tips fall into ±3% range (dashed green lines) of the best fitted activation energy values. The ideal elastic-perfectly plastic case is also analyzed using eq. (4.1) and eq. (4.2) and shown in Figure 4-7(c) and (d). Both models fit the data well and the activation energy and effective activation volume are calculated.

Since the upper and lower bounds of contact stress are given by assumptions of pure elastic and ideal elastic-perfectly plastic constitutive behavior of PMMA, the ranges of the activation energy and effective activation volume are determined. As shown in Table 4-2, the average stress model, eq. (4.1), results in 0.67 eV≤ E_a≤ 0.73 eV and 16 Å^3≤ V_{eff}≤ 51.8 Å^3. While the stress distribution model, eq. (4.2), results in 0.67 eV≤ E_a≤ 0.69 eV and 11.3 Å^3≤ V_{eff}≤ 24.8 Å^3. Comparing these ranges, the model using contact stress distribution shows its advantages by giving narrower ranges for both activation energy and effective activation volume. Due to the exponential form of the Arrhenius type function, small variations in these parameters can cause large changes in height loss rate. The narrower range obtained from model using contact stress distribution suggests the results of this analysis is precise.

Comparing the activation energy of several materials, diamond-like diamond (DLC) ~1.0 eV [42], silicon ~0.98 eV [43], calcite ~0.8 eV [63], PMMA ~0.68 eV (my

result) and NaCl ~0.34 eV [66], shows an increasing of wear resistance with increasing activation energy.

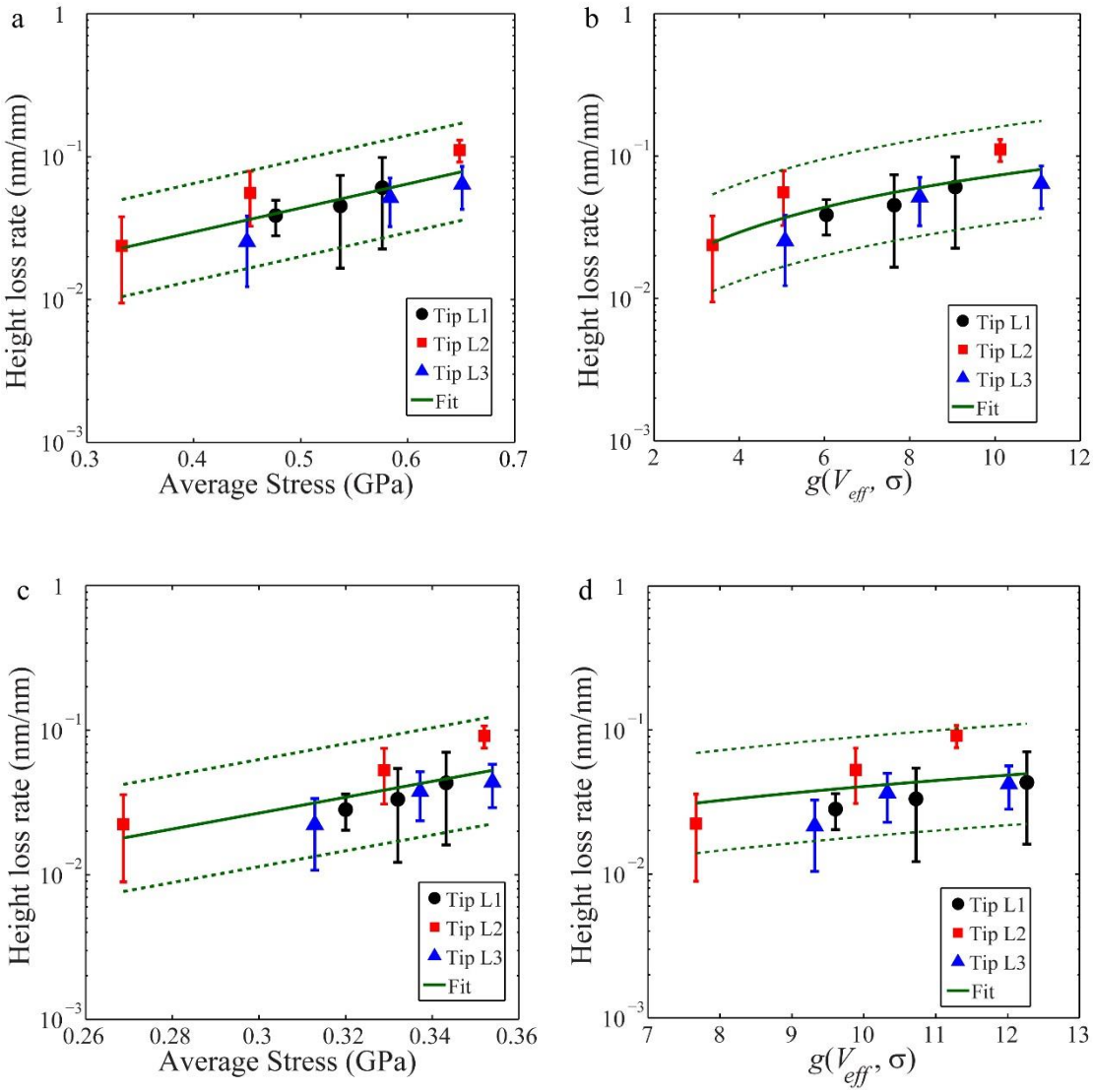

Figure 4-7. Results of fitting the transition state theory of model using (a) average stress and (b) stress distribution from FEA results of pure elastic PMMA assumption, and (c) average stress and (d) stress distribution from FEA results of ideal elastic-perfectly plastic assumption (dashed line: +/-3% of best fitted activation energy).

Table 4-2. Effective volume and activation energy fit from line wear tests data using average stress model and stress distribution model. Narrower ranges for both parameters result when using stress distribution model.

	Average stress	**Stress distribution**
Pure elastic	V_{eff}=16 Å^3, E_a=0.67 eV	V_{eff}=11.3 Å^3, E_a=0.67 eV
Ideal elastic-perfectly plastic	V_{eff}=51.8 Å^3, E_a=0.73 eV	V_{eff}=24.8 Å^3, E_a=0.69 eV

4.4.3 Volume loss prediction by transition state wear model

Instead of fitting a new set of parameters for raster wear data, we use the E_a and V_{eff} values, which are acquired from line wear tests, into transition state theory to predict the volume loss rate. Combined with corresponding FEA results of contact stress for these tips, the ranges of volume loss rate are estimated as shown in Figure 4-8. The red circles with error bar are the experimental data with standard deviation measured in raster wear experiments. The dashed box for each tip indicates the upper bound and lower bound of the volume loss rate prediction by average stress model (eq. (4.4)) and the deviation from the experimental data is 13%. Results from the stress distribution model (eq. (4.5)), which are shown by the solid boxes, shows a narrower range of volume loss rate and 7.8% deviation from the experimental data. Even though there are many differences in line wear and raster wear experiments, such as different AFM, tip geometries, experimental

environments and wear patterns, the application of transition state theory, with E_a and V_{eff} obtained from line wear tests, nicely predicts the ranges of volume loss rate relative to the experimental data in raster wear tests.

Although other mechanisms, such as chain removal or cluster detachment, are possible for polymer wear, the quality of line wear data fittings (Figure 4-7) and the agreement between experimental data and predictions of transition state theory in raster wear tests (Figure 4-8) suggest an atom-by-atom essence of wear process at nanoscale for PMMA thin films. By assuming the radius of an atom is 0.1 nm, an estimation indicates that there are 4.9 to 7.4 atoms removed from 1×1 nm^2 area by 1 nm sliding. This also implies that an atom-by-atom process is likely to occur.

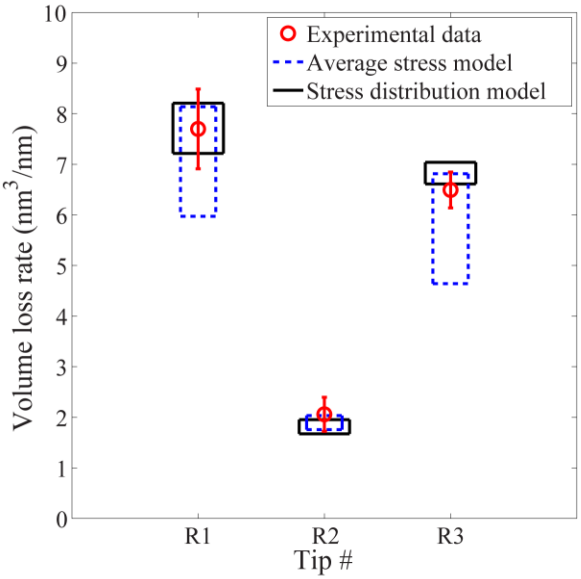

Figure 4-8. Comparisons between volume loss rate measured in raster wear experimental tests (circles) and that predicted by average stress model (dashed box) and stress distribution model (solid box).

4.5 Summary

Nanoscale wear tests were performed on e-beam patterned PMMA structures. Rectangular and square PMMA structures on a silicon wafer were fabricated. The gaps between PMMA structures allowed the wear debris to be captured during wear experiments. They also provided a flat and clean reference surface when measuring the height variations of patterns.

Load controlled AFM line and raster wear tests were performed using six different UNCD tips. The 3D UNCD tip geometries were measured using an inverse AFM imaging technique. FEA was used to calculate the normal stress distributions and contact areas on PMMA surface. The simulations included all tips, different normal loads and examined two cases of constitutive behaviors for the PMMA.

The line wear data was analyzed by transition state theory to extract activation energy and effective activation volume for PMMA using both average stresses and the contact stress distributions. The results indicated a good description of experimental data. The analyses using contact stress distributions resulted in narrower ranges of activation parameters, i.e. 0.67 eV$\leq E_a \leq$ 0.69 eV and 11.3 Å$^3 \leq V_{eff} \leq$ 24.8 Å^3. By taking these parameters, both transition state theory models result in estimations of volume loss rate ranges close to the experimental data in raster wear. The stress distribution model demonstrates a more accurate estimation than that of average stress model.

CHAPTER 5: Nanoscale wear at varying temperatures

5.1 Introduction

Wear models based on transition state theory have been applied in nanoscale wear studies of many materials, including silicon- and carbon-based materials [42]–[44], [77], as well as polymers (Chapter 4). In this mechanism, atom-by-atom attrition based on a stress assisted thermal activation process is assumed [44]. As suggested by the form of the transition state theory (for example eq. (4.4)), the temperature should have significant effect on the wear rate.

Sheehan [66] performed AFM wear experiments over NaCl steps in nitrogen environments at two different temperatures, 32 and 60 ^{o}C. With temperature variation, the data assesses changes in wear rate with temperature. The effect of temperature is consistent with the transition state theory, although there is a large error measured for activation energy E_a=0.34±0.17 eV for NaCl [66]. The uncertainty is mainly because of having only two temperatures over a limited range [40], [66]. However, all other studies, to my knowledge, that apply transition state theory to explain nanoscale wear behavior are performed at one fixed temperature. The effect of temperature on nanoscale wear has not been fully evaluated.

Moreover, variation of temperature in a relative small range can result in significant changes in mechanical properties of a polymer. For example, the properties of PMMA, such as Young's modulus and yield stress, can reduce by ~40% when temperature increases

from 30 ^{o}C to 70 ^{o}C [86], [87], and therefore results in different contact stress distributions. For tribological properties, friction for instance, the effect of temperature is also prominent due to the viscoelastic relaxations [88], [89] under or above glass transition temperature T_g. Hammerschmidt et al. [88] used temperature controlled friction force microscopy to characterize the friction between silicon AFM tips and polymer thin films. The results indicated a time-temperature equivalence on scan speed and temperature for friction measured on PMMA. The dependence of friction on temperature was attributed to the viscoelastic relaxations of polymers, namely the β-relaxations that happens below T_g. The energy to hinder the rotation of side chain of PMMA was measured as ~12 kcal/mol and friction data measured from different temperature falls into one master curve at 60 ^{o}C. Such effects have not been studied for nanoscale wear for polymer materials.

In this Chapter, AFM based wear tests on PMMA thin films are performed in a dry nitrogen environment at varying temperatures. The volume loss rate increases with increasing temperature. At elevated temperatures (~66 ^{o}C), the volume loss rate is twice as large as that at ~27 ^{o}C. The transition state theory models (eq. (4.4) and (4.5)) overestimate the volume loss rate at elevated temperatures and the overestimation can be as much as one order of magnitude higher. Modified transition state theory models are proposed by including a time-temperature superposition shift factor which is related to the viscoelastic relaxations of PMMA. The modified models result in much better matching to the experimental data.

5.2 Methods

The experiments were performed in an NT-MDT® AFM system with a heating stage and a chamber installed for temperature and environmental control. Dry nitrogen was filled into the chamber and the relative humidity is controlled <4% RH. The PMMA sample (T_g ~106 ^oC, prepared and patterned as described in Chapter 4.2) was mounted on the heating stage and the set temperature of the heating stage was varied from 30 ^oC to 80 ^oC. When set temperature was changed, a waiting time of at least 10 min was used to allow the temperature to be stabilize through the sample. The temperatures at the top of the PMMA film were measured by a thermocouple at different locations, different stabilized times (10 to 50 min) and different set temperatures. The set temperatures, T_{set}, and the PMMA surface temperatures, T_{PMMA}, are listed in Table 5-1. Note that when a UNCD probe is brought into contact with PMMA sample, the temperature at the contact location is expected to be reduced as UNCD has high thermal conductivity. However, the exact temperature at the contact is extremely difficult to measure experimentally due to the nanoscale size of contact.

Table 5-1. List of set temperatures of heating stage, measured temperatures on top of PMMA surface without an UNCD probe contacting sample, and FEA results of temperatures at the contact location of UNCD tip and PMMA surface. The values after ± are the standard deviation from multiple measurements at different locations and different stabilized time (10 to 50 min).

T_{set} (^oC)	30	50	70	80
T_{PMMA} (^oC) [no probe, measured]	28.2±0.31	44.0±1.28	59.2±0.19	67.1±0.31
$T_{PMMA\text{-}UNCD}$ (^oC) [with probe, simulated]	27.8	43.1	58.3	65.9

Thermal FEA simulations were performed in Abaqus® 6.9-EF. The model included two steps. In the first step, a model consisting of a piece of silicon wafer (600×600 μm^2 and 525 μm thick), a thin layer of PMMA (100 nm thick) and a layer of artificial thermal boundary of air was built (Figure 5-1(a)). The temperature at the bottom surface of silicon wafer was fixed as T_{set} and the artificial thermal layer was fixed at 21 ^oC. The thermal conductivities for materials were λ_{Si}=1.3 W/(m·K), λ_{PMMA}=0.2 W/(m·K), λ_{UNCD}= 5 W/(m·K) and λ_{sir}=0.0278 W/(m·K). In this step, the distance between the artificial air layer and the PMMA surface, $d_{PMMA\text{-}Air}$, was varied and determined as 86.15 μm by matching the PMMA surface temperature with the experimentally measured value.

In second step, a UNCD probe was brought into contact with the PMMA surface. Thermal conduction was defined between the top surface of UNCD probe and artificial 21 ^oC layer, and between lower surface of UNCD probe and PMMA surface. The results of temperature distribution at T_{set}=80 ^oC are shown in Figure 5-1(b). For convenience of observation, the artificial air layer is not displayed. Close observation of the temperature variation in UNCD probe and PMMA surface are shown in Figure 5-1(c) and (d). The temperature in UNCD probe decreases quickly from the tip to the base of cantilevers due to the high conductivity of UNCD. The temperature distribution in PMMA is also influenced by the UNCD probe, but the range of variation is small. At the contact location, the temperature is calculated and shown in Table 5-1. Slight reductions are observed for all temperatures used. These values of $T_{PMMA\text{-}UNCD}$ are used for further analysis in the following section.

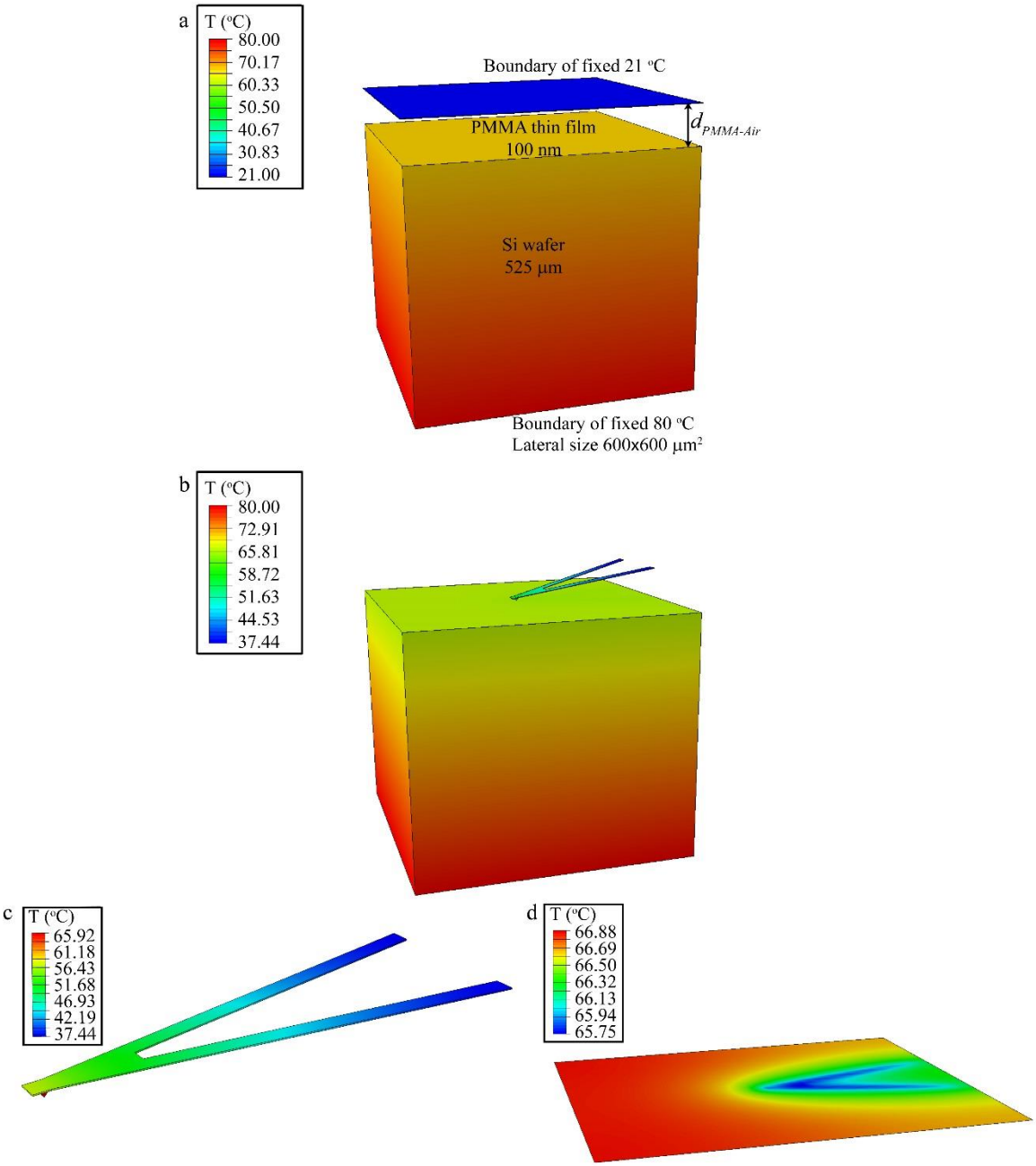

Figure 5-1. FEA temperature distribution results of (a) a model without UNCD probe and the distance between artificial thermal layer and PMMA surface, $d_{PMMA\text{-}Air}$, is determined by matching the surface temperature with experimentally measured values (step 1), (b) a model with UNCD probe in contact with PMMA surface (artificial thermal layer not display), and (c, d) close look at the temperature distribution in UNCD probe and PMMA surface in (b).

The methods for 3D characterizations of tip geometries and wear tests, described in Chapter 4, were used in the experiments here as well. Raster wear tests on PMMA structures were performed with temperature varying from 30, 50, 70 to 80 ^{o}C. At each temperature and each UNCD probe, the tests were repeated on three to six different patterns. The adhesion forces were measured and no significant difference was seen at different temperatures, as shown in Table 5-2. The PMMA pattern's volume was measured from AFM images using the exposed silicon wafer surface as a reference plane. Volume loss was then calculated by the difference of volume in a certain AFM image to that of the first image.

Table 5-2. List of adhesion forces between UNCD tips and PMMA surface measured at different set temperatures of heating stage.

T_{set} (^{o}C)	30	50	70	80
Tip R1	29.5±3.7	28.7±3.3	27.1±3.9	25.3±3.2
Tip R2	8.4±1.0	8.4±1.1	8.7±0.7	8.9±1.1
Tip R3	25.2±5.9	26.9±2.6	24.1±4.1	23.7±5.5

5.3 Experimental results

The PMMA volume loss as a function of sliding distance at four different temperatures is shown in Figure 5-2(a-c) for UNCD tip R1-R3. The error bars represent the standard deviation from multiple measurements. The data is reasonably well fit by a straight line and the slopes of these lines are the volume loss rates. The volume loss rates

increase with increasing temperature. This tendency is qualitatively consistent with the transition state theory. A significant change in volume loss rate is observed with varying temperature. At T_{set}=80 ^{o}C (65.9 ^{o}C at contact location), the volume loss rate is 76-87% larger than that at T_{set}=30 ^{o}C (27.8 ^{o}C at contact location) for all three tips.

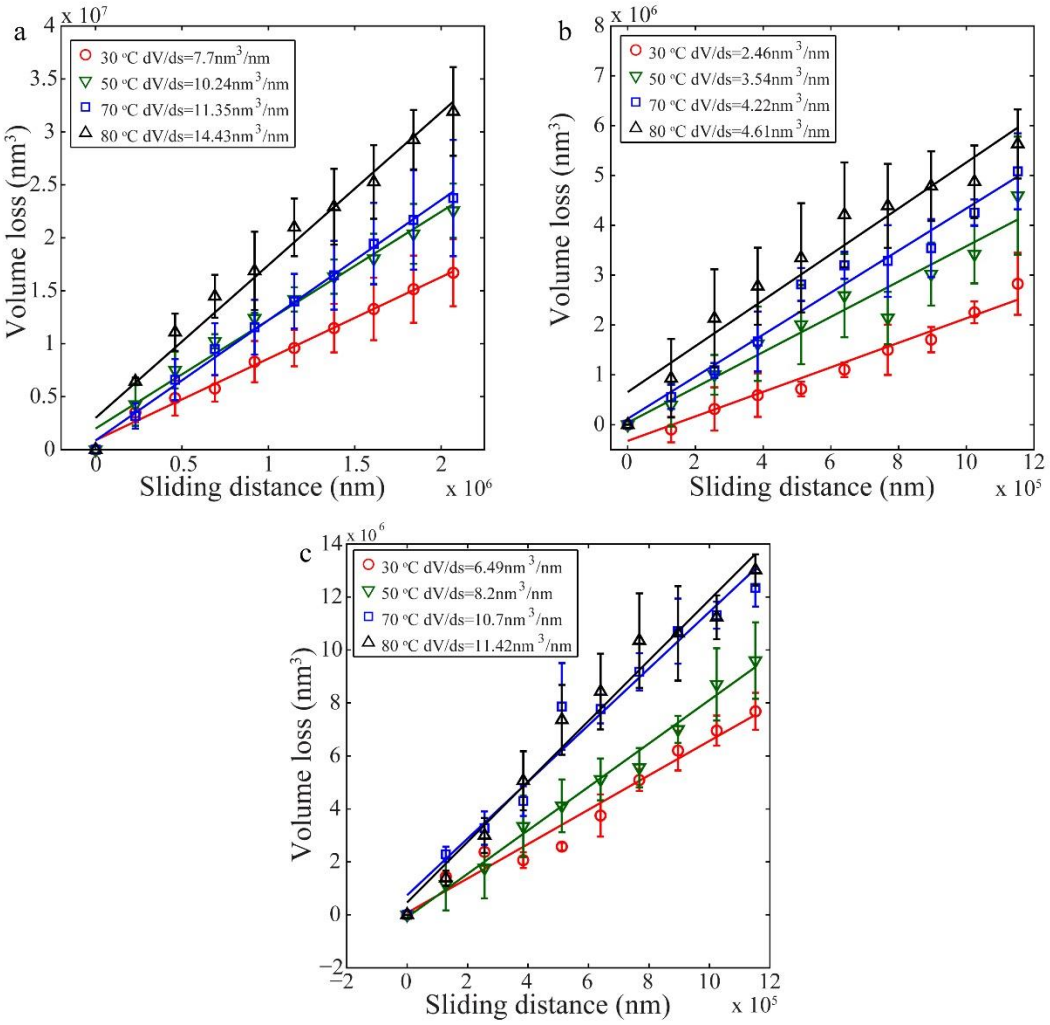

Figure 5-2. Volume loss as a function of sliding distance at varying set temperatures for (a) tip R1, (b) tip R2 and (c) tip R3.

The stress analysis was done by FEA as described in Chapter 4. In the FEA, the Young's modulus and yield stress used for PMMA are listed in Table 5-3. Previously measured wear parameters, E_a and V_{eff}, are listed in Table 4-2. Based on the stress distribution calculated at the interface, the transition state theory estimates the volume loss rate close to that from experimental measurements at ~300 K. At higher temperatures, however, both the average stress model (eq. (4.4)) and the stress distribution model (eq. (4.5)) overestimate the volume loss rate. In Figure 5-3, there are significant discrepancies between experimental measured volume loss rate by tip R1 and the ranges estimated by transition state theory. At ~340 K, transition state theory overestimates the volume loss rate by almost an order of magnitude. For tip R2 and R3, transition state theory models result in 5 to 10 times larger volume loss rate compared with experimental data as well. These results suggest that the temperature dependence in the transition state theory model presented in Chapter 4 does not describe the wear of PMMA at varying temperatures.

Table 5-3. Young's modulus, Poisson's ratio and yield stress used in FEA for PMMA at different temperatures [86], [87].

T (K)	E (GPa)	ν	Yield stress (MPa)
300.8	3.04	0.4	184.4
316.1	2.53	0.4	144.6
331.3	2.09	0.4	113.9
338.9	1.94	0.4	102.8

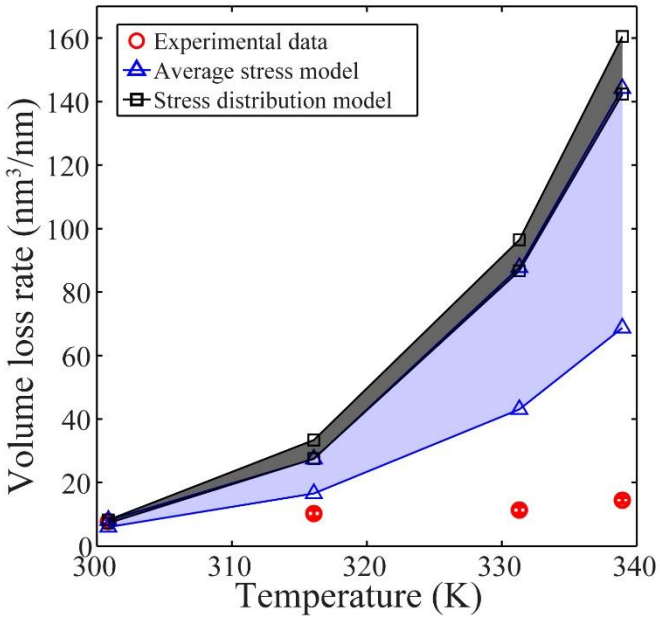

Figure 5-3. Experimental results of volume loss rate for tip R1 compared with transition state theory average stress model (eq. (4.4)) and stress distribution model (eq. (4.5)).

5.4 Analysis and discussion

5.4.1 Temperature dependent tribological properties

In transition state theory, the wear process is represented as a thermally activated process with the system transferring from a local potential energy minimum to another when an atom is worn [40], [44], [77]. Eq. (4.4) and (4.5) indicate a temperature dependence of the bonding and debonding process of an atom. Unlike many other solids, such as ionic bonded NaCl and covalent bonded C- or Si-based materials, temperature effects the properties of polymers through multiple mechanisms, including chain mobility [90], [91] and viscoelastic relaxations [88], [89]. These properties can have significant

effect on polymers' tribological behaviors. For example, Barry et al. [91] used molecular dynamics to simulate the sliding and wear between two polytetrafluoroethylene (PTFE) slabs. Chain scission and carbon atoms separated from backbones, which indicated covalent bond breaking and supported atom-by-atom attrition, as well as chain segments bowing, entanglement and reorientation, which depended on polymer's mobility, were observed at the interface. This indicated a wear process that combined both atom-by-atom attrition and polymer chain movements. Hammerschmidt et al. [88] used friction force microscopy and measured varying friction behavior of PMMA at varying temperature below T_g. By applying time-temperature superposition, the friction data collapsed into a master curve at reference temperature 60 ^oC. The dependence of friction on temperature was attributed to hindered rotation of ester group in PMMA (β-relaxations) that occurs under T_g. However, temperature dependent properties such as these are not considered in the original transition state theory models for wear of polymers.

5.4.2 Modified transition state theory models

In polymer physics, the time-temperature superposition principle [88], [92]–[94] is widely used to determine temperature-dependent mechanical properties from known properties at a reference temperature. Here, modified transition state theory wear models are proposed based on application of this principle. A schematic is illustrated in Figure 5-4. Volume loss rates at different temperatures are shown as separate segments in left panel.

A shift factor $\alpha_T=\alpha_T(T)$ is used to shift four segments into one master curve at reference temperature. The form of shift factor [88], [93] is defined as:

$$\ln \alpha_T = \frac{E_r}{R} exp\left(\frac{1}{T} - \frac{1}{T_0}\right) \tag{5.1}$$

where R=8.314 $JK^{-1}mol^{-1}$ is the universal gas constant, T_0 is the reference temperature, E_r is an activation energy related to viscoelastic relaxations of PMMA. Since the temperatures in AFM wear experiments are below T_g, β-relaxation and the energy E_r close to the energy hindered rotation of the side chains (-$COOCH_3$) in PMMA [88] are expected.

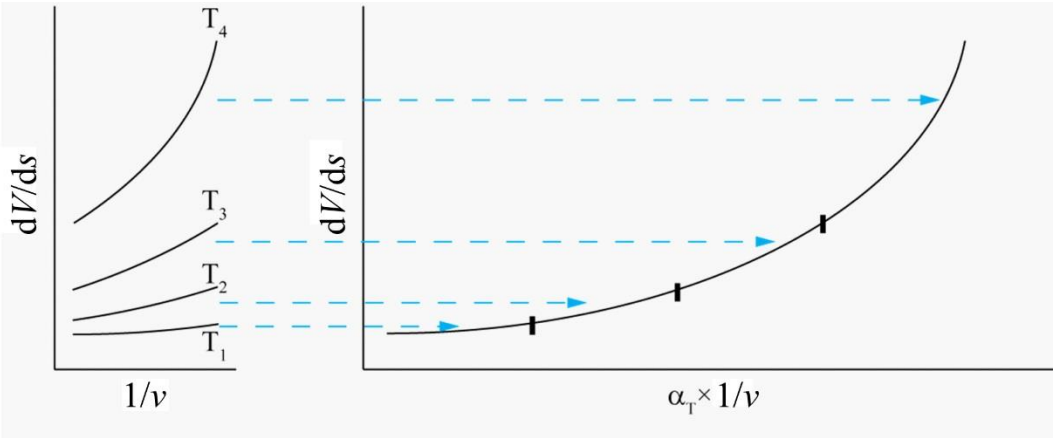

Figure 5-4. A schematic of applying time-temperature superposition on PMMA nanoscale wear mechanism. dV/ds is the volume loss rate, v is the sliding speed, and $\alpha_T=\alpha_T(T)$ is the shift factor as a function of temperature.

Combining the shift factor and transition state theory models, I propose the modified average stress model to describe wear:

$$\frac{\partial V}{\partial s} = \alpha_T \frac{A_c b f_0}{v} exp\left(\frac{-E_a + V_{eff}\bar{\sigma}}{k_B T_0}\right) \tag{5.2}$$

and the modified stress distribution model:

$$\frac{\partial V}{\partial s} = \alpha_T \frac{A_c b f_0}{v} exp\left(\frac{-E_a}{k_B T_0}\right) g(V_{eff}, \sigma) \quad (5.3)$$

where T_0 is selected as 300 K. All parameters, except α_T, in both models remain as the same as those in previous chapter. When $T=T_0$, $\alpha_T(T_0)=1$ and eq. (5.2) and (5.3) reduce to eq. (4.4) and (4.5), respectively, and both models provide good estimates of PMMA wear as shown in Chapter 4.4.

By using experimentally measured volume loss rate and FEA calculated stress and contact area for all three tips used in experiments, the shift factor as a function of temperature is shown in Figure 5-5. The fits by eq. (5.1) for average stress model and stress distribution model are plotted as well.

The fittings result in E_r=9.59 kcal/mol for modified average stress model (eq. (5.2)) and E_r=11.74 kcal/mol for modified stress distribution model (eq. (5.3)). These values are close to the value ~12 kcal/mol, which is measured for the activation energy for hindered rotation of the $–COOCH_3$, i.e. β-relaxation, in PMMA [88]. This implies that the shift factor introduced into the original transition state theory models considers the temperature dependence of viscoelastic relaxation of PMMA.

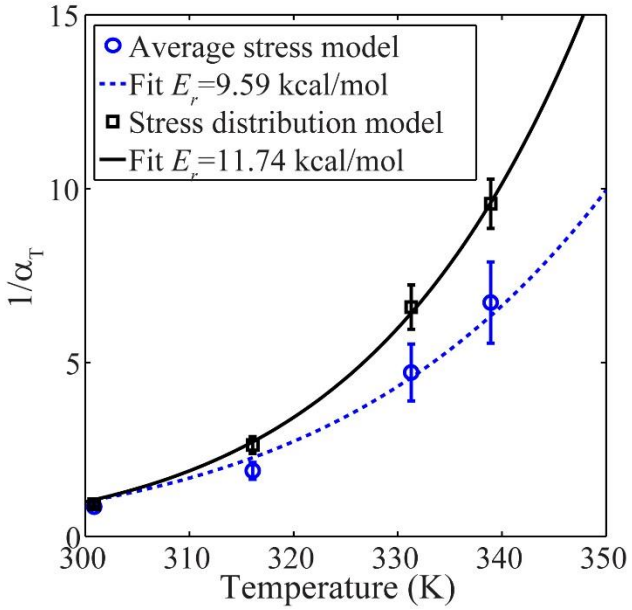

Figure 5-5. Shift factor as a function of temperature for average stress model and stress distribution model.

The ranges of volume loss rate estimated by modified transition state wear models at varying temperatures, together with experimental data, are shown in Figure 5-6. Compared with original transition state models (Figure 5-2(d)), the modified models match the experimental data much better. For modified average stress model, the estimated ranges (light blue regions in Figure 5-6) becomes larger with increasing temperature. The average deviation of the estimated range to experimental data increases from 18.6% (300.8 K) to 37.5% (338.9 K). The modified stress distribution model has generally stable volume loss rate ranges (light black regions in Figure 5-6) at different temperature and the estimations are much precise than that of modified average stress model. The deviation of estimation is only 13.1% to 19.4% compared with experimental data. The deviation may be caused by

several possible factors, including different mechanical properties of PMMA near free surface [95] and dependence of E_r on stress [89]. Further detailed studies need to be done in the future to fully validate this model.

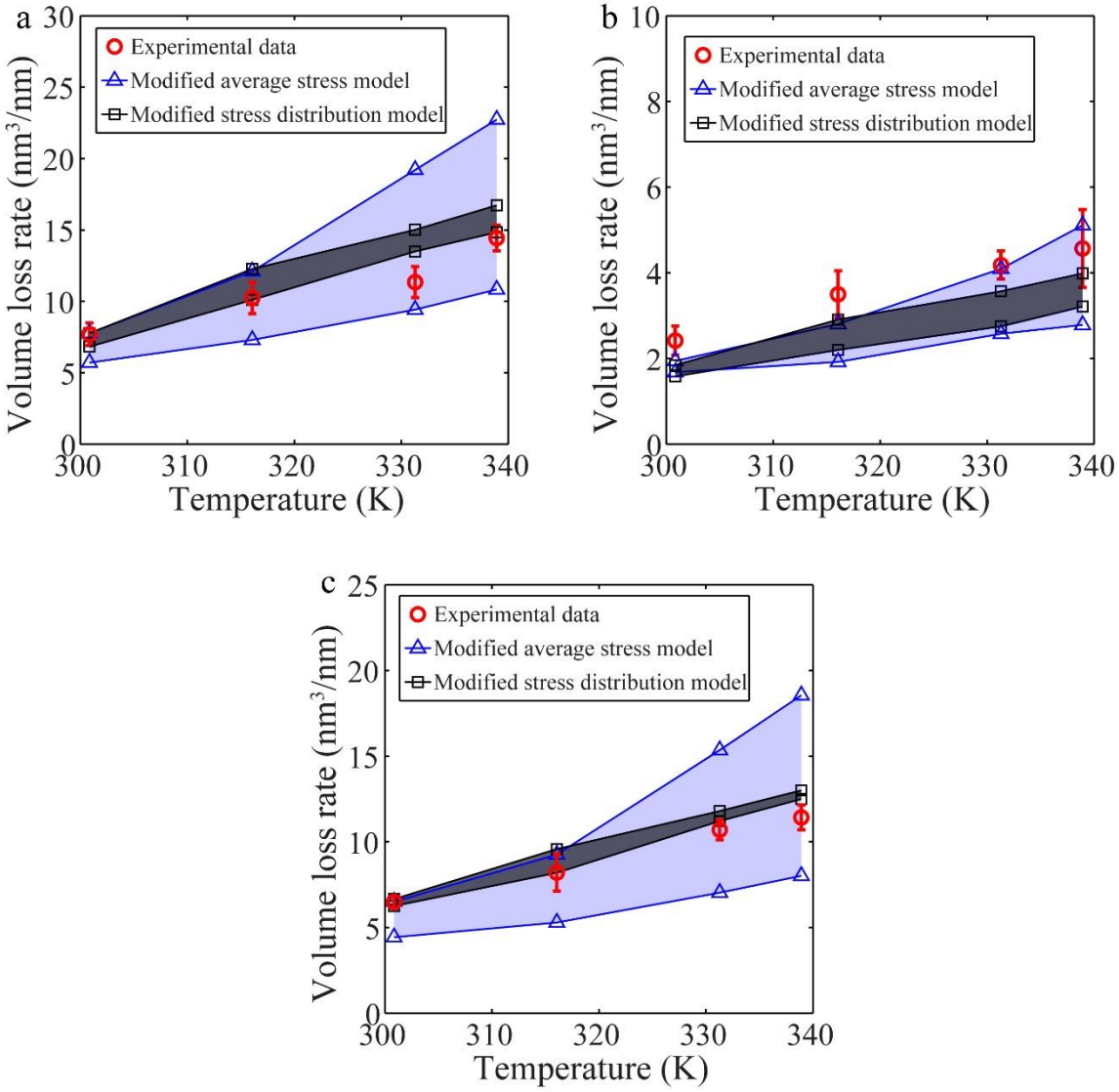

Figure 5-6. The experimentally measured volume loss rate of nanoscale PMMA wear at varying temperatures by AFM tip (a) R1, (b) R2, and (c) R3, compared with the ranges of volume loss rate estimated by modified average stress model (eq. (5.2)) and modified stress distribution model (eq. (5.3)).

5.5 Summary

AFM-based nanoscale wear tests between UNCD tips and PMMA thin films were performed at varying temperatures in a dry nitrogen environment. The samples were patterned by e-beam lithography and heated during testing. The temperature at the contact location was simulated by FEA to account for the thermal conductivity of the AFM probe.

The experiments were done at temperatures between 300.8 K and 338.9 K, which were lower than T_g of PMMA 380 K. The volume loss rate increased with increasing temperature. The transition state theory model presented in Chapter 4 overestimates the volume loss rate by more than a factor of 10 at elevated temperatures.

Modified transition state theory wear models that include thermally activated atom-by-atom attrition process, as well as temperature dependent viscoelastic relaxation of PMMA, are proposed. A shift factor was applied in the proposed models and an activation energy of ester group rotation E_r=9.59 kcal/mol and 11.74 kcal/mol in average stress and stress distribution model, respectively. The modified models (eq. (5.2) and (5.3)) reasonably described the experimental data for all temperatures. The modified stress distribution model resulted in more accurate estimates with deviations of 13.1% to 19.4% from experimental data at different temperatures.

CHAPTER 6: Microscale wear tests by nanoindenter

6.1 Introduction

At the macroscale, wear is typically described empirically since there are complicated interactions between multiple asperities at large length scales and wear usually involves fracture and plastic deformation [44]. In nanoscale wear experiments, the contact situation is simplified and a more rigorous analysis can be done. The nanoscale wear experiments have led to atomic attrition model of wear [42], [44], [61], [66], [77], which describe atom removal using a stress-assisted transition state theory. In the previous chapters, the AFM-based wear experiments on PMMA samples demonstrate that this wear mechanism can be applied to polymers at the nanoscale. To broaden the understanding and evaluate the application of the transition state theory at larger scales, wear experiments at larger scales are necessary. In this chapter, I present wear experiments in which the contact size is 100 to 4000 times larger than AFM-based experiments in previous chapters.

Nanoindentation has been widely used for mechanical characterization at the small scales, such as indentation for hardness and elastic modulus [96], scratch tests for adhesion [97], friction [98], [99], fracture toughness [100] and scratch resistance [30], [101], [102] measurements. During a scratch test, an indenter scratches on top of a sample in one single pass and leaves a permanent track. A high load is usually applied in a scratch test and the process, especially when a sharp indenter (such as Berkovich tip) is used, involves a large amount of plastic deformation, complicated stress fields, and sometimes fracture and crack

propagation [30], [101]. The complex mechanical situation and large deformation in a typical scratch test makes it poorly suited for studying wear phenomenon, which is a gradual and repeated process. However, to scan a blunt indenter, for example a spherical end indenter rather than Berkovich indenter, repeatedly over the same pass using moderate load can be used for wear studies without inducing complicated stress fields and damage.

In this chapter, nanoindenter based line wear tests on PMMA with micrometer sized contact (radius 0.16 to 0.3 μm) were performed. Wear tracks were generated by repeated scratching a diamond tip over the sample. An indenter with spherical end (radius ~1 μm) was used and the loads were systematically varied. The profiles of the wear tracks were measured by high resolution AFM imaging. Volume loss was found to increase sublinearly with sliding distance under constant loads. The loads and contact areas were more than two orders of magnitude larger than that in previous AFM based nanoscale wear tests. The wear volume increased exponentially with normal contact stress and the relationship was described by transition state theory model, even though the scale is considerably larger than the AFM-based tests.

6.2 Experimental methods

The microscale wear tests were performed by a spherical diamond indenter (radius ~1 μm as shown in Figure 6-1) in a Hysitron TI-950® triboindenter at room temperature. The indenter was first scanned along a straight line (-8 to +8 μm of a selected location)

under load control of a low load (<2 μN) in order to measure the tilt of the sample and original profile before wear. Then the indenter was moved to location of +6 μm and the load was ramped to a higher value (20 to 200 μN) in 5 s. The indenter was slid from +6 μm back to -6 μm under this high constant load. Then the indenter was unloaded back to the low load and moved to -8 μm. The low load sliding between +6 and +8 μm, and -6 and -8 μm measured the non-worn surface height. These steps were repeated five times with constant sliding speed of 3 μm/s. The loads varied from 20 to 200 μN with a uniform increment of 20 μN. For each load, the tests were repeated at 10 different locations. To exclude the influence of possible asymmetry of indenter, the indenter was unmounted, rotated a random angle and mounted back again to the transducer manually. Then, some tests of ten times wear with high load scanning were performed under load of 160, 180 and 200 μN. The loads applied in these microscale tests were as 100 to 4000 times as larger than those applied in nanoscale line wear tests in Chapter 4.

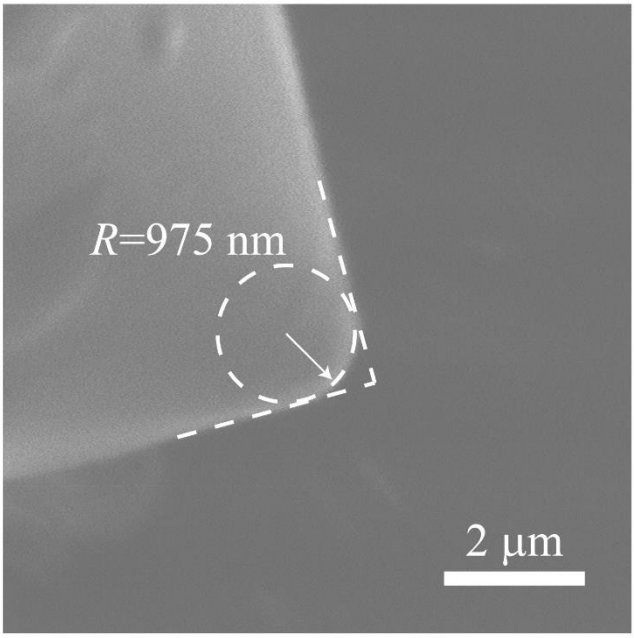

Figure 6-1. SEM image of the spherical end of the conical diamond indenter.

During the tests, the normal load F_z was controlled and the lateral force F_x, the on-load depth and depth after elastic recovery were measured. As indicated in Figure 6-2, the recovered depth is *d(0)* and on-load depth is $d_s(0)$. Considering that the diamond has much higher stiffness than that of PMMA, the deformation of the indenter is much smaller than that of PMMA. Thus, the on-load wear track profile (the green dashed line) can be determined from the indenter's geometry and $d_s(0)$. However, the wear track after elastic recovery (solid line) cannot be determined from a single value of *d(0)*. In order to calculate the volume variation, the profile of the cross section needs to be determined.

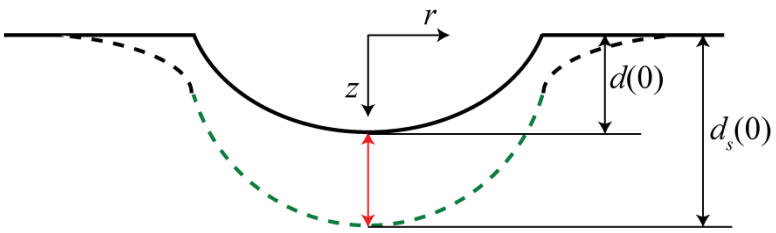

Figure 6-2. A schematic of the cross section of a wear track on load (dashed line) and the wear tack after elastic recovery (solid line). Depth is $d(0)$ and on-load depth is $d_s(0)$.

High resolution AFM images of the wear tracks after final scans were taken using a sharp silicon AFM tip (NanoSensors^{TM} PPP-NCH AFM probe) in Bruker Icon$^{®}$ AFM. Tapping mode AFM images of 20×20 μm^2 with 512×512 resolution were acquired over wear tracks. The cross sections of the wear tracks were measured from AFM images.

6.3 Experimental results

6.3.1 Nanoindenter wear results

The depth and on-load depth of the wear tracks were leveled based on the measured original sample profile before wear tests. As shown in Figure 6-3(a), the depth of the wear track increased strongly for first wear, then kept increasing gradually. The depth and on-load depth were calculated using the data within lateral displacement between -4.5 and +4.5 μm (two red lines in Figure 6-3(a)). Under different loads, the depth and on-load depth of 5 wear scans are shown in Figure 6-3(b) and (c). At 20 μN, the on-load depth remained around 11 nm for all 5 scans and no observable depth after elastic recovery. For other loads,

higher loads resulted in larger on-load depth and it increased sublinearly with scan numbers. After elastic recovery, non-zero depth was measured and a similar sublinear trend was observed for all loads (40 to 200 μN). In Figure 6-3(d), the depth showed a linear dependence on the on-load depth. The relationship was well described by a linear relationship: d=0.81d_s-11.74 nm, for all data except those at 20 μN, where no wear was observed.

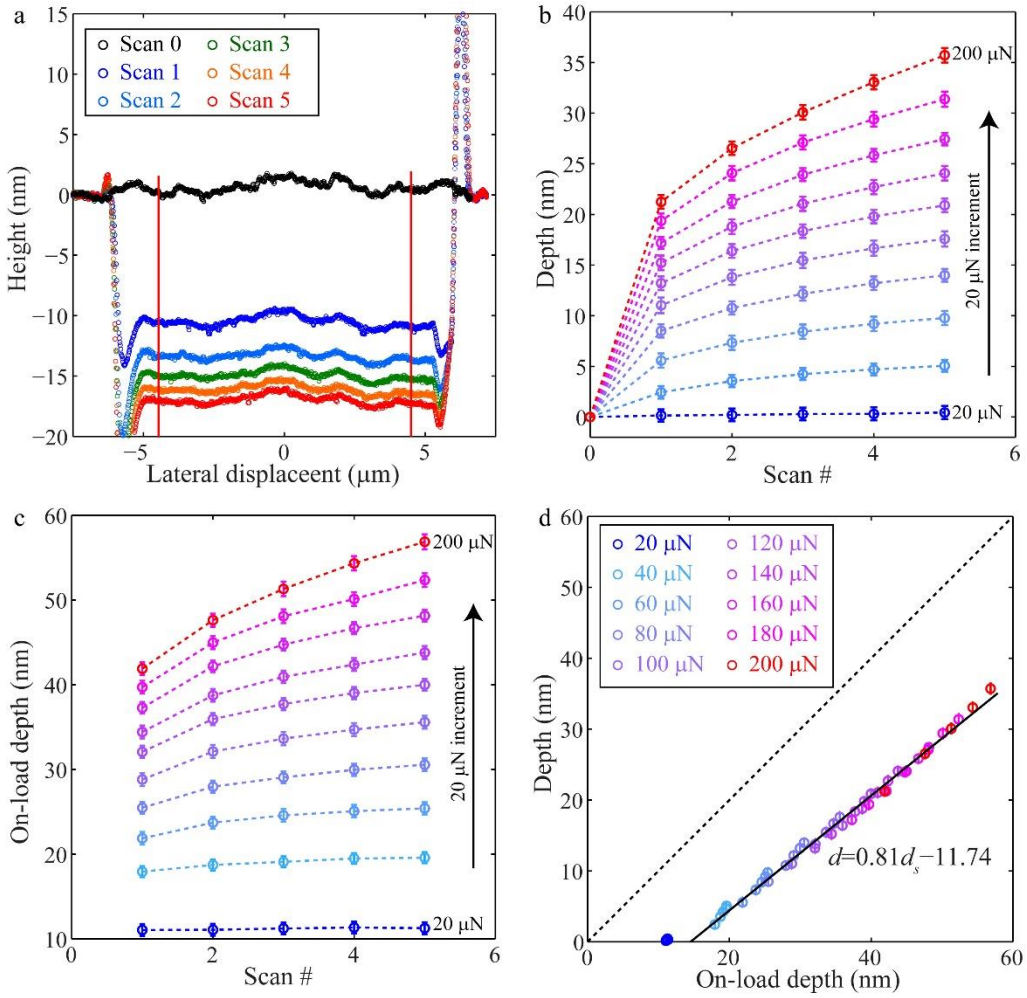

Figure 6-3. (a) Height variation along the wear track (after elastic recovery) of repeated scans under normal load of 100 μN, (b) depth and (c) on-load depth as a function of scans and under different loads, and (d) the relationship between depth and on-load depth.

6.3.2 Wear tracks characterized by AFM

High resolution AFM images of the wear tracks after wear tests were taken. An example of wear track after sliding under a load of 120 μN wear is shown in Figure 6-4(a). The cross section along the tracks were consistent as indicated by 10 randomly selected paths in Figure 6-4(b) and showed small variations along the wear tracks. However, the wear track cross section profiles couldn't be measured in this way for other scans (except the last scan). In order to determine the cross section profile of the wear track after elastic recovery for all scans, an assumption that the elastic recovery mainly happened in the vertical direction was used. With this assumption, the cross section profile can be estimated from the on-load wear track profile and the on-load depth, i.e.

$$d(r) = 0.81\left(d_s(0) - R_{ind} + \sqrt{R_{ind}^2 - r^2}\right) - 11.74\,nm \qquad (6.1)$$

where R_{ind} is the radius of the indenter. Therefore, the profile of the cross section of wear track after elastic recovery can be estimated by knowing the on-load depth of this scan.

This assumption was validated by fitting all AFM measured wear track profiles for every loads with corresponding on-load depth and eq. (6.1). The fitting results had very small average rms error (~1 nm) for all loads. Thus, the cross section profile and the volume of the wear tracks were determined by integrating the area of cross section along the wear track. The volume of the wear tracks were shown in Figure 6-5 for loads of 40 to 200 μN. As the volumes were calculated based on a 9 μm wear track (from -4.5 μm to 4.5 μm as

indicated in Figure 6-3(a)), each scan corresponds to a sliding distance of 9 μm. For the ten scan experiments, the method of nanoindenter-based wear tests, AFM characterization of wear tracks, and the data process were performed in the same way.

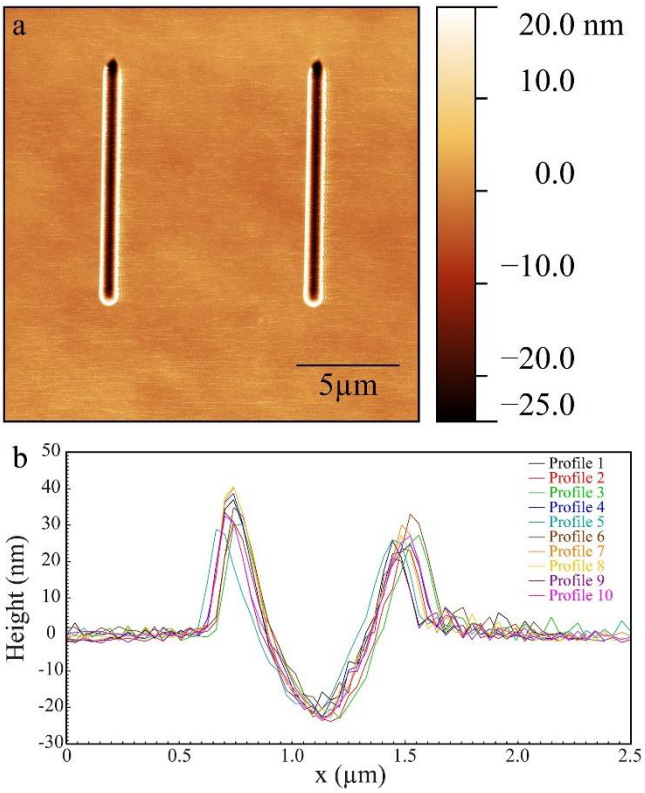

Figure 6-4. (a) AFM image of wear tracks after 5 scans under 120 μN load and (b) the cross section profiles of 10 paths randomly distributed along the length.

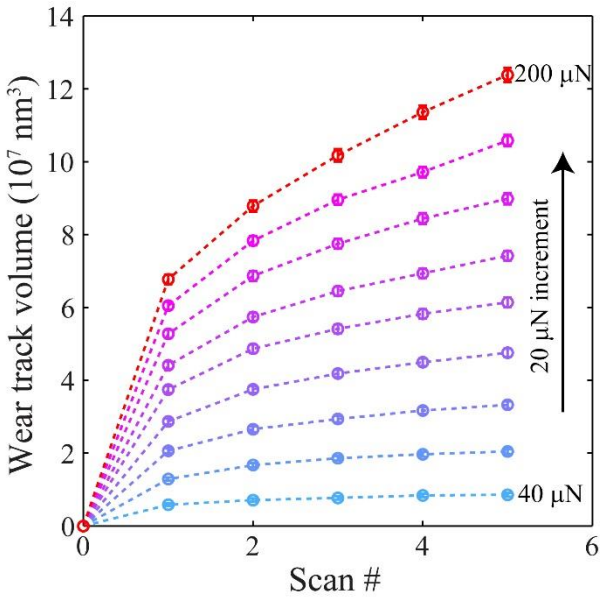

Figure 6-5. The volume of the wear tracks at different loads as a function of scan numbers. Each scan is corresponding to a sliding distance of 9 μm.

6.4 Analysis and discussion

6.4.1 Stress analysis

To analyze if the volume loss is described by transition state theory, the stress at contact interface is needed. The average contact stress was estimated by a contact mechanics model developed for spherical tip scratch tests [103]. In this model, contact is assumed to occur between the front half of the indenter and the substrate. The normal stress and shear stress at the interface are related to the forces in vertical and lateral direction via a geometric analysis. The model is formulated as [103]:

$$F_x = p_m R_{ind}^2(\alpha - \sin\alpha\cos\alpha) + 2sR_{ind}^2\left[\int_0^{\pi/2}\int_0^{\alpha}\sin\zeta\sqrt{sin^2\xi + cos^2\xi cos^2\zeta}\,d\zeta d\xi\right] \quad (6.2)$$

$$F_z = \pi/2 p_m R_{ind}^2 sin^2\alpha - sR_{ind}^2[\sin\alpha - cos^2\alpha\, ln(\sec\alpha + \tan\alpha)] \quad (6.3)$$

where F_x is the lateral force and F_z is the normal load, α is the contact angle and is determined by indenter's geometry and contact depth:

$$\alpha = \arcsin\left(\frac{\sqrt{2R_{ind}d_c - d_c^2}}{R_{ind}}\right) \quad (6.4)$$

where d_c is the contact depth and calculated as $d_c=(1-\varepsilon/2)d_s+\varepsilon d/2$ and ε=0.75 for spherical indenter [96]. The average normal stress p_m and the average shear stress s are to be solved from eq. (6.2) to eq. (6.4). The contact area in the tests ranges from 4×10^4 nm^2 to 1.5×10^5 nm^2, which is 2 to 3 orders of magnitude larger than that in AFM based wear experiments reported in previous chapters.

6.4.2 Transition state theory on microscale wear

The volume loss due to wear were calculated based on the volume of wear track as shown in Figure 6-5. The first scan resulted in much larger volume change compared with following scans. This first scan included both plastic deformation and material removal due to wear. In the following scans, as the high load applied was the same as that in first scan, much less plastic deformation was induced in these scans. Thus, to analyze the volume loss due to wear, the first scan data was excluded. For each individual load, a sublinear relationship between wear volume and sliding distance was observed Figure 6-5,

which suggests that Archard's wear law (eq. (2.17)) cannot be used to describe the experimental measurements.

The transition state theory model (eq. (4.4)) was applied to the experimental data from the 5 scans tests (load 40-200 μN) and 10 scans tests (load 160-200 μN). The results from both 5 and 10 scan tests are similar as shown in Figure 6-6. If each data set is fit separately, no significant difference is observed. A fitting to all data results in E_a=0.81 eV and V_{eff}=14.4 Å^3.

Despite the fact that the contact conditions in microscale wear tests, including load and contact area, are significantly larger than those in AFM based nanoscale tests, the transition state theory describes the wear properties PMMA as a function of normal contact stress. The effective activation volume is comparable with that measured in nanoscale line wear tests. The activation energy, however, is larger than that measured in nanoscale tests (E_a=0.67-0.73 eV). The larger E_a in microscale experiments indicates that the PMMA has a higher apparent wear resistance in the microscale tests than the nanoscale tests. Two possible reasons for this result: a) plastic deformation and strain hardening in PMMA during the first cycle of microscale wear tests and b) the different surface chemical reaction of diamond indenter, which is single crystal, compared to the UNCD AFM tip, which has different orientation grains and grain boundaries, in contact with PMMA. As the atom-by-atom attrition process involves bonding and debonding of atoms at interface [40], [44], the chemical properties at surface can contribute in wear resistance. Further investigation on these hypotheses will be done in the future.

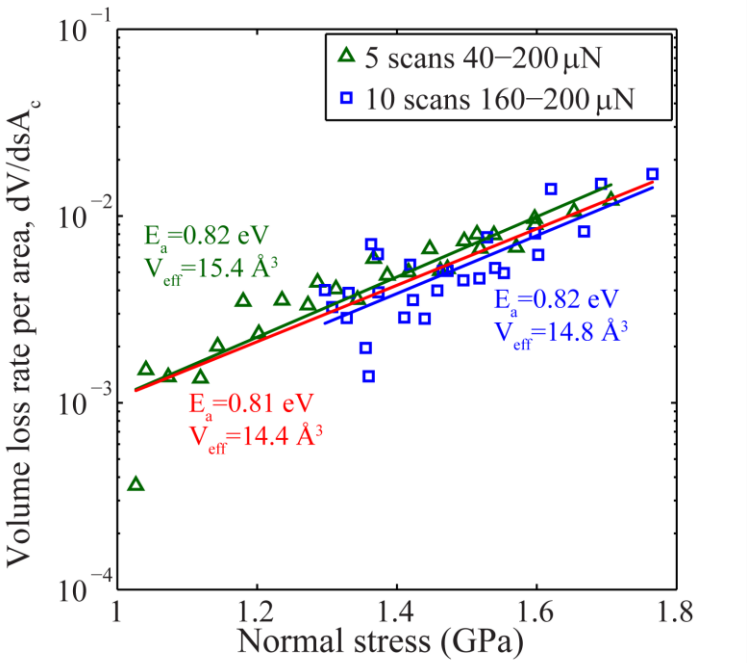

Figure 6-6. The application of transition state theory to microscale wear experimental data. The green and blue lines are fits to 5 scans and 10 scans experiments separately, and the red line is the fit to all data points.

6.5 Summary

Microscale line wear experiments were performed in a nanoindentation system with a 1 μm spherical diamond indenter under load control (20-200 μN). The wear tracks were characterized by high resolution AFM imaging. Unlike Archard's wear law, which is frequently used at macroscale, the microscale wear results show a sublinear relationship between wear volume and sliding distance at each constant load. Despite significant differences between the nanoindenter-based microscale tests and AFM based nanoscale tests, i.e. both load and contact area are 2 to 3 orders of magnitude larger in microscale

tests, the dependence of wear volume on normal contact stress is appropriately described by transition state theory model (eq. (4.4)). This is the first application of transition state theory at a larger scale and the results imply that the nature of atom-by-atom attrition process occurs over the range of nanoscale to microscale wear tests.

CHAPTER 7: Finite element simulations of wear

7.1 Introduction

During the sliding of an AFM tip against a flat surface, the geometry of tip and the topography of the substrate evolve, and the adhesion force as well as the contact stress distribution at the interface change. The evolution of mechanical interactions coupled with geometries make it difficult to understand the relationship between applied loads, stress and wear measurements in experiments. FEA simulations allow the stress distributions to be calculated and, at the same time, predict how the geometries of contacting bodies evolve. Specifically, simulations can be used in an iterative fashion to predict the evolution due to wear between various components. The motivation of the work in this chapter is to establish an FE wear model to study the contact details during wear and investigate the wear behavior under various situations.

FEA has been used in simulating macroscopic wear and to predict the life-span of mechanical components in applications such as dry sliding wear [104], fretting [105]–[107], and fatigue of solid lubricant [108]. FEA simulations of wear processes usually require several steps: (1) experimentally measure the wear behavior of the sample and determine wear parameters in wear laws that describe material removal [108], [109], (2) construct FE models matching the pre-wear geometries of contacting components and boundary conditions matching the contact and sliding conditions in experiments, (3) apply a wear law to calculate volume and height variations based on FEA force and stress results

for an increment of sliding distance and update components' geometries, (4) iteratively repeat the previous step until the sliding distance reaches the desired value. The quantities, such as volume loss and height loss due to wear, can be predicted as a function of sliding distance and applied load using these simulations.

The evolution of components' geometries and application of wear criteria is usually simulated in FE in one of two ways: a) use of an adaptive mesh or user defined subroutine for mesh modification during contact simulation [105], [106], [110], and b) use of iterative post-FE processing to calculate volume/height loss according to wear mechanism, adjust the mesh for a new model geometry and then run contact simulation again [104], [107], [108]. The post-FE processing is less time consuming in general [104]. The iteration algorithm, remeshing scheme and contacting conditions are of critical importance to the computational stability, efficiency and accuracy.

In this Chapter, an iterative FE-based wear simulation algorithm is established and used to examine nanoscale wear of PMMA and DLC. A transition state theory stress distribution model is applied as the criteria in the wear simulations. Case studies, including effect of contacting pairs with different modulus, friction and roughness, are performed, followed by a 3D simulation of line wear test on PMMA surface. Comparable wear behaviors are seen in numerical simulation and previous experimental results. The results from numerical simulations indicate correlations between averages contact stress and volume loss rate if there's no roughness at interface and show a strong dependence of wear volume on surface roughness.

7.2 Simulation method

Wear simulations between an AFM tip and a sample are performed using an iterative FEA simulation process implemented in Matlab®-Abaqus®. A transition state theory stress distribution wear model (eq. (4.2)) is used. A flow chart that summarizes this iterative process is shown in Figure 7-1.

To construct the initial geometries of the AFM tip and the sample, an Abaqus contact model between two rectangular cubes with the mesh, contact constraints and boundary conditions fully defined is firstly written into an Abaqus input file. Then, a Matlab program is used to read and modify the nodal coordinates to generate the initial tip and sample geometries for corresponding parts. The loading conditions or boundary conditions can be revised if necessary in this step. After modification, a new Abaqus input file is written. The stress distribution is then calculated by running this modified input file. Unless specified otherwise, the lateral dimension of the model is 150 nm and the vertical dimension is 75 nm for both tip and substrate. The load is applied on the base of tip and then the substrate is slid forward and backward repeatedly along a 50 nm track.

The height loss rate for each contacting node is estimated by transition state theory:

$$\left(\frac{\partial h}{\partial s}\right)_k = \frac{b f_0}{v} exp\left(\frac{-E_a + V_{eff}\sigma_k}{k_B T}\right) \tag{7.1}$$

where k=1,2,3…N, with N being the total number of nodes in contact. To determine the height loss, the sliding distance, s_i, for this step is needed. The determination of sliding distance is crucial. If the sliding distance is too long, the local high stress will result in an unrealistic deep valley or roughness at interface and thus causes extremely high stress or divergence, which leads to failure of whole program, for next step. If the sliding distance is too short, the program will take an unnecessarily long time to finish.

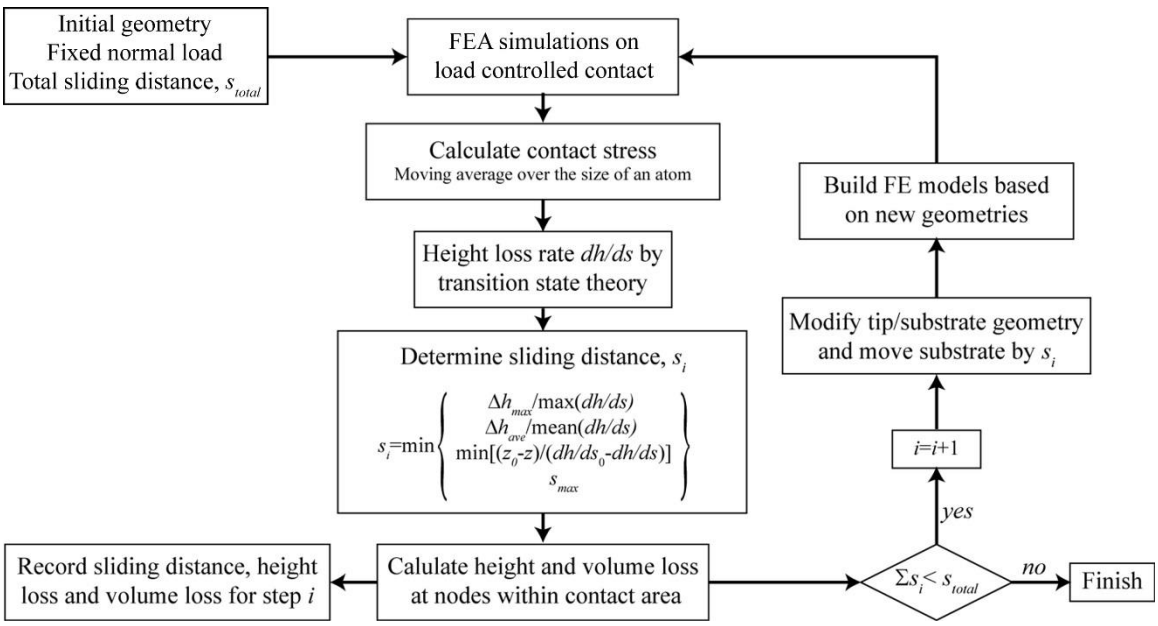

Figure 7-1. Flow chart of FE simulation process with application of transition state wear model to describe local material removal.

As indicated at the center box of Figure 7-1, there are four criteria for determining sliding distance. The sliding distance is determined as the minimum of (a) the height loss at the node with the largest contact stress is less than a preset Δh_{max}, (b) the average height loss of the nodes in contact is less than a preset Δh_{ave}, (c) the height loss differences of the

lowest node relative to other nodes is less than the original differences of vertical coordinates, and (d) less than a preset s_{max}. The constraint values for the 3D models are selected as Δh_{max}=0.5 nm, Δh_{ave}=0.2 nm, and s_{max}=3 nm. These were determined by trial and error of simulations. Since 2D simulation can run much faster in a single step compared to 3D, smaller constraints Δh_{max}=0.1 nm, Δh_{ave}=0.05 nm, and s_{max}=0.5 nm are used in order to have smaller sliding distance in each step and capture more details during the total wear simulation.

Once the sliding distance is determined, the height variation for each node in contact and volume loss of both tip and sample can be calculated and output. If the total sliding distance hasn't reached the desired value, new tip and sample geometries are modified accordingly and the model is run again. A Matlab program is coded to build a new FEA model with these updated geometries by reading and revising coordinates in the Abaqus input file. The modified model goes back to the loop for stress and height loss calculation. If the total sliding distance reaches the value that is specified for the simulation, the program stops.

7.3 2D wear simulations and case studies

In the 2D wear simulations, plane strain is assumed. The basic model assumes frictionless contact model between a paraboloidal tip and a flat smooth substrate. The cases studied in this section include: (1) different materials in contact, three tip-substrate pairs DLC-PMMA, DLC-UNCD and DLC-DLC are studied, (2) different friction coefficients,

and (3) effect of surface roughness with different spatial distributions and amplitudes (rms roughness 0.1 to 0.62 nm).

7.3.1 Contacting pairs

The tip has a paraboloidal profile with radius of 20 nm and the applied load is 30 nN/nm. The material properties and wear parameters are listed in Table 7-1. In DLC tip on PMMA sample and DLC tip on UNCD sample cases, the sliding distance is 100 nm (1 cycle of 50 nm sliding forward and backward), and in DLC tip on DLC sample case, a total sliding distance is 300 nm.

Table 7-1. The mechanical properties and wear parameters [77], [87] used in FE wear simulations.

Material	E (GPa)	ν	E_a (eV)	V_{eff} (Å^3)
PMMA	3.04	0.4	0.67	11.3
DLC	150	0.3	0.8	5.5
UNCD	790	0.057	Assume no wear	

Contact stress distributions were calculated as the tip geometry changes during sliding. As shown in Figure 7-2(a-c), the normal stress distributions in DLC-DLC contact varied at different sliding distances. At 0 nm, the tip was a smooth paraboloid and substrate was a flat surface and this results in a symmetric stress distribution. The substrate was displaced to the left and this resulted in asymmetric wear of tip. Geometries of tip (Figure

7-2(d)) and substrate changed due to the wear. Large volume loss initially occurs on the front side of the tip. This is because the wear happens in both tip and substrate and caused an asymmetric and rough contact interface, for example, the tip profile after 10 nm sliding distance (Figure 7-2(d)). The stress distribution changed corresponding to the geometries. Locally high stresses happened at the rough interface and caused faster wear rate at these locations. Thus, the geometry, as that after 100 nm sliding in Figure 7-2(d), became relatively symmetric and smooth again. These process repeated over the course of the full sliding experiment and gradually removed the material. The tip geometry was generally a flat end with curved edges, rather than a tip truncated by a plane, after the initial stage of rapid change in geometry.

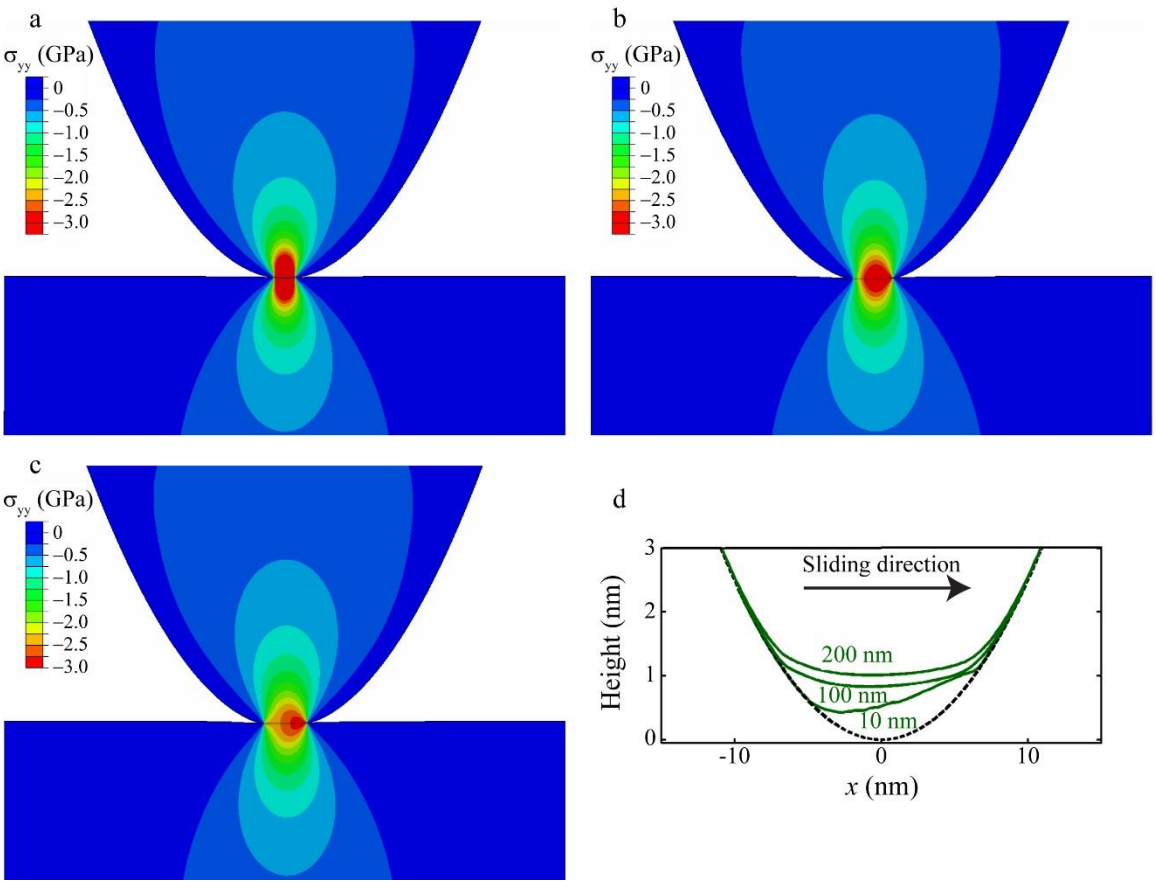

Figure 7-2. Stress distribution in DLC tip and DLC substrate at sliding distance of (a) 0 nm, (b) 100 nm and (c) 200 nm. The substrate is moving to left at these moments. (d) The evolution of DLC tip geometries during sliding.

The volume loss and average stress as a function of sliding distance for three pairs of materials are shown in Figure 7-3. The DLC-DLC case showed a rapid volume loss at the initial stage and then the volume loss became more gradual (Figure 7-3(a)). The average stress within the first 25 nm fluctuated significantly and resulted in an increased volume loss. In the DLC-PMMA contact, the DLC tip had a much smaller volume loss compared with that of PMMA over the 100 nm sliding. The PMMA substrate had >500× as larger volume loss than the DLC and the volume loss of PMMA increased linearly with sliding

distance and the average stress remained almost constant (Figure 7-3(b)). The DLC tip volume loss when slid against UNCD had a smooth sublinear relationship with sliding distance, as shown in Figure 7-3(c). The rate of volume loss decreases with the decreasing stress. Note that the FEA simulations used the stress distribution wear model (eq. (7.1)), however, the volume loss and average stress also appeared to correlate well.

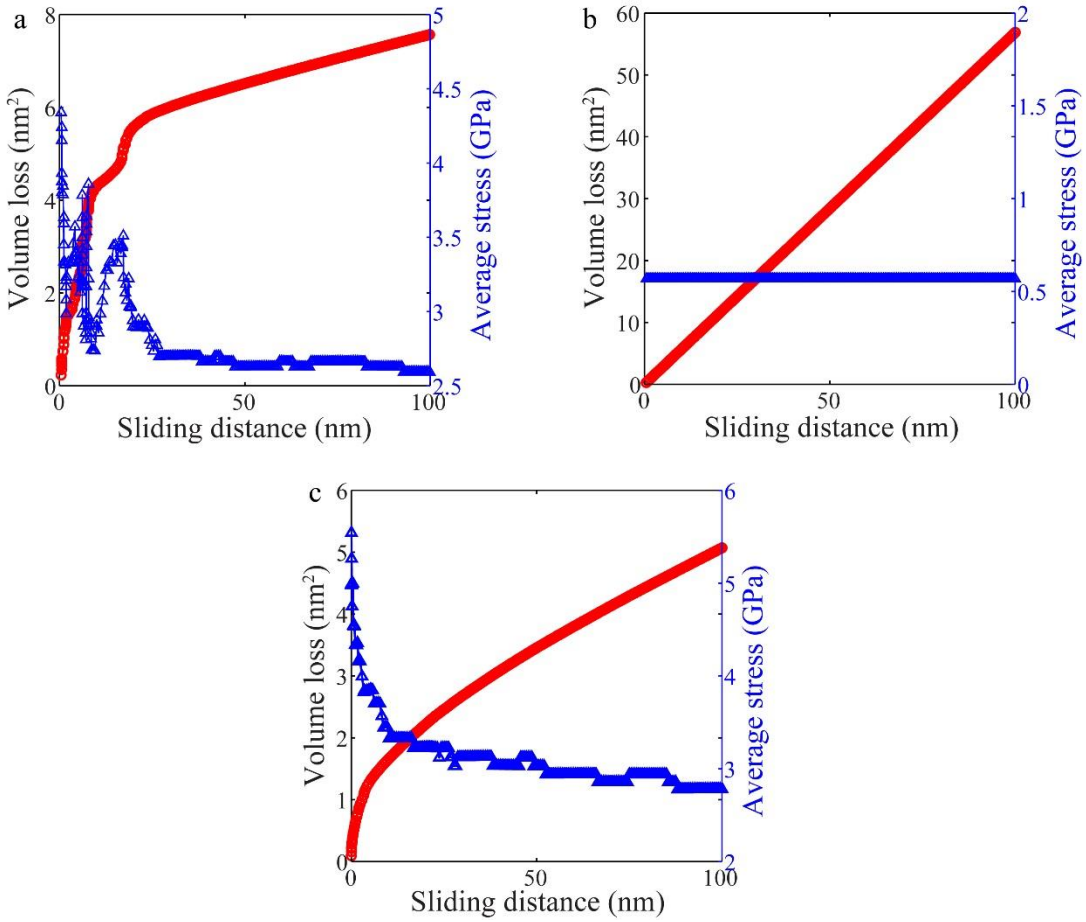

Figure 7-3. Volume loss and average stress as a function of sliding distance during FEA wear simulations of (a) DLC wear (tip and substrate have identical values) in DLC-DLC, (b) PMMA substrate wear in DLC-PMMA contact, and (c) DLC tip wear in DLC-UNCD contact.

7.3.2 Effect of friction

Frictionless contact models, such as Hertz model and DMT model, are often used to analyze stress in nanoscale asperity contacts and wear studies [44], [77]. However, friction can affect the contact stress distribution at the interface [111]. The effect of friction in application of nanoscale wear models has not been studied yet. Here, four cases of DLC tip on DLC substrate wear, with different friction coefficients, i.e. μ=0, 0.3, 0.5 and 0.8, were simulated. The applied normal load was 10 nN/nm and the sliding distance was 50 nm. In addition to the boundary conditions specified previously, a lateral force, which had a magnitude equal to the product of the friction coefficient and normal load, was applied at the bottom boundary of substrate from right to left.

The normal stress and shear stress distributions for frictionless (μ=0) and a frictional case (μ=0.8) are shown in Figure 7-4. The stress distributions were calculated at sliding distance of 0 nm, where no wear had happened and both the geometries of tip and substrate were symmetric. Thus, the stress distributions are symmetric (Figure 7-4(a) and (b)). In the case of μ=0.8, the distribution of normal stress became asymmetric and the peak stress shifted to the front of sliding (Figure 7-4(c)). A larger shear stress was observed at the interface (Figure 7-4(d)).

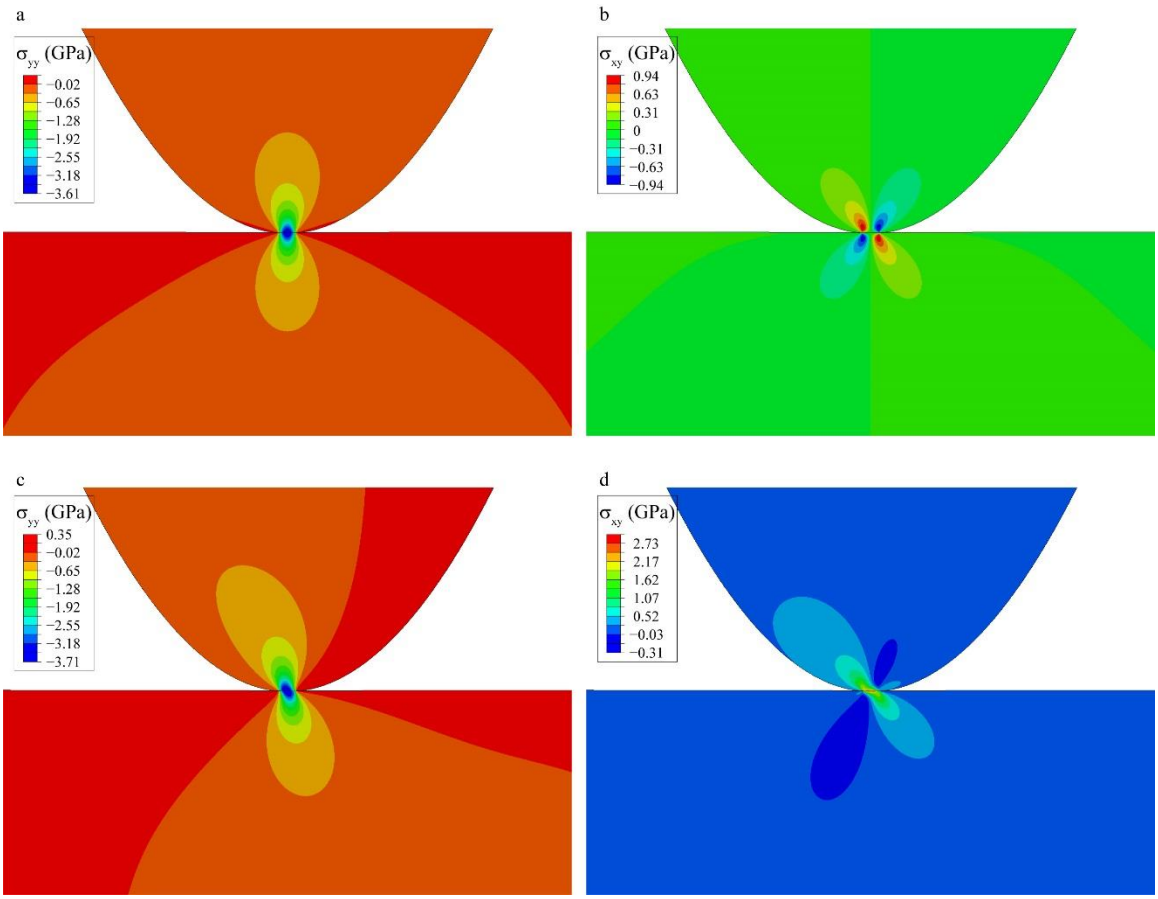

Figure 7-4. Normal stress and shear stress distribution for DLC-DLC contact with friction coefficient (a, b) μ=0 and (c, d) μ=0.8, respectively. The sliding distance is 0 nm and the substrate starts moving to the left.

The normal and shear contact stress at the interface are plotted in Figure 7-5 for all four μ values examined. In the normal stress results, the distribution shifts slightly to the right when friction is applied. While the magnitude of the normal stress had no significant increment from μ=0 to μ=0.8 (Figure 7-5(a)). Only minimal shear stress was seen when μ=0 and the shear stress increased significantly with friction coefficient. The peak shear stress increased from 1.12 GPa (μ=0.3) to 2.77 GPa (μ=0.8) as shown in Figure 7-5(b).

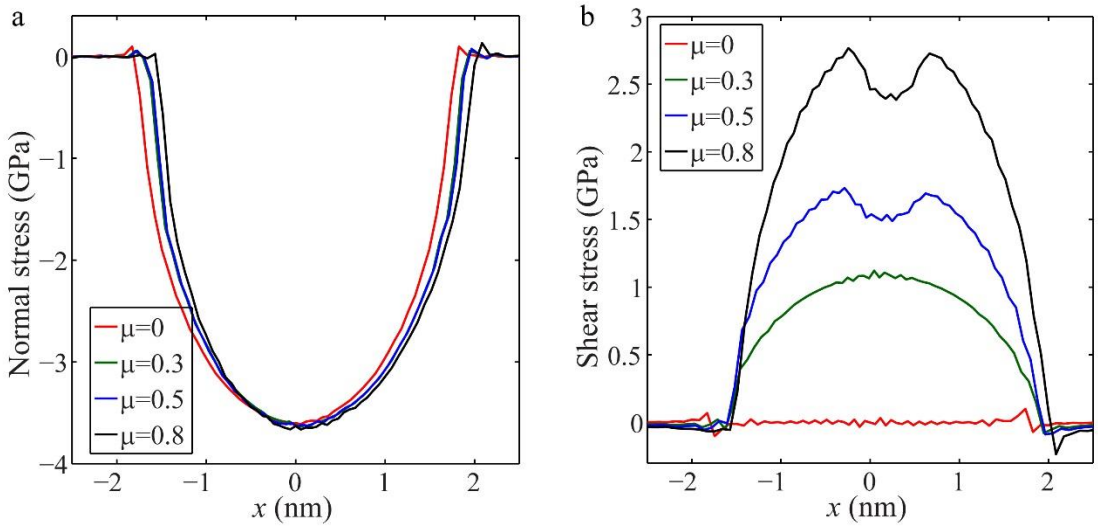

Figure 7-5. FEA results of (a) normal stress and (b) shear stress at the interface of DLC tip and DLC substrate with different friction coefficients.

The wear simulations using the wear criteria eq. (7.1) were performed for a sliding distance of 50 nm. With different friction coefficients, the normal stress results didn't vary significantly as shown in Figure 7-6. For μ=0-0.8, all four cases had similar changes in both average normal stress and volume loss during the wear process. The average normal stress fluctuated and generally decreased as the geometries of tip and substrate changed during sliding as discussed in previous section. The differences in normal stress only results in minimal differences in volume loss (Figure 7-6(b)) for different friction coefficients. These simulation results indicate that it is a reasonable assumption to use frictionless mechanical models for stress analysis of experimental data [44], [77].

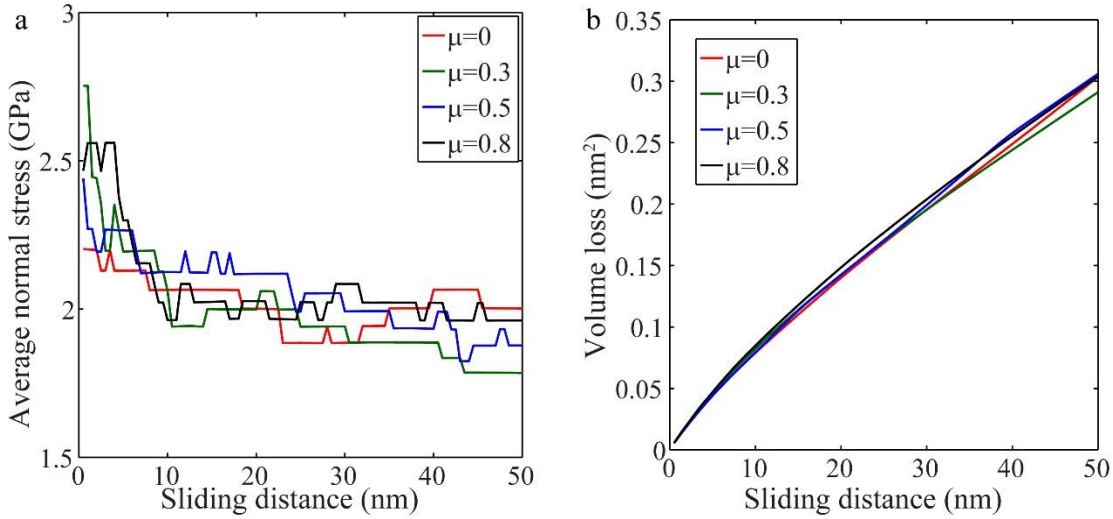

Figure 7-6. (a) Average normal stress and (b) volume loss as a function of sliding distance calculated from FEA simulations with different friction coefficients.

7.3.3 Effect of surface roughness

To study the effect of surface roughness on wear, FEA simulations of a paraboloidal DLC tip (R=20 nm) against several different rough substrates, as well as a flat smooth substrate, were carried out. The load was 10 nN/nm in all cases and the sliding include a forward (substrate moving from right to left) 50 nm and a backward 50 nm. Three cases of random roughness were generated by superposing five sine functions with randomly selected amplitudes, wave lengths and phases. Three random roughness distributions were used:

$$r_1 = 3sin(x/7.577\pi + 0.8147) + 2.5sin(x/1.712\pi + 0.0975) + 2sin(x/3.922\pi + 0.1576) + 1.5sin(x/6.555\pi + 0.1419) + sin(x/7.431\pi + 0.6557) \quad (7.2)$$

$$r_2 = 2.5sin(x/8.229\pi + 0.3309) + 2.5sin(x/1.942\pi + 0.9544) + 2sin(x/6.985\pi + 0.4076) + 1.5sin(x/5.709\pi + 0.82) + sin(x/7.959\pi + 0.7184) \quad (7.3)$$

$$r_3 = 3sin(x/8.147\pi + 0.157) + 2.5sin(x/19.06\pi + 0.9875) + 2sin(x/1.27\pi + 0.5469) + 1.5sin(x/0.9134\pi + 0.2785) + sin(x/6.324\pi + 0.0975) \quad (7.4)$$

To control the rms roughness of random roughness, different prefactors were used to multiply to r_1, r_2 and r_3, respectively. The geometries of the roughness and asperities distributions are shown in Figure 7-7. In FEA simulations, each random roughness had 3 different prefactors multiplied, i.e. 3 different rms roughness, but the identical distributions of peaks and valleys.

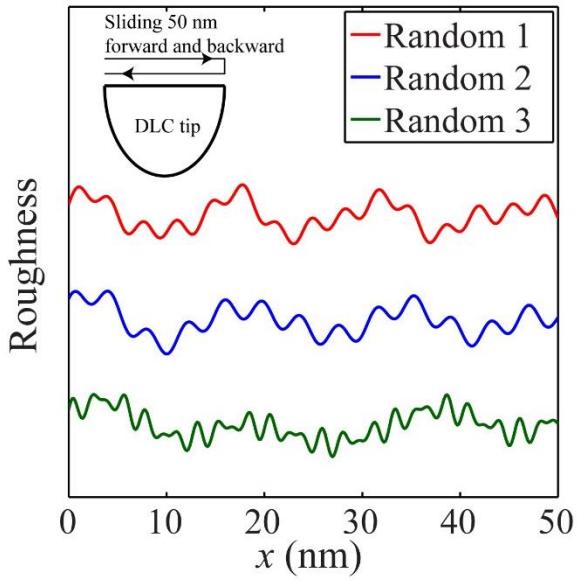

Figure 7-7. The random roughness cases used in FEA simulations. The rms roughness of each case is controlled by changing the amplitude of the whole roughness functions (eq. (7.2)-(7.4)).

In Figure 7-8(a), the volume loss as a function of sliding distance are shown for cases with different roughness distribution and different rms roughness, as well as for a smooth flat substrate case. The different colors and markers indicated the cases of random roughness used and the values in the right column indicated the rms roughness for each

case. The volume loss increased sublinearly with sliding distance for all cases. Generally, with higher rms roughness, higher volume loss was seen. For the cases with roughness, clear changes of slopes were observed before and after 50 nm, where the sliding direction changed from forward to backward. When sliding backward, substrate was worn and the peaks in roughness were expected to be less sharp due to the forward sliding and resulted in less volume loss. As also seen in the average stress distribution (Figure 7-8(b)), strong fluctuations in stress were observed before 50 nm and then less fluctuation is seen in 50-100 nm of sliding. The results from the flat case show that the stress gradually reduces during sliding, which is consistent with results in previous section. Unlike the smooth-smooth wear simulations in previous section, there is not a clear correlation between average normal stress and volume loss behavior for the cases with the roughness.

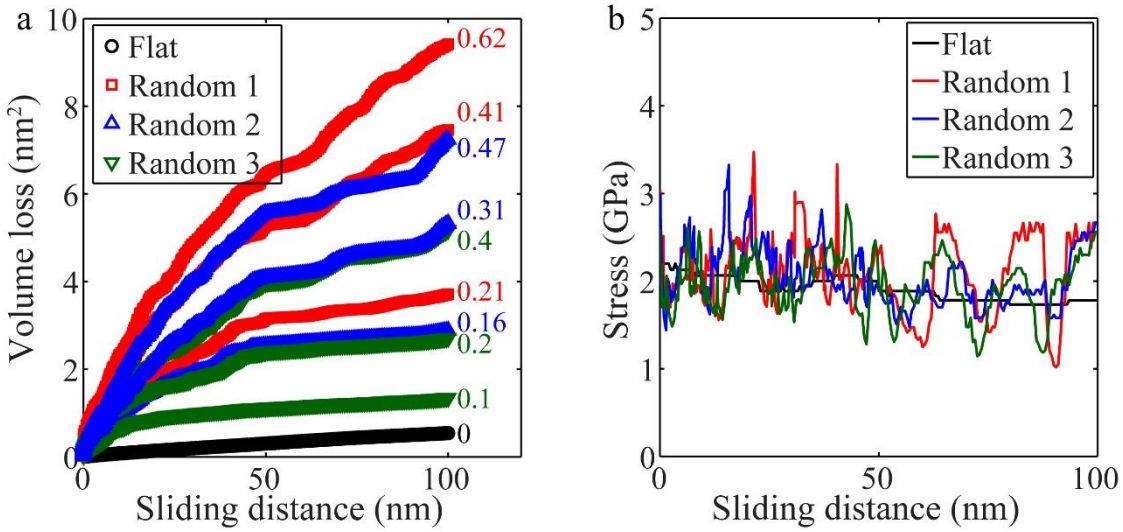

Figure 7-8. (a) Volume loss and (b) average normal stress as a function of sliding distance. The DLC substrate is sliding forward (right to left) for sliding distance from 0 to 50 nm and sliding backward (left to right) from 50 to 100 nm. The numbers listed at the right of the curves in (a) indicate the rms roughness in unit of nm. Rms= 0.41, 0.31 and 0.2 nm for the cases shown in (b).

As the rms roughness was calculated for the unworn roughness, the volume loss of the first 50 nm sliding was used to quantify the effect of roughness on wear. The volume loss and the corresponding rms roughness were plotted in Figure 7-9. An increasing volume loss with increasing rms roughness was observed. The simulated results for all random roughness cases and a flat smooth substrate case were fit to a linear line as shown in Figure 7-9

$$V_{loss} = 10.1rms + 0.565 \quad (7.5)$$

The fit had R^2=0.95. Considering the complicated nature of roughness and the complex geometry evolution that occurs during wear, the dependence of simulated volume loss on roughness shows a promising start for further detailed simulations and experimental works of the effect of roughness on nanoscale wear.

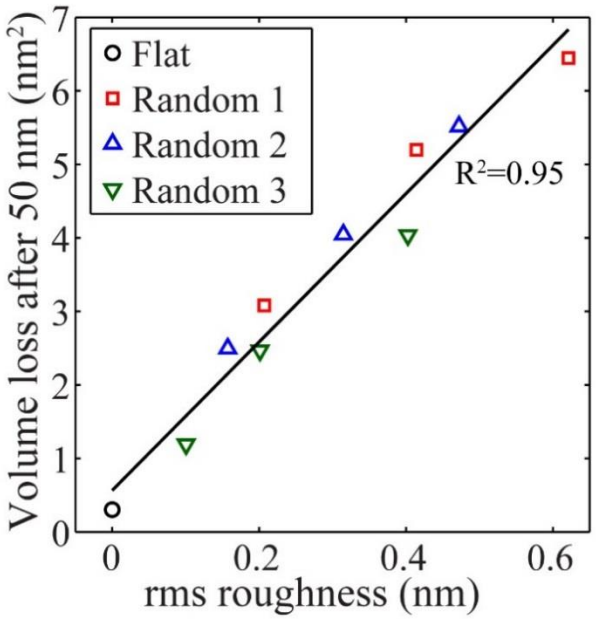

Figure 7-9. The volume loss after 50 nm sliding on substrates with different rms roughness.

7.4 3D simulation of PMMA line wear

3D simulations of a DLC tip on PMMA sample were performed to mimic the line wear experiments reported in Chapter 4. The DLC tip had a paraboloidal geometry and the radius was 10 nm. The load was kept as constant 56 nN and the simulations included forward and backward sliding of 10 nm for a total sliding distance of 32 nm.

The tip-sample contact and sliding resulted in a wear track in the PMMA surface. The evolution of wear track is shown in Figure 7-10(a). The DLC tip was located at the center of the sample and the sample was sliding in the direction indicated in the figure. The DLC tip was not shown for the convenience of observation. The geometry of DLC tip had minimal changes due to the input wear parameters in Table 7-1. The σ_{zz} stress distributions changed as the wear track formed. The stress distributions at the cross section at the plane along wear direction were shown in Figure 7-10(b). The magnitude of the stress decreases as the sliding distance increased and the wear track becomes deeper. A symmetric stress distribution was seen at a sliding distance of 0 nm. After the wear simulation began, higher stress was observed at the sliding front (against the sliding direction of substrate). This was consistent with what was observed in previous 2D simulations.

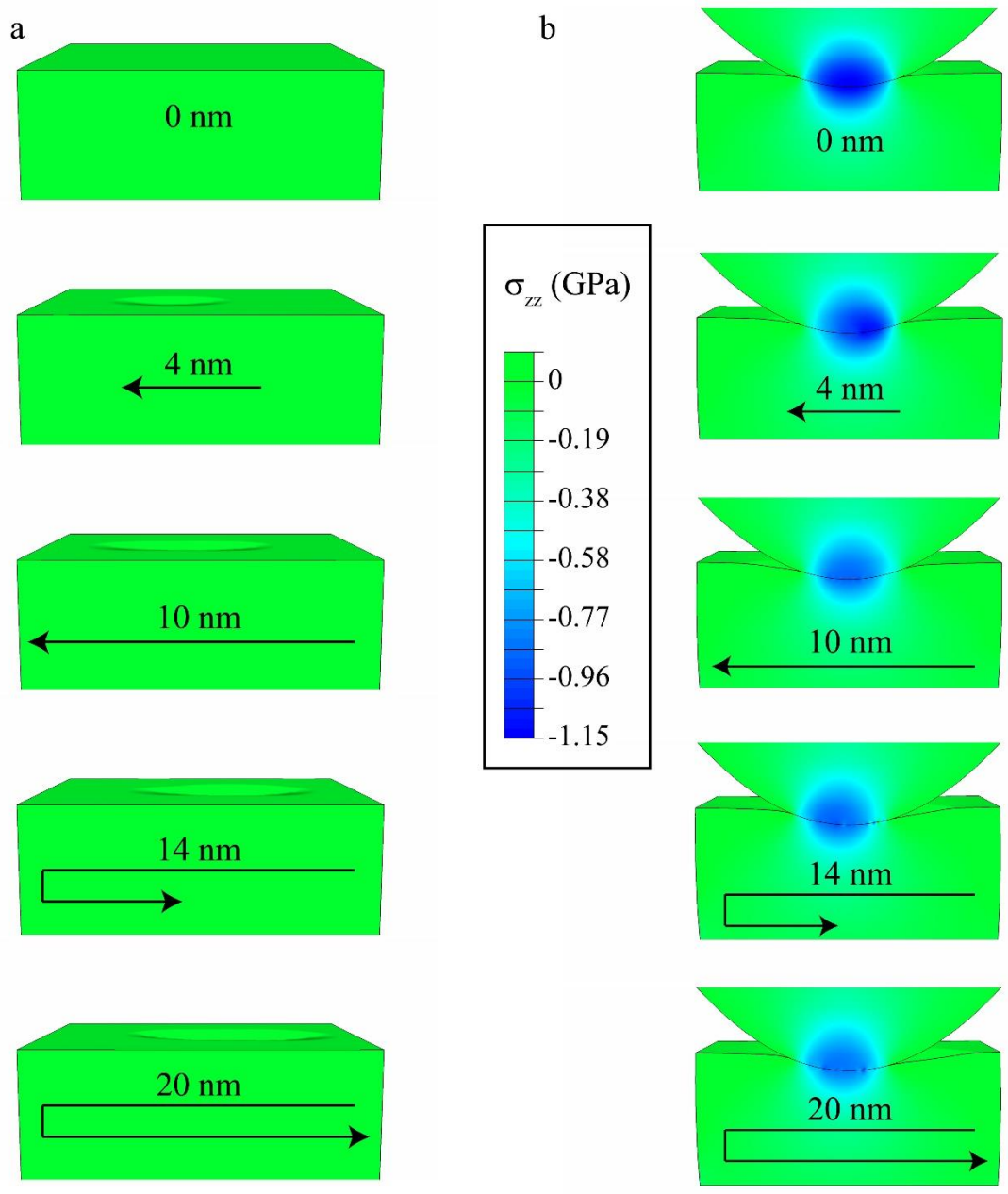

Figure 7-10. (a) Wear track formation on PMMA sample during sliding and (b) variations of normal stress distribution observed at the cross section along the center of wear track during wear simulations.

To compare with line wear experimental results, the incremental height loss of PMMA, i.e. the depth variation of the wear track, was plotted in Figure 7-11 as a function of tip sliding distance. A linear fit for the initial part of the data (0 to 6 nm) indicated that the height loss from 3D FEA simulations increased sublinearly with sliding distance. Although it is difficult to do quantitative comparison to the experiments due to the different tip geometry and short sliding distance simulated, the simulated results are qualitatively consistent with the experimental wear behavior in AFM line wear tests.

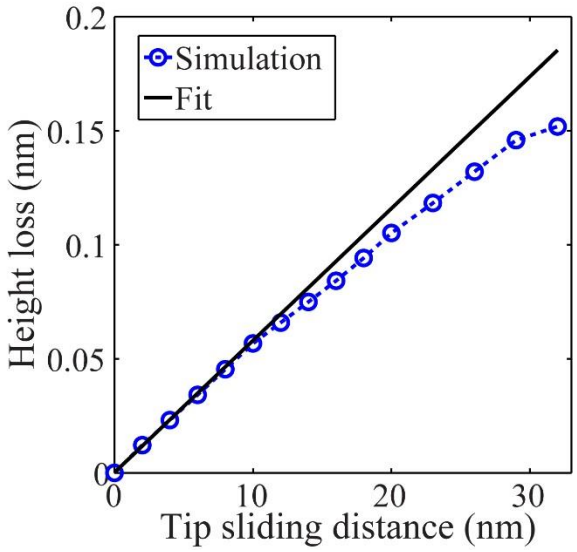

Figure 7-11. Cumulative height loss of PMMA calculated from FEA simulations. A linear fit to the first 6 nm data indicates a sublinear trend of increasing height loss.

7.5 Summary

An FEA wear simulation algorithm using a custom Matlab-Abaqus iterative program was developed and used in this chapter. A transition state theory stress distribution

model is applied as the local wear criteria in the simulations. 2D and 3D simulations are performed for case studies. In all simulations, the simultaneous evolution of the geometry and stress are predicted.

In the 2D simulations, different contacting materials pairs with different stiffness and different friction coefficients and smooth tip-sample interfaces were examined. The height/volume variations, though calculated by stress distribution model, have correlation to the average normal stress. Once the roughness is added on the interfacial geometries, significant wear behaviors are presented. The volume loss increases sublinearly with sliding distance, while average stress fluctuates and has no correlation to the volume loss anymore. The volume loss after the first cycle of wear over the initial substrate geometry shows a linear dependence of rms roughness. The 3D DLC tip on PMMA substrate simulations show a sublinear height loss as a function of sliding distance, which is consistent with the observation in AFM based line wear experiments.

The developed numerical program provides a way to monitor the details of the stress variation and geometry evolution during wear and can be used as a tool for understanding nanoscale wear.

CHAPTER 8: Conclusions and contributions

8.1 Conclusions

Atomic force microscopy (AFM) is a powerful and ubiquitous tool for measuring and manipulating matter at the nanoscale, such as nanometrology, nanolithography and tip-based nanomanufacturing. In many of these nanoscale techniques, the hard AFM tip interacts with a polymer as a substrate materials. For example, high resolution 2D patterns and 3D structures are often fabricated in thin polymer layers [1], [2], [4], [12], [14], [15]. An understanding of the nanoscale adhesion and wear behavior of the tip-sample contact is important in the design of tip-based nanomanufacturing processes to produce structures in the polymer layers as well as avoiding damage of polymer layers in nanometrology applications.

In the work on nanoscale adhesion in this dissertation, a new approach that combines AFM pull-off measurements and detailed characterization of the 3D geometry of the AFM tip was developed to characterize the adhesive traction-separation relation of nanoscale contacts. The properties of the adhesive traction-separation relation between UNCD AFM tips and PMMA thin films were quantified with this method. The method requires measurements from a minimum of two tips with different geometries; three tips were used in this work to illustrate the overall robustness of this approach. The measurement data was analyzed using two common traction-separation laws: the Dugdale relation and 3-9 Lennard-Jones potential. The Dugdale analysis resulted in adhesion range

h_{ad}=2.46-2.49 nm and work of adhesion W_a=49.6±0.8 mJ/m^2, while the 3-9 Lennard-Jones traction-separation law resulted in z_0=1.53-2.02 nm and W_a=51.4±2.4 mJ/m^2. Similar work of adhesion was obtained regardless of whether the Dugdale or 3-9 Lennard-Jones traction-separation law was applied in analysis. The peak adhesive stresses in the traction separation law differed by about 50%, suggesting that it might be more appropriate to set $\sigma_{LJ-max} \approx 1.5\sigma_D$ instead of $\sigma_{LJ-max} \approx \sigma_D$ as is sometimes assumed in analyses that define equivalent Dugdale and Lennard-Jones potentials.

The wear of PMMA at nanoscale was investigated by AFM-based wear experiments and finite element-based mechanics analysis. Load controlled experiments were performed on e-beam patterned PMMA structures. Rectangular and square PMMA structures with sizes of several hundred of nanometers were fabricated on a silicon wafer. The exposed silicon surface in the gaps between the PMMA structures provided a flat reference surfaces for measuring the height of the patterns over the course of the wear test. The gaps between PMMA structures also allowed the wear debris to be captured. For each UNCD AFM tip used in wear tests, the 3D tip geometries were measured using an inverse AFM imaging technique. The measured geometries were then used in FEA calculations to determine the stress distribution and contact area at tip-sample interface. The simulations, which were performed for all tips, examined the effect of two cases of constitutive behaviors for the PMMA. The overall experimental design, tip characterization, and FEA was used in PMMA wear experiments at room and elevated temperature.

At room temperature, load controlled AFM-based line and raster wear tests were performed using three different UNCD tips. The line wear data was analyzed using transition state theory and the activation energy and effective activation volume for PMMA were extracted using two different implementations of the wear model: average stress model and stress distribution model. Fitting of the models to the experimental data indicates that the transition state models describe the experimental data well. This suggests an atom-by-atom attrition mechanism for the nanoscale polymer wear. The analyses that use contact stress distribution results in a narrower range of activation parameters, i.e. 0.67 eV$\leq E_a \leq$ 0.69 eV and 11.3 Å$^3 \leq V_{eff} \leq$ 24.8 Å^3 from stress distribution model, and 0.67 eV$\leq E_a \leq$ 0.73 eV and 16 Å$^3 \leq V_{eff} \leq$ 51.8 Å^3 from average stress model. Using these parameters and transition state theory models, the predictions of volume loss rates in raster wear tests done with tips with different geometries were performed. The predicted volume loss rates were quite close to those measured from raster wear experiments. For the stress distribution model, which demonstrates a more accurate prediction, there was a 7.8% difference between the predictions and experimental results.

AFM-based raster wear tests of PMMA were then performed at varying temperatures between 300.8 K and 338.9 K, in order to study the temperature dependence of wear mechanism. In these experiments, PMMA samples were mounted on a heating stage in a dry nitrogen environment. The surface temperature before contacting a UNCD tip was measured by a thermocouple and the temperature at the tip-sample contact was estimated by FEA to consider the thermal conductivity of the AFM probe. The measured

volume loss rate almost doubled with increasing temperature. However, the transition state theory parameters obtained from the room temperature data significantly overestimates the increase in wear rate with temperature. The transition state theory models overestimate the volume loss rate by more than one order of magnitude at the higher temperatures. A modified transition state theory wear model, which combines temperature-dependent viscoelastic relaxation of PMMA as well as thermally activated atom-by-atom attrition, is developed to describe the wear data at multiple temperatures. By applying time-temperature superposition, a shift factor is determined and it is believed to be related to the activation energy of ester group rotation in PMMA. The modified models describe the experimental data over the range of temperatures characterized. The modified stress distribution model results in the best estimation of wear across the temperature range with differences ranging from 13.1% to 19.4% at different temperatures.

In addition to the nanoscale wear experiments, microscale experiments were performed to evaluate the applicability of transition state theory in larger scale. Microscale line wear experiments were performed in a nanoindentation system with a 1 μm spherical diamond indenter under load control (20-200 μN). The wear tracks were characterized by high resolution AFM measurements. The results in the microscale tests did not follow Archard's law, but rather exhibited a sublinear relationship between wear volume and sliding distance at a fixed load. Despite the fact that both load and contact area were 2 to 3 orders of magnitude larger in microscale tests than those in nanoscale tests, the relationship

between wear volume and normal contact stress was appropriately described by a transition state theory model.

Finally, studies on stress and geometry evolution during sliding due to wear was investigated using a new iterative FEA program that was implemented in Matlab and Abaqus. A transition state theory stress distribution model was applied as the local wear criteria in the simulations. In all 2D and 3D simulations that were performed, the evolution of the geometry and stress distributions due to wear were observed. In the 2D cases, simulations with different contacting materials pairs with different stiffness, wear properties and different friction coefficients were performed. The volume loss, although calculated by stress distribution model, show correlation to the average normal stress. Simulations that incorporate roughness showed a significant effect of roughness on wear behaviors and overall wear rate. Surface roughness with different rms values were added on substrate and result in strong fluctuations in average normal stress. In the presence of roughness, a correlation between volume loss and average stress is no longer observed. The results also indicate a positive correlation between volume loss and rms roughness. 3D wear simulations of DLC tip on PMMA substrate were performed to facilitate comparison between the experiments and simulations. The 3D simulations show a sublinear relationship between height loss and sliding distance, which is consistent with experimental behavior.

8.2 Contributions

This dissertation has made multiple contributions in characterization and understanding of the nanoscale adhesion and wear of PMMA surfaces. The key contributions are:

- Development of a novel approach for the measurement of range and strength of adhesion, as well as work of adhesion, between UNCD-PMMA interfaces. This approach combines AFM pull-off force measurements and characterization of 3D nanoscale geometries of AFM tips. This approach can be extended to other pairs of materials contacting at nanoscale as long as the materials are stiff enough to have minimal deformation under adhesion.

- A novel experimental design of using nanopatterned structures and AFM-based wear experiments. The design uses gaps between structures to capture debris due to wear and minimize its influence on the wear process and measurements. The data collected from simple line wear experiments on PMMA could be described by transition state theory wear models. Using the extracted wear parameters, the prediction of volume loss rates in nanoscale raster wear experiments was shown.

- Investigation of the effect of temperature on polymer nanoscale wear and the development of a modified transition state theory wear model. The studies illustrate the importance of temperature on nanoscale wear of polymers. The modified models can

describe the experimental data and imply a polymer wear process that combines viscoelastic relaxation and atom-by-atom attrition at nanoscale.

- Development and use of an iterative FEA wear simulation method. This numerical technique can be used for detailed study of the simultaneous evolution in stress and geometry in wear process, as well as systematically studying cases with different contact conditions. It can also be used as a complementary tool for helping further experimental research of nanoscale wear.

BIBLIOGRAPHY

[1] A. W. Knoll, D. Pires, O. Coulembier, P. Dubois, J. L. Hedrick, J. Frommer, and U. Duerig, "Probe-based 3-D nanolithography using self-amplified depolymerization polymers.," *Adv. Mater.*, vol. 22, no. 31, pp. 3361–3365, Aug. 2010.

[2] D. Pires, J. L. Hedrick, A. De Silva, J. Frommer, B. Gotsmann, H. Wolf, M. Despont, U. Duerig, and A. W. Knoll, "Nanoscale three-dimensional patterning of molecular resists by scanning probes.," *Science*, vol. 328, no. 5979, pp. 732–735, May 2010.

[3] D. Wang, V. K. Kodali, W. D. Underwood, J. E. Jarvholm, T. Okada, S. C. Jones, M. Rumi, Z. Dai, W. P. King, S. R. Marder, J. E. Curtis, and E. Riedo, "Thermochemical nanolithography of multifunctional nanotemplates for assembling nano-objects," *Adv. Funct. Mater.*, vol. 19, no. 23, pp. 3696–3702, 2009.

[4] C. Martín, G. Rius, X. Borrisé, and F. Pérez-Murano, "Nanolithography on thin layers of PMMA using atomic force microscopy," *Nanotechnology*, vol. 16, no. 8, pp. 1016–1022, Aug. 2005.

[5] H. Sugimura, T. Uchida, N. Kitamura, and H. Masuhara, "Tip-induced anodization of titanium surfaces by scanning tunneling microscopy: A humidity effect on nanolithography," *Appl. Phys. Lett.*, vol. 63, no. 9, pp. 1288–1290, 1993.

[6] U. Kunze and B. Klehn, "Plowing on the Sub-50 nm Scale: Nanolithography Using Scanning Force Microscopy," *Adv. Mater.*, vol. 11, no. 17, pp. 1473–1475, Dec.

1999.

[7] X. N. Xie, H. J. Chung, C. H. Sow, and A. T. S. Wee, “Nanoscale materials patterning and engineering by atomic force microscopy nanolithography,” *Materials Science and Engineering R: Reports*, vol. 54, no. 1–2. pp. 1–48, 2006.

[8] R. D. Piner, J. Zhu, F. Xu, S. Hong, and C. A. A. Mirkin, “‘Dip-Pen’ Nanolithography,” *Science*, vol. 283, no. 5402, pp. 661–663, 1999.

[9] C. A. Mirkin, “The power of the pen: development of massively parallel dip-pen nanolithography,” *ACS Nano*, vol. 1, no. 2, pp. 79–83, 2007.

[10] M. R. Falvo, G. Clary, A. Helser, S. Paulson, R. M. Taylor, V. Chi, F. P. Brooks, S. Washburn, and R. Superfine, “Nanomanipulation experiments exploring frictional and mechanical properties of carbon nanotubes,” *Microsc. Microanal.*, vol. 4, no. 5, pp. 504–512, 1998.

[11] S. Cruchon-Dupeyrat, S. Porthun, and G. Y. Liu, “Nanofabrication using computer-assisted design and automated vector-scanning probe lithography,” *Appl. Surf. Sci.*, vol. 175–176, pp. 636–642, 2001.

[12] Y. Wang, X. Hong, J. Zeng, B. Liu, B. Guo, and H. Yan, “AFM tip hammering nanolithography,” *Small*, vol. 5, no. 4, pp. 477–483, Apr. 2009.

[13] B. Cappella and H. Sturm, “Comparison between dynamic plowing lithography and nanoindentation methods,” *J. Appl. Phys.*, vol. 91, no. 1, pp. 506–512, 2002.

[14] Y. Yan, X. Zhao, Z. Hu, and D. Gao, “Effects of Atomic Force Microscope Silicon

Tip Geometry on Large-Scale Nanomechanical Modification of the Polymer Surface," *Tribol. Trans.*, vol. 55, no. 6, pp. 846–853, Nov. 2012.

[15] L. Porter, A. Ribbe, and J. Buriak, "Metallic nanostructures via static plowing lithography," *Nano Lett.*, vol. 3, no. 8, pp. 1043–1047, 2003.

[16] B. Klehn and U. Kunze, "Nanolithography with an atomic force microscope by means of vector-scan controlled dynamic plowing," *J. Appl. Phys.*, vol. 85, no. 7, p. 3897, 1999.

[17] Y.-J. Chen, J.-H. Hsu, and H.-N. Lin, "Fabrication of metal nanowires by atomic force microscopy nanoscratching and lift-off process," *Nanotechnology*, vol. 16, no. 8, pp. 1112–1115, Aug. 2005.

[18] L. L. Sohn and R. L. Willett, "Fabrication of nanostructures using atomic-force-microscope-based lithography," *Appl. Phys. Lett.*, vol. 67, no. 11, p. 1552, 1995.

[19] A. A. Tseng, "Three-dimensional patterning of nanostructures using atomic force microscopes," *J. Vac. Sci. Technol. B Microelectron. Nanom. Struct.*, vol. 29, no. 4, p. 040801, 2011.

[20] M. Heyde, K. Rademann, B. Cappella, M. Geuss, H. Sturm, T. Spangenberg, and H. Niehus, "Dynamic plowing nanolithography on polymethylmethacrylate using an atomic force microscope," *Rev. Sci. Instrum.*, vol. 72, no. 1, p. 136, 2001.

[21] E. Dubois and J. Bubbendorff, "Nanometer scale lithography on silicon, titanium and PMMA resist using scanning probe microscopy," *Solid. State. Electron.*, vol.

43, pp. 1085–1089, 1999.

[22] T. A. Jung, A. Moser, H. J. Hug, D. Brodbeck, R. Hofer, H. R. Hidber, and U. D. Schwarz, "The atomic force microscope used as a powerful tool for machining surfaces," *Ultramicroscopy*, vol. 42–44, pp. 1446–1451, Jul. 1992.

[23] W. Brostow, M. Dutta, J. Ricardo de Souza, P. Rusek, A. Marcos de Medeiros, and E. N. Ito, "Nanocomposites of poly(methyl methacrylate) (PMMA) and montmorillonite (MMT) Brazilian clay: A tribological study," *eXPRESS Polym. Lett.*, vol. 4, no. 9, pp. 570–575, Aug. 2010.

[24] S. Gross, D. Camozzo, V. Di Noto, L. Armelao, and E. Tondello, "PMMA: A key macromolecular component for dielectric low-κ hybrid inorganic–organic polymer films," *Eur. Polym. J.*, vol. 43, no. 3, pp. 673–696, Mar. 2007.

[25] A. Akinci, S. Sen, and U. Sen, "Friction and wear behavior of zirconium oxide reinforced PMMA composites," *Compos. Part B Eng.*, vol. 56, pp. 42–47, Jan. 2014.

[26] A. Karimzadeh and M. R. Ayatollahi, "Investigation of mechanical and tribological properties of bone cement by nano-indentation and nano-scratch experiments," *Polym. Test.*, vol. 31, no. 6, pp. 828–833, Sep. 2012.

[27] Z.-B. Cai, S.-S. Gao, M.-H. Zhu, X.-Z. Lin, J. Liu, and H.-Y. Yu, "Tribological behavior of polymethyl methacrylate against different counter-bodies induced by torsional fretting wear," *Wear*, vol. 270, no. 3–4, pp. 230–240, Jan. 2011.

[28] J. Liu, D. S. Grierson, N. Moldovan, J. Notbohm, S. Li, P. Jaroenapibal, S. D.

O'Connor, A. V Sumant, N. Neelakantan, J. A. Carlisle, K. T. Turner, and R. W. Carpick, "Preventing nanoscale wear of atomic force microscopy tips through the use of monolithic ultrananocrystalline diamond probes.," *Small*, vol. 6, no. 10, pp. 1140–1149, May 2010.

[29] B. Bhushan and K. J. Kwak, "Velocity dependence of nanoscale wear in atomic force microscopy," *Appl. Phys. Lett.*, vol. 91, no. 16, p. 163113, 2007.

[30] J. S. S. S. Wong, H.-J. J. Sue, K.-Y. Y. Zeng, R. K. Y. Y. Li, and Y.-W. W. Mai, "Scratch damage of polymers in nanoscale," *Acta Mater.*, vol. 52, no. 2, pp. 431–443, Jan. 2004.

[31] D. S. Grierson, J. Liu, R. W. Carpick, and K. T. Turner, "Adhesion of nanoscale asperities with power-law profiles," *J. Mech. Phys. Solids*, vol. 61, no. 2, pp. 597–610, Sep. 2013.

[32] T. D. B. Jacobs, K. E. Ryan, P. L. Keating, D. S. Grierson, J. A. Lefever, K. T. Turner, J. A. Harrison, and R. W. Carpick, "The Effect of Atomic-Scale Roughness on the Adhesion of Nanoscale Asperities: A Combined Simulation and Experimental Investigation," *Tribol. Lett.*, vol. 50, pp. 81–93, Feb. 2013.

[33] T. D. B. Jacobs, J. A. Lefever, and R. W. Carpick, "Measurement of the Length and Strength of Adhesive Interactions in a Nanoscale Silicon-Diamond Interface," *Adv. Mater. Interfaces*, vol. 2, p. 1400547, 2015.

[34] J. Katainen, M. Paajanen, E. Ahtola, V. Pore, and J. Lahtinen, "Adhesion as an

interplay between particle size and surface roughness," *J. Colloid Interface Sci.*, vol. 304, no. 2, pp. 524–529, 2006.

[35] N. Miki and S. M. Spearing, "Effect of nanoscale surface roughness on the bonding energy of direct-bonded silicon wafers," *J. Appl. Phys.*, vol. 94, no. 10, pp. 6800–6806, 2003.

[36] A. G. Peressadko, N. Hosoda, and B. N. J. Persson, "Influence of Surface Roughness on Adhesion between Elastic Bodies," *Phys. Rev. Lett.*, vol. 95, no. 12, p. 124301, Sep. 2005.

[37] R. Berger, Y. Cheng, R. Förch, B. Gotsmann, J. S. Gutmann, T. Pakula, U. Rietzler, W. Schärtl, M. Schmidt, A. Strack, J. Windeln, and H.-J. Butt, "Nanowear on polymer films of different architecture.," *Langmuir*, vol. 23, no. 6, pp. 3150–6, Mar. 2007.

[38] G. Haugstad, W. Gladfelter, and E. Weberg, "Probing molecular relaxation on polymer surfaces with friction force microscopy," *Langmuir*, vol. 5, no. 21, pp. 3473–3482, 1995.

[39] X. Jin and W. N. Unertl, "Submicrometer modification of polymer surfaces with a surface force microscope," *Appl. Phys. Lett.*, vol. 61, no. 6, p. 657, 1992.

[40] T. D. B. Jacobs, B. Gotsmann, M. A. Lantz, and R. W. Carpick, "On the application of transition state theory to atomic-scale wear," *Tribol. Lett.*, vol. 39, no. 3, pp. 257–271, Jul. 2010.

[41] M. A. Lantz, B. Gotsmann, P. Jaroenapibal, T. D. B. Jacobs, S. D. O'Connor, K. Sridharan, and R. W. Carpick, "Wear-Resistant Nanoscale Silicon Carbide Tips for Scanning Probe Applications," *Adv. Funct. Mater.*, vol. 22, pp. 1639–1645, Feb. 2012.

[42] H. Bhaskaran, B. Gotsmann, A. Sebastian, U. Drechsler, M. a Lantz, M. Despont, P. Jaroenapibal, R. W. Carpick, Y. Chen, and K. Sridharan, "Ultralow nanoscale wear through atom-by-atom attrition in silicon-containing diamond-like carbon," *Nat. Nanotechnol.*, vol. 5, no. 3, pp. 181–5, Mar. 2010.

[43] B. Gotsmann and M. Lantz, "Atomistic Wear in a Single Asperity Sliding Contact," *Phys. Rev. Lett.*, vol. 101, no. 12, pp. 1–4, Sep. 2008.

[44] T. D. B. Jacobs and R. W. Carpick, "Nanoscale wear as a stress-assisted chemical reaction," *Nat. Nanotechnol.*, vol. 8, no. 2, pp. 108–112, Feb. 2013.

[45] E. Boschung, M. Heuberger, and G. Dietler, "Energy dissipation during nanoscale indentation of polymers with an atomic force microscope," *Appl. Phys. Lett.*, vol. 64, no. 26, pp. 3566–3568, 1994.

[46] H. Hertz, "Über die berührung fester elastischer Körper (On the contact of rigid elastic solids)," *J. reine und Angew. Math. 92*, pp. 156–171, 1896.

[47] Z. Zheng and J. Yu, "Using the Dugdale approximation to match a specific interaction in the adhesive contact of elastic objects," *J. Colloid Interface Sci.*, vol. 310, no. 1, pp. 27–34, Jun. 2007.

[48] K. L. Johnson, K. Kendall, and A. D. Roberts, “Surface energy and the contact of elastic solids,” *Proc. R. Soc. A Math. Phys. Eng. Sci.*, vol. 324, no. 1558, pp. 301–313, Sep. 1971.

[49] B. Derjaguin, V. Muller, and Y. P. Toporov, “Effect of contact deformations on the adhesion of particles,” *J. Colloid Interface Sci.*, vol. 53, no. 2, pp. 314–326, 1975.

[50] D. Tabor, “Surface forces and surface interactions,” *J. Colloid Interface Sci.*, vol. 58, no. 1, pp. 2–13, 1977.

[51] D. Maugis, “Adhesion of spheres: the JKR-DMT transition using a Dugdale model,” *J. Colloid Interface Sci.*, vol. 150, no. 1, pp. 243–269, 1992.

[52] D. S. Dugdale, “Yielding of steel sheets containing slits,” *J. Mech. Phys. Solids*, vol. 8, no. 2, pp. 100–104, 1960.

[53] K. N. G. Fuller and D. Tabor, “The effect of surface roughness on the adhesion of elastic solids,” *Proc. R. Soc. London. Ser. A, Math. Phys. Sci.*, vol. 345, no. 1642, pp. 327–342, 1975.

[54] C. Gui, M. Elwenspoek, N. Tas, and J. G. E. Gardeniers, “The effect of surface roughness on direct wafer bonding,” *J. Appl. Phys.*, vol. 85, no. 10, pp. 7448–7454, 1999.

[55] S. N. Ramakrishna, L. Y. Clasohm, A. Rao, and N. D. Spencer, “Controlling adhesion force by means of nanoscale surface roughness,” *Langmuir*, vol. 27, no. 16, pp. 9972–9978, 2011.

[56] B. N. J. Persson and E. Tosatti, “The effect of surface roughness on the adhesion of elastic solids,” *J. Chem. Phys.*, vol. 115, no. 12, pp. 5597–5610, 2001.

[57] H. Rumpf, *Particle Technology*. London, UK: Chapman and Hall, 1990.

[58] Y. I. Rabinovich, J. J. Adler, A. Ata, R. K. Singh, and B. M. Moudgil, “Adhesion between Nanoscale Rough Surfaces,” *J. Colloid Interface Sci.*, vol. 232, no. 1, pp. 10–16, 2000.

[59] J. F. Archard, “Contact and Rubbing of Flat Surfaces,” *J. Appl. Phys.*, vol. 24, no. 8, p. 981, 1953.

[60] H.-J. Kim, S.-S. Yoo, and D.-E. Kim, “Nano-scale wear: A review,” *Int. J. Precis. Eng. Manuf.*, vol. 13, no. 9, pp. 1709–1718, Sep. 2012.

[61] E. Gnecco, R. Bennewitz, and E. Meyer, “Abrasive Wear on the Atomic Scale,” *Phys. Rev. Lett.*, vol. 88, no. 21, pp. 5–8, May 2002.

[62] Z. Sha, V. Sorkin, P. S. Branicio, Q. Pei, Y. Zhang, and D. J. Srolovitz, “Large-scale molecular dynamics simulations of wear in diamond-like carbon at the nanoscale Large-scale molecular dynamics simulations of wear in diamond-like carbon at the nanoscale,” *Appl. Phys. Lett.*, vol. 103, p. 073118, 2013.

[63] N.-S. Park, M.-W. Kim, S. C. Langford, and J. T. Dickinson, “Atomic layer wear of single-crystal calcite in aqueous solution using scanning force microscopy,” *J. Appl. Phys.*, vol. 80, no. 5, p. 2680, 1996.

[64] W. Maw, F. Stevens, S. C. Langford, and J. T. Dickinson, “Single asperity

tribochemical wear of silicon nitride studied by atomic force microscopy," *J. Appl. Phys.*, vol. 92, no. 9, pp. 5103–5109, 2002.

[65] P. E. Sheehan, L. J. Whitman, W. P. King, and B. A. Nelson, "Nanoscale deposition of solid inks via thermal dip pen nanolithography," *Appl. Phys. Lett.*, vol. 85, no. 9, p. 1589, 2004.

[66] P. E. Sheehan, "The wear kinetics of NaCl under dry nitrogen and at low humidities," *Chem. Phys. Lett.*, vol. 410, no. 1–3, pp. 151–155, Jul. 2005.

[67] J. Liu, J. K. Notbohm, R. W. Carpick, and K. T. Turner, "Method for characterizing nanoscale wear of atomic force microscope tips," *ACS Nano*, vol. 4, no. 7, pp. 3763–72, Jul. 2010.

[68] D. Grierson, E. Flater, and R. Carpick, "Accounting for the JKR-DMT transition in adhesion and friction measurements with atomic force microscopy," *J. Adhes. Sci. Technol.*, vol. 19, pp. 291–311, 2005.

[69] J. A. Greenwood, "Adhesion of elastic spheres," *Proc. R. Soc. A*, vol. 453, no. 1961, pp. 1277–1297, 1997.

[70] N. Yu and A. A. Polycarpou, "Adhesive contact based on the Lennard-Jones potential: a correction to the value of the equilibrium distance as used in the potential," *J. Colloid Interface Sci.*, vol. 278, no. 2, pp. 428–35, Oct. 2004.

[71] J. N. Israelachvili, *Intermolecular and Surface Forces*, 2nd edition. London, UK: Academic Press, 1991.

[72] A. Plößl and G. Kräuter, “Wafer direct bonding: Tailoring adhesion between brittle materials,” *Mater. Sci. Eng. R Reports*, vol. 25, pp. 1–88, 1999.

[73] I. Szlufarska, M. Chandross, and R. W. Carpick, “Recent advances in single-asperity nanotribology,” *J. Phys. D. Appl. Phys.*, vol. 41, no. 12, p. 123001, Jun. 2008.

[74] M. Wang, K. M. Liechti, J. M. White, and R. M. Winter, “Nanoindentation of polymeric thin films with an interfacial force microscope,” *J. Mech. Phys. Solids*, vol. 52, no. 10, pp. 2329–2354, Oct. 2004.

[75] M. Wang, K. M. Liechti, V. Srinivasan, J. M. White, P. J. Rossky, and M. T. Stone, “A Hybrid Continuum-Molecular Analysis of Interfacial Force Microscope Experiments on a Self-Assembled Monolayer,” *J. Appl. Mech.*, vol. 73, no. 5, pp. 769–777, 2006.

[76] P. C. Fletcher, J. R. Felts, Z. Dai, T. D. Jacobs, H. Zeng, W. Lee, P. E. Sheehan, J. A. Carlisle, R. W. Carpick, and W. P. King, “Wear-resistant diamond nanoprobe tips with integrated silicon heater for tip-based nanomanufacturing,” *ACS Nano*, vol. 4, no. 6, pp. 3338–3344, 2010.

[77] V. Vahdat, K. E. Ryan, P. L. Keating, Y. Jiang, S. P. Adiga, J. D. Schall, K. T. Turner, J. A. Harrison, and R. W. Carpick, “Atomic-scale wear of amorphous hydrogenated carbon during intermittent contact: a combined study using experiment, simulation, and theory.,” *ACS Nano*, vol. 8, no. 7, pp. 7027–40, Jul. 2014.

[78] A. V. Sumant, D. S. Grierson, J. E. Gerbi, J. A. Carlisle, O. Auciello, and R. W. Carpick, "Surface chemistry and bonding configuration of ultrananocrystalline diamond surfaces and their effects on nanotribological properties," *Phys. Rev. B*, vol. 76, no. 23, p. 235429, Dec. 2007.

[79] J. S. Villarrubia, "Algorithms for scanned probe microscope image simulation, surface reconstruction, and tip estimation," *J. Res. Natl. Inst. Stand. Technol.*, vol. 102, no. 4, pp. 425–454, Jul. 1997.

[80] J. L. Hutter and J. Bechhoefer, "Calibration of atomic-force microscope tips," *Rev. Sci. Instrum.*, vol. 64, no. 7, pp. 1868–1873, 1993.

[81] F. Restagno, J. Crassous, C. Cottin-Bizonne, and E. Charlaix, "Adhesion between weakly rough beads," *Phys. Rev. E*, vol. 65, no. 4, p. 042301, Apr. 2002.

[82] V. M. Muller, V. S. Yushchenko, and B. V. Derjaguin, "On the influence of molecular forces on the deformation of an elastic sphere and its sticking to a rigid plane," *J. Colloid Interface Sci.*, vol. 77, no. 1, pp. 91–101, 1980.

[83] K. L. Johnson and J. A. Greenwood, "An Adhesion Map for the Contact of Elastic Spheres," *J. Colloid Interface Sci.*, vol. 192, no. 2, pp. 326–333, 1997.

[84] J. R. Fried, *Polymer science and technology*, 2nd ed. Upper Saddle River, New Jersey: Prentice Hall, 2003.

[85] Y. Jiang and K. T. Turner, "Measurement of the strength and range of adhesion using atomic force microscopy," *Extrem. Mech. Lett.*, vol. 9, pp. 119–126, 2016.

[86] G. M. Swallowe and S. F. Lee, "A study of the mechanical properties of PMMA and PS at stain rates of 10^{-4} to 10^{3} over the temperature range 293-363 K," *J. Phys. IV Fr.*, vol. 110, pp. 33–38, 2003.

[87] M. F. Ashby and D. R. H. Jones, *Engineering Materials 2*, 4th ed. Elsevier, UK, 2013.

[88] J. A. Hammerschmidt, W. L. Gladfelter, and G. Haugstad, "Probing Polymer Viscoelastic Relaxations with Temperature-Controlled Friction Force Microscopy," *Macromolecules*, vol. 32, no. 10, pp. 3360–3367, May 1999.

[89] J. Sondhauß, M. Lantz, B. Gotsmann, and A. Schirmeisen, "β-Relaxation of PMMA: Tip Size and Stress Effects in Friction Force Microscopy.," *Langmuir*, vol. 31, no. 19, pp. 5398–405, May 2015.

[90] R. Bennewitz and J. T. T. Dickinson, "Fundamental Studies of Nanometer-Scale Wear Mechanisms," *MRS Bull.*, vol. 33, pp. 1174–1180, 2008.

[91] P. R. Barry, P. Y. Chiu, S. S. Perry, W. G. Sawyer, S. B. Sinnott, and S. R. Phillpot, "Effect of Temperature on the Friction and Wear of PTFE by Atomic-Level Simulation," *Tribol. Lett.*, vol. 58, no. 3, p. 50, May 2015.

[92] M. Rubinstein and R. H. Colby, *Polymer Physics*. Oxford, 2003.

[93] N. G. McCrum, B. E. Read, and G. Williams, *Anelastic and Dielectric Effects in Polymeric Solids*. London: Wiley, 1967.

[94] M. Williams, R. Landel, and J. Ferry, "The temperature dependence of relaxation

mechanisms in amorphous polymers and other glass-forming liquids," *J. Am. Chem. Soc.*, vol. 77, no. 14, pp. 3701–3707, 1955.

[95] K. Paeng, R. Richert, and M. D. Ediger, "Molecular mobility in supported thin films of polystyrene, poly(methyl methacrylate), and poly(2-vinyl pyridine) probed by dye reorientation," *Soft Matter*, vol. 8, no. 3, pp. 819–826, 2012.

[96] W. Oliver and G. Pharr, "An improved technique for determining hardness and elastic modulus using load and displacement sensing indentation experiments," *J. Mater. Res.*, vol. 7, no. 6, pp. 1564–1583, 1992.

[97] K. Kendall, "The adhesion and surface energy of elastic solids," *J. Phys. D. Appl. Phys.*, vol. 4, pp. 1186–1195, 1971.

[98] N. S. Tambe and B. Bhushan, "Scale dependence of micro/nano-friction and adhesion of MEMS/NEMS materials, coatings and lubricants," *Nanotechnology*, vol. 15, no. 11, pp. 1561–1570, Nov. 2004.

[99] N. S. Tambe and B. Bhushan, "Micro/nanotribological characterization of PDMS and PMMA used for BioMEMS/NEMS applications," *Ultramicroscopy*, vol. 105, pp. 238–247, 2005.

[100] A.-T. Akono and F.-J. Ulm, "Scratch test model for the determination of fracture toughness," *Eng. Fract. Mech.*, vol. 78, no. 2, pp. 334–342, Jan. 2011.

[101] M. J. Adams, A. Allan, B. J. Briscoe, P. J. Doyle, D. M. Gorman, and S. A. Johnson, "An experimental study of the nano-scratch behaviour of poly(methyl

methacrylate),” *Wear*, vol. 251, no. 1–12, pp. 1579–1583, Oct. 2001.

[102] Y.-R. Huang, Y. Jiang, J. L. Hor, R. Gupta, L. Zhang, K. J. Stebe, G. Feng, K. T. Turner, and D. Lee, “Polymer nanocomposite films with extremely high nanoparticle loadings via capillary rise infiltration (CaRI),” *Nanoscale*, vol. 7, pp. 798–805, 2015.

[103] N. Tayebi, T. F. Conry, and A. A. Polycarpou, “Determination of hardness from nanoscratch experiments: Corrections for interfacial shear stress and elastic recovery,” *J. Mater. Res.*, vol. 18, no. 9, pp. 2150–2162, Jan. 2003.

[104] V. Hegadekatte, N. Huber, and O. Kraft, “Finite element based simulation of dry sliding wear,” *Model. Simul. Mater. Sci. Eng.*, vol. 13, no. 1, pp. 57–75, Jan. 2005.

[105] T. Zhang, P. E. McHugh, and S. B. Leen, “Computational study on the effect of contact geometry on fretting behaviour,” *Wear*, vol. 271, no. 9–10, pp. 1462–1480, 2011.

[106] I. R. McColl, J. Ding, and S. B. Leen, “Finite element simulation and experimental validation of fretting wear,” *Wear*, vol. 256, no. 11–12, pp. 1114–1127, 2004.

[107] N. H. Kim, D. Won, D. Burris, B. Holtkamp, G. R. Gessel, P. Swanson, and W. G. Sawyer, “Finite element analysis and experiments of metal/metal wear in oscillatory contacts,” *Wear*, vol. 258, no. 11–12, pp. 1787–1793, 2005.

[108] N. L. McCook, D. L. Burris, N. H. Kim, and W. G. Sawyer, “Cumulative damage modeling of solid lubricant coatings that experience wear and interfacial fatigue,”

Wear, vol. 262, no. 11–12, pp. 1490–1495, 2007.

[109] M. F. Ashby and S. C. Lim, "Wear-mechanism maps," *Scr. Metall. Mater.*, vol. 24, no. 5, pp. 805–810, 1990.

[110] A. Rezaei, W. Van Paepegem, P. De Baets, W. Ost, and J. Degrieck, "Adaptive finite element simulation of wear evolution in radial sliding bearings," *Wear*, vol. 296, no. 1–2, pp. 660–671, 2012.

[111] K. L. Johnson, *Contact mechanics*. Cambridge, UK: Cambridge University Press, 1985.